NOAA Technical Memorandum NMFS-AFSC-403

Deriving Apparent Optical Properties from Light Measurements Obtained Using Bottom-trawl-mounted Archival Tags

S. K. Rohan, S. Kotwicki, L. L. Britt, E. A. Laman, and K. Aydin

June 2020

U.S. DEPARTMENT OF COMMERCE

National Oceanic and Atmospheric Administration
National Marine Fisheries Service
Alaska Fisheries Science Center

The National Marine Fisheries Service's Alaska Fisheries Science Center uses the NOAA Technical Memorandum series to issue informal scientific and technical publications when complete formal review and editorial processing are not appropriate or feasible. Documents within this series reflect sound professional work and may be referenced in the formal scientific and technical literature.

The NMFS-AFSC Technical Memorandum series of the Alaska Fisheries Science Center continues the NMFS-F/NWC series established in 1970 by the Northwest Fisheries Center. The NMFS-NWFSC series is currently used by the Northwest Fisheries Science Center.

This document should be cited as follows:

S. K. Rohan, S. Kotwicki, L. L. Britt, E. A. Laman, and K. Aydin. 2020. Deriving apparent optical properties from light measurements obtained using bottom-trawl-mounted archival tags. U.S. Dep. Commer., NOAA Tech. Memo. NMFS-AFSC-403, 91 p.

This document is available online at:

Document available: https://repository.library.noaa.gov/welcome

This document is available to the public through:
National Technical Information Service
U.S. Department of Commerce
5285 Port Royal Road
Springfield, VA 22161

www.ntis.gov

NOAA FISHERIES

Deriving Apparent Optical Properties from Light Measurements Obtained Using Bottom-trawl-mounted Archival Tags

S. K. Rohan, S. Kotwicki, L. L. Britt, E. A. Laman, and K. Aydin

Alaska Fisheries Science Center
Resource Assessment and Conservation Engineering Division
7600 Sand Point Way
Seattle, WA 98115

U.S. DEPARTMENT OF COMMERCE

National Oceanic and Atmospheric Administration
National Marine Fisheries Service
Alaska Fisheries Science Center

NOAA Techncial Memorandum NOAA-TM-AFSC-403

June 2020

ABSTRACT

Since 2004, the National Marine Fisheries Service's Alaska Fisheries Science Center has collected light data during bottom-trawl surveys using trawl-mounted archival tags equipped with a photoelectric cell. The archival tags continuously record light measurements during bottom-trawl survey hauls and provide vertical profiles of downwelling light during each deployment and retrieval (downcast and upcast) of the bottom-trawl gear. Given the temporal frequency and spatial resolution of bottom-trawl survey sampling, these measurements provide an unprecedented opportunity to monitor subsurface water clarity in Alaska's marine ecosystems and to characterize the visual environment inhabited by deep-dwelling marine fauna. This technical memorandum describes an algorithm which applies quality control checks to archival tag light measurements obtained during bottom-trawl surveys, then derives apparent optical properties (optical depth and vertical attenuation coefficient of downwelling irradiance) from the bottom-trawl survey light data. To determine whether the data collection method and algorithm yields reproducible and precise apparent optical properties, we applied the algorithm to light data obtained during annual summer bottom-trawl surveys of the eastern Bering Sea continental shelf from 2004 to 2018. Out of 10,837 casts from the eastern Bering Sea continental shelf during 2004–2018, 7,887 (72.8%) passed quality control checks. Apparent optical properties derived from cast data were reproducible and precise. A description of an experimental data product containing apparent optical properties derived for the eastern Bering Sea is described herein.

CONTENTS

INTRODUCTION

Changes in the visual environment (light and water clarity) of coastal marine ecosystems can have implications for the assessment and management of fish stocks. Because fishes rely on vision for feeding, orientation, threat detection, schooling, and reproduction (Lythgoe 1979, Douglas and Hawryshyn 1990, Warrant and Locket 2004), the visual environment affects the catchability of survey and commercial gears (Glass and Wardle 1989, Buijse et al. 1992, Ryer and Olla 2000, Ryer and Barnett 2006, Ryer 2008, Kotwicki et al. 2009, Stapanian et al. 2009. Ryer et al. 2010) and productivity of fish stocks (Eiane et al. 1999, Fiksen et al. 2002, Utne-Palm 2002, Aksnes 2007). Changes in the visual environment can alter the structure and function of ecosystems (Beauchamp et al. 1999, Sørnes and Aksnes 2004, Varpe et al. 2015, Klevjer et al. 2016, Langbehn and Varpe 2017). However, the subsurface visual environment is infrequently monitored in coastal marine ecosystems due to the logistical challenge of obtaining samples at fine resolution across a large spatial extent, and the need to use expensive sampling equipment.

The visual environment of aquatic ecosystems is often characterized using apparent optical properties (e.g., Lovvorn et al. 2001, Aksnes et al. 2004, Staby and Aksnes 2011) that characterize the transmission of light through water in manner that is dependent on inherent optical properties of water and the angular structure of the radiance field (Kirk 2011). If they characterize regular features of the water column in a stable (i.e., reproducible) manner, apparent optical properties provide a means to compare water clarity across space and time (Mobley 1994). To meet this criteria, equipment used to obtain light measurements must be able to accurately characterize relative changes in light intensity across the range of intensities, color spectra, and angular structure the light field that occurs in the sampled domain.

In optically complex coastal marine ecosystems, in situ sampling is necessary to obtain apparent optical properties that provide an accurate and precise characterization of the subsurface visual environment. Satellite-based remote sensing can be used to derive near-surface apparent optical properties under clear-sky conditions, but near-surface apparent optical properties do not necessarily provide an accurate representation of subsurface conditions (e.g., Capuzzo et al. 2013, Naik et al. 2013). In coastal marine ecosystems, physical and biological constituents of the water column vary with depth, causing depth-dependent variation in optical properties (Naik et al. 2013). Within a water column, optical properties can vary due to surface chlorophyll (Wernand et al. 2013, Sigler et al. 2014), deep chlorophyll maxima (Naik et al. 2010), sediment resuspension driven by currents, winds, and tides (McManus and Smyth 1970, Kawana 1975), and terrestrial-origin chromophoric dissolved organic matter and suspended particulate matter (Kirk 2011). In situ, apparent optical properties are primarily obtained from vessel-based oceanographic surveys and fixed moorings. However, such sampling is often conducted sporadically over time, and is spatially and temporally decoupled from biological sampling of deep-dwelling fishes and invertebrates.

Obtaining in situ apparent optical properties during fisheries-independent stock assessment surveys would improve monitoring of the visual environment in coastal marine ecosystems and provide useful information about the visual environment in habitats used by deep-dwelling fauna. Stock assessment surveys are designed to provide sustained, systematic monitoring of marine ecosystems. Stock assessment surveys often use temporally stationary sampling schemes which allocate effort across gradients in ecological communities and habitat.

Miniaturization and ruggedization of oceanographic sampling equipment has increasingly enabled the collection of environmental data during bottom-trawl stock assessment surveys (e.g.,

Kotwicki et al. 2009, Cokelet 2016), which has improved our understanding of how environmental factors influence the distribution, productivity, and catchability of marine fish stocks (Baker and Hollowed 2014, Laman et al. 2014, 2018, Holsman and Aydin 2015, Kotwicki et al. 2015, Vestfals et al. 2016, Yeung and Yang 2018, Rooper et al. 2019). During bottom-trawl surveys, most environmental data are collected using equipment attached to trawl gear (Bradburn and Keller 2015, Cokelet 2016, Conner et al. 2017, Stevenson and Lauth 2019). Apparent optical properties have not been monitored during bottom-trawl surveys, in part because conventional radiometers and quantum sensors are expensive and susceptible to damage during trawl operations.

Light measurements collected during bottom-trawl surveys conducted by the National Marine Fisheries Service provide an opportunity to evaluate whether it is feasible to derive apparent optical properties from data collected during stock assessment surveys. Passive measurements of water column light have been collected during bottom-trawl surveys of Federally-managed waters of Alaska and West Coast of the continental United States (Kotwicki et al. 2009, Bradburn and Keller 2015, Hoff 2016, Conner et al. 2017, von Szalay et al. 2017). In Alaska, measurements have been collected annually from the eastern Bering Sea since 2004, biennially from the Gulf of Alaska since 2005, biennially from the Aleutian Islands since 2006, and from the Chukchi Sea in 2012. Light measurements are obtained using archival tags equipped with a photoelectric cell, intended to provide measurements which can be used as a basis for geolocation of tagged animals. However, archival tag light measurements from bottom-trawl surveys have been used as a basis to derive density-dependent trawl efficiency correction factors for the bottom-trawl survey index of abundance of walleye pollock in the eastern Bering Sea (Kotwicki et al. 2014) and to estimate light-dependent vertical distribution of walleye

Pollock in order to combine bottom trawl and acoustic survey data for stock assessment (Kotwicki et al. 2018). In the U.S. West Coast region, variation in archival tag light measurements have been linked to variation in catch rates of arrowtooth flounder, Pacific hake, longnose skate, and greenstripe rockfish (Bradburn and Keller 2015).

Previous work suggests it is feasible to derive apparent optical properties from light data collected using trawl-mounted archival tags. Light measurements obtained using undulating samplers towed behind vessels traveling at 4-6 m s^{-1} have been used to derive apparent optical properties that are consistent with values derived using sampling equipment deployed from a stationary vessel (Aiken and Bellan 1990, Savidge et al. 1992). Apparent optical properties have also been derived from light measurements obtained from archival tags attached to pinnipeds (Jaud et al. 2012, O'Toole et al. 2014).

To provide a useful characterization of visual habitat, apparent optical properties need to capture variation in light transmission in a manner that is sufficiently accurate and precise to be relevant to vision. Although fishes occupy habitat spanning at least 10 orders of magnitude of variation in ambient light levels, life stages of a species are often concentrated in habitat spanning 2-4 orders of magnitude of variation in ambient light (Roe 1983, Kaartvedt et al. 1996, Røstad et al. 2016). The ability of fishes to feed (Henderson and Northcote 1985, Aksnes and Utne 1997, Ryer and Olla 1999, Vogel and Beauchamp 1999, Mazur and Beauchamp 2003, Hurst et al. 2007) and school (Glass et al. 1986, Ryer and Olla 1998) can decrease from a maximum to zero given a 3-4 order of magnitude decrease in light. And similarly, visual reactions to trawl gear can cease given a 3-4 order of magnitude decrease in light (Glass and Wardle 1989, Olla et al. 1997, 2000, Ryer and Olla 2000). As such, apparent optical properties

likely need to characterize the ambient light environment to within an order of magnitude to provide an ecologically meaningful characterization of visual habitat.

To obtain apparent optical properties from bottom-trawl survey light data, we developed an algorithm that performs quality control checks then derives apparent optical properties from light measurements obtained during NFMS bottom-trawl surveys using trawl-mounted archival tags. The algorithm derives optical depth, a logarithmic ratio that relates light just below the sea surface to light at depth, and the vertical attenuation coefficient of downwelling irradiance, the rate at which light is decreasing at depth. We evaluated the performance of the algorithm by applying it to light data collected during annual summer bottom-trawl surveys of the eastern Bering Sea continental shelf from 2004 to 2018. We tested for biases in algorithm subroutines. Then, we used the derived apparent optical properties to ask whether the approach to data collection and processing yields apparent optical properties that are reproducible and precise, although we did not evaluate absolute accuracy. Finally, we describe an experimental apparent optical properties data product for the eastern Bering Sea continental shelf.

MATERIALS AND METHODS

Light Data Collection

Water column and surface light measurements have been collected during National Marine Fisheries Service bottom-trawl surveys in Alaska since 2004. Light data have been collected from the eastern Bering Sea continental shelf since 2004, northern Bering Sea continental shelf since 2010, eastern Bering Sea continental slope since 2008, Aleutian Islands

since 2006, Gulf of Alaska since 2007, and Chukchi Sea since 2012. Survey sampling schemes and trawl gears vary between regions but, for all surveys, sampling is conducted during daylight hours, with hauls starting ≥ 30 minutes after sunrise and ending ≤ 30 minutes before sunset (Stauffer 2004). During hauls, vessels tow at a target speed of 3 knots (speed over the ground).

During each haul, light measurements are collected using trawl-mounted Wildlife Computers TDR-Mk9 archival tags that have a built-in Hamamatsu S2387 photodiode[1]. The unfiltered photodiodes have a sensitivity range from 340 to 1,100 nm with a peak sensitivity at 960 nm, but are equipped with a bandpass filter which, for tags manufactured prior to 2012, has 50% of transmissivity from 460 to 548 nm[2]. All tags used for this study were manufactured prior to 2012. Based on high spectral resolution monochromator measurements, Vacquié-Garcia et al. (2017) suggested the spectral response of TDR10-X archival tags, equipped with the same bandpass-filtered photodiodes as the TDR-Mk9 have a peak spectral sensitivity at 465 nm with a half-band width of 420–470 nm, although it is unclear how this sensitivity is related to absolute sensitivity because the absolute spectral output of the monochromator at each waveband was unknown. However, tags have some sensitivity across the visible spectrum with highest sensitivity in the blue and a relatively flat response at long (green–red) wavelengths (Vacquié-Garcia et al. 2017, Lyle Britt, unpublished research). Archival tags record light measurements in manufacturer-specific relative integer units using an on-board log-transformation. The integer range is approximately 25–225 which, per manufacturer specifications, corresponds with an absolute radiometric irradiance sensitivity of 10×10^{-12} W cm^{-2} to 5×10^{-2} W cm^{-2} in the blue spectrum. Between TDR-Mk9 tags, Kotwicki et al. (2009) found the relative unit measurements

[1] Trade names are used for identification purposes only. Reference to trade names does not imply endorsement by the National Marine Fisheries Service, NOAA.
[2] Heather Baer, Wildlife Computers, personal communication, 16 April 2020.

from archival tags varied around a mean by approximately two relative units. For a single TDR10-X tag, Vacquié-Garcia et al. (2017) found that under constant light conditions, measurements fluctuate by two relative units.

The photoelectric cell has a wide acceptance angle and is not equipped with a cosine collector. Evaluating the response of photoelectric cells to light at varying angles, Vacquié-Garcia et al. (2017) found that TDR10-X tags had a peak response to 465 nm light provided from an LED source at a 0° zenith angle, with the response decreasing towards zero as the angle of incident light decreased to zenith angles greater than 50°. Thus, we expect archival tag light measurements provide an approximation of downwelling irradiance but have a response bias that depends on the angular structure of radiance field relative to the orientation of the photoelectric cell of the archival tag. The angular structure of the radiance field varies with solar zenith angle (Baker and Smith 1979, Kirk 2011).

Trawl-mounted archival tags are affixed to triangular, white polyurethane baseplates with shackles at the anterior corners (Fig. 1). During each haul, the archival tag assembly is attached to the exterior of the top panel of the bottom-trawl gear, approximately 1 m behind the headrope of the trawl gear, with the photoelectric cell of the archival tag facing upward. Trawl-mounted archival tags record light measurements every 1 second, while the archival tag is wet. An oblique profile of water column light measurements is obtained during each net deployment (downcast) and retrieval (upcast).

Since 2006, light measurements have been collected aboard survey vessels, during hauls, using deck-mounted archival tags. Deck-mounted archival tags are positioned in unobstructed locations atop the bridges of survey vessels, with the photoelectric cell facing up. Deck-mounted archival tags record light measurements every 10 s for the duration of surveys.

Archival tags were replaced and added opportunistically and according to need, over the duration of the study. Tags were haphazardly assigned to vessels (and trawl or deck), and 18 different tags were used during the study. Individual tags were deployed in the eastern Bering Sea a median of three times (range: 1–7). Individual tags were deployed over a median duration of three survey years (range: 1–12 years). Light measurements from archival tags were not regularly calibrated, so it is unclear if the intensity-response of individual tags drifted over time.

Figure 1. -- Archival tag affixed to polyurethane baseplate.

Although archival tags record depth measurements, they were not used to determine the depth from which light measurements were obtained because archival tags are not depth-calibrated prior to surveys. Instead, we used depth measurements collected with a Seabird SBE-39 temperature-depth recorder that is calibrated annually. The SBE-39 is attached to the trawl headrope, adjacent to the archival tag assembly. Internal clocks of the archival tag and SBE-39 are time-synchronized prior to the surveys, and data are corrected for temporal misalignment and

drift after the surveys. The maximum temporal drift between the SBE-39 and TDR-Mk9 is typically few seconds.

Data Processing Algorithm

We developed an algorithm to derive apparent optical properties of the water column using bottom-trawl survey light data. The light data processing algorithm implements a series of subroutines which separate signal from noise in raw light measurements, applies data quality checks, and derives apparent optical properties from bottom-trawl survey light data (Fig. 2). The algorithm does not require intensity-response of the archival tag photoelectric cells to be identical among tags, but does assume that, for individual tags, measured light intensity (in relative units) scales proportionally with true light intensity. Functions to implement algorithm subroutines and accompanying documentation of functions are available in the R package *trawllight* (Rohan 2020).

The apparent optical properties derived by the algorithm are optical depth, OD(Z), and the instantaneous vertical attenuation coefficient of downwelling irradiance, $K_d(Z)$. Apparent optical property derivation is based on the Beer's law equation,

$$E_d(Z) = E_d(R)e^{-K_d Z}, \qquad \text{Eqn. (1)}$$

where Z is depth (m), $E_d(Z)$ is vertical downwelling irradiance at depth Z ($\mu \cdot M \cdot photons \cdot m^{-2} \cdot s^{-1}$) $E_d(R)$ is downwelling irradiance at a reference depth, K_d is the vertical attenuation coefficient of downwelling irradiance between the reference depth and depth Z (m^{-1}).

Optical depth, OD(Z) is a dimensionless log-ratio which characterizes the light level at depth Z relative to light at a reference depth just below the water surface. OD(Z) can be used to compare light transmission through the water column over space and time. OD(Z) defined as

$$OD(Z) = \ln E_d(R) - \ln E_d(Z). \qquad \text{Eqn. (2)}$$

The vertical attenuation coefficient of downwelling irradiance, $K_d(Z)$, characterizes the rate at which light is decreasing at depth Z. $K_d(Z)$ provides a measure of relative light transmission at a depth and can be used to qualitatively describe vertical structure of light attenuating layers within the water column. $K_d(Z)$ is defined as

$$K_d(Z) = -\frac{d\ln(E_d(Z))}{dZ}. \qquad \text{Eqn. (3)}$$

Algorithm subroutines used for light data processing are described below.

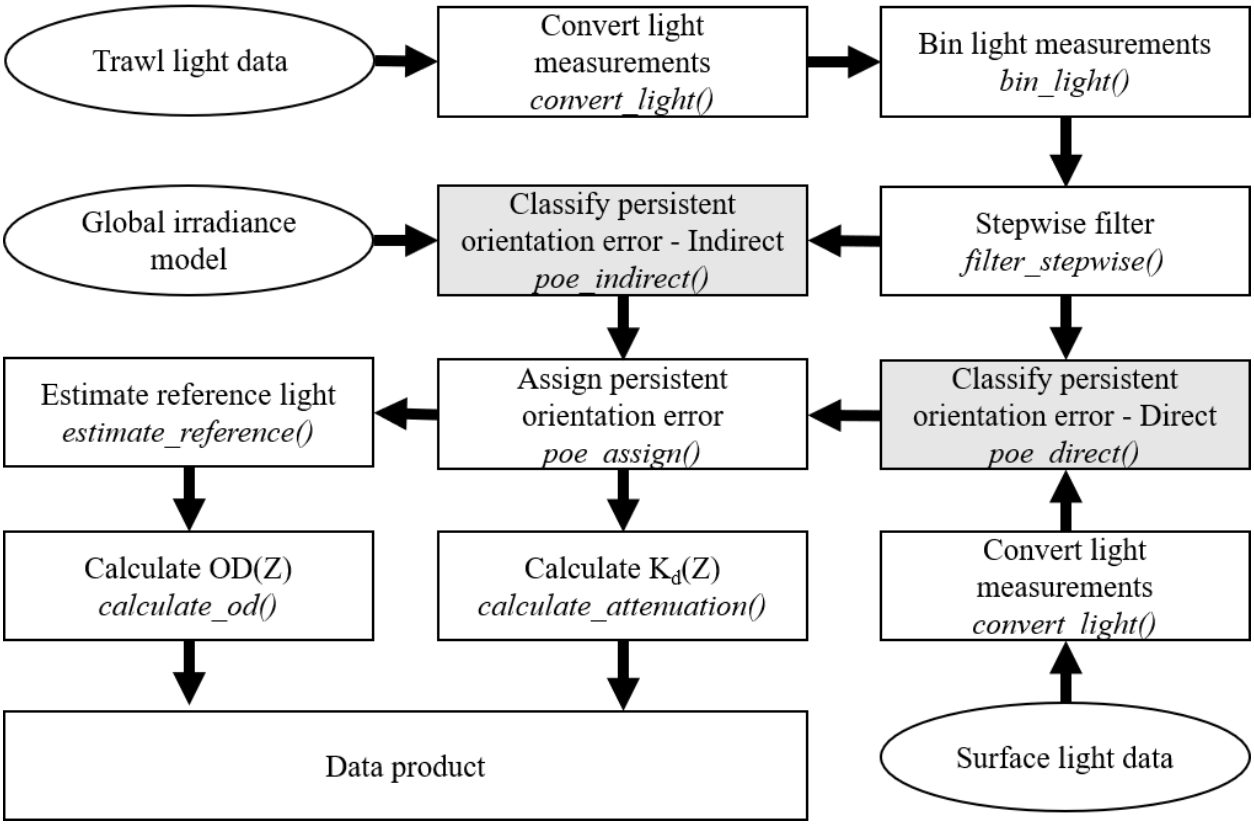

Figure 2. -- Flow chart of algorithm subroutines used to apply quality control checks to data and derive apparent optical properties data product (Alaska Fisheries Science Center 2020). Italicized names indicate the names of functions implemented in the R package *trawllight* (Rohan 2020) which are used to process light data.

Convert light measurements

Because the archival tags record downwelling light measurements in relative integer units, that are not physically or biologically meaningful quantities, the algorithm converts archival tag measurements to downwelling irradiance, $E_d(Z)$ $\mu M \cdot photons \cdot m^{-2} \cdot s^{-1}$. The conversion is based on calibration experiments, conducted under green (555 nm) and white (broad spectrum) light, which found an approximately log-linear relationship between TDR-Mk9 light measurements and irradiance measured using an International Light IL1700 radiometer equipped with photosynthetically active radiation sensor (Kotwicki et al. 2009).

Bin light measurements

Subsurface light measurements are affected by rapid fluctuations in atmospheric light and periodic refraction due to waves. To minimize the effects of rapid fluctuations in light, the geometric mean of light measurements from individual casts are calculated for each 2-m depth bin in the water column. A geometric mean was used instead of an arithmetic mean because large spikes in individual light measurements sporadically occurred near the sea surface, which may have occurred due to periodic focusing of light by waves.

Stepwise filter

After calculating depth-binned measures of central tendency from raw light measurements, signal processing methods (e.g., Kalman filter) are typically applied to binned light measurements to further distinguish signal from noise in light data (Smith and Baker 1984, Kirk 2011). However, some casts had periodic variation in light measurements near the surface which caused conventional filter methods to retain autocorrelated process noise in $E_d(Z)$. Thus,

based on the assumption that $E_d(Z)$ should decrease with depth, the algorithm uses a stepwise point removal procedure to iteratively omit binned $E_d(Z)$ which are darker than $E_d(Z)$ deeper in the water column. For example, if $E_d(1) < E_d(3)$, the algorithm omits $E_d(1)$. The stepwise algorithm omits points until $E_d(Z_1) \geq E_d(Z_2) \geq \cdots \geq E_d(Z_{max})$, where $E_d(Z_i)$ are downwelling irradiance values ordered by depth in the water column.

Classify persistent orientation error

To obtain measurements of downwelling irradiance, the archival tag should be oriented perpendicular to the main axis of the angular distribution of downwelling radiance. Inconsistent orientation of archival tags would cause measurement errors which would affect the precision and reproducibility of apparent optical properties. However, information about the orientation of archival tags was not collected during hauls.

Although the stepwise filtering subroutine handles measurement errors caused by rapid changes in archival tag orientation, it does not handle persistent orientation errors (e.g., due to the archival tag assembly being mounted upside down). Thus, a separate subroutine was necessary to detect cases of persistent orientation error to reduce the potential for orientation errors to affect the derivation of apparent optical properties.

The algorithm uses two subroutines to detect probable cases of persistent orientation error based on light measurements: a direct method and an indirect method. Direct method and indirect method subroutines are predicated on the assumption that changes in archival tag orientation away from the main axis of downwelling irradiance would result in lower-than-expected light measurements.

The direct method for detecting persistent orientation errors is intended for casts where surface light measurements are obtained simultaneously. For the direct method, the log-ratio between surface and subsurface light, τ, is calculated for each cast, as

$$\tau = \ln\left(\frac{E_d(Z)}{E_d(S)}\right), \qquad \text{Eqn. (4)}$$

where $E_d(S)$ is the average surface light recorded by a deck-mounted archival tag within 30 seconds of the cast start or end time, and $E_d(Z)$ is light for the depth bin centered at Z m below the sea surface. Then, the first derivative of the kernel density distribution of τ, among all casts, is calculated. The threshold for persistent orientation error is assigned as the largest value of τ that is less than the mode of the kernel density distribution, where the first derivative of the kernel density distribution is equal to zero.

The indirect method is intended for casts where surface light measurements are not available. For the indirect method, a generalized additive model is fit between modeled log-transformed clear-sky photosynthetically active radiation, I_{PAR} ($W \cdot m^{-2}$), from an atmospheric irradiance model (Frouin et al. 1989, Nelson 2018) and $\ln(E_d(Z))$, at a specific depth, across all casts. The model is

$$\ln\big(E_d(Z)\big) \sim \beta_0 + s(\ln(I_{PAR})) + \varepsilon\,, \qquad \text{Eqn. (5)}$$

where β_0 is the intercept, $s(\cdot)$ is a basis spline, and $\varepsilon \sim N(0,\sigma^2)$. The generalized additive model is used because the relationship between $E_d(Z)$ and I_{PAR} is non-linear, as the relationship between $E_d(Z)$ and I_{PAR} may vary with solar zenith angle. Solar zenith angle is not included as a covariate in the model due to collinearity with I_{PAR}. The indirect method subroutine estimates the kernel density distribution of generalized additive model residuals using a Gaussian kernel function. Then, the first derivative of the kernel density function distribution of the generalized additive model residuals is used as a basis to identify a persistent orientation error threshold. The indirect

method subroutine assigns persistent orientation error thresholds to be the largest residual value, less than the mode of the kernel density distribution, where the first derivative of the kernel density distribution is equal to zero. The indirect method subroutine fits the generalized additive model using cubic regression splines, implemented in the R package 'mgcv' (Wood 2011).

A key consideration for estimating kernel density distributions is the choice of bandwidth used by the kernel density function. An appropriate bandwidth minimizes bias while not over-or-under-smoothing kernel density distributions (Wand and Jones 1994). Bandwidths can be selected based on prior information, graphical analysis, or an automatic selection method. Because there is no information available to select a bandwidth a priori, the direct method and indirect method subroutines use an automatic bandwidth selection method, indirect cross-validation (Savchuk et al. 2010), for bandwidth selection. For samples sizes ≥ 100, indirect cross-validation has low bias and provides more stable bandwidth estimates than commonly-used bandwidth selectors (Heidenreich et al. 2013).

Assign persistent orientation error

Classifications of persistent orientation error can differ between depth bins and between the direct method and indirect method. To resolve conflicts between classifications, the algorithm assigns a final classification to each cast based on hierarchical rules. Direct method classifications are accepted ahead of indirect method classifications, and classifications from shallower depth bins are accepted ahead of classifications from deeper depth bins. The rationale for these hierarchical rules is that in situ measurements are more dependable than model estimates of I_{PAR}, which are affected by atmospheric conditions, and that high attenuation near the surface can cause downwelling irradiance to decrease rapidly with depth.

Calculate vertical attenuation coefficient of downwelling irradiance

Using conventional sampling equipment, $K_d(Z)$ is typically derived by estimating the slope of a least-squares fit between Z and $\ln(E_d(Z))$ over fixed depth intervals, or by using a moving window average to smooth profiles of binned $E_d(Z)$, then estimating $K_d(Z)$ over fixed depth intervals as

$$K_d(Z_1 \rightarrow Z_2) = \frac{\ln \widehat{E_d(Z_1)} - \ln \widehat{E_d(Z_2)}}{(Z_2 - Z_1)}, \qquad \text{Eqn. (6)}$$

where $E_d(Z_1)$ and $E_d(Z_2)$ are light measurements from consecutive depth bins. For archival tag light data, fixed depth-interval methods cause biases in $K_d(Z)$ due to the coarse precision of archival tag integer units. As light decreases, the rate of change in integer measurements recorded by archival tags decreases, slowing the rate of change in $E_d(Z)$. Consequently, using a small fixed-depth interval when water clarity is low or the water column is deep (>100 m), results in profiles with sequential zeros in $K_d(Z)$ which are interspersed by spikes when the integer unit of the archival tag changes. When attenuation is low or the water column is deep, using a large fixed-interval masks changes in $K_d(Z)$ over small depth intervals.

In lieu of a fixed-depth interval method, the algorithm fits first-order loess models with normally-distributed error between Z and $\ln(E_d(Z))$, for individual casts, using an automatic span selection method. Then, Equation 6 is used to estimate $K_d(Z)$ from the fitted loess model. First order loess models provide a better fit at the upper and lower depth limits of a profile than alternative polynomial bases (Keele 2008). For each cast, constrained optimization is used to automatically select a span that minimizes an approximation of bias-corrected Akaike's Information Criterion (AIC_c),

$$AIC_C = \ln(\hat{\sigma}^2) + 1 + \frac{2\{tr(H) + 1\}}{n - tr(H) - 2}\ , \qquad \text{Eqn. (7)}$$

where $\hat{\sigma}^2$ is the fitted standard deviation of the model, n is the number of $E_d(Z)$ in a cast, and tr(H) is the trace of the hat matrix of the model (Hurvich et al. 1998).

Estimate reference light

To calculate optical depth, it is necessary to have light measurements for the reference depth, $E_d(R)$. However, $E_d(R)$ are sometimes missing or omitted by the stepwise algorithm. In such cases, the algorithm estimates $E_d(R)$.

The subroutine to estimate reference light uses one of two approaches depending on the depth of the reference depth relative to the depths of available light data. In cases where the reference depth is located between two depth bins with light measurements, the reference light measurement is interpolated as

$$\widehat{E_d(R)} = E_d(a) * \exp\left(\frac{\ln E_d(b) - \ln E_d(a)}{b - a} * (R - a)\right), \quad \text{Eqn. (8)}$$

where R is the reference depth, a is the midpoint of the closest depth bin above the reference depth with a light measurement, and b is the midpoint of the closest depth bin below the reference depth with a light measurement. In cases where the reference depth is above the shallowest available light measurement, the reference depth is estimated as

$$\widehat{E_d(R)} = E_d(A) * \exp\left(\frac{\frac{\ln(E_d(A)) - \ln(E_d(B))}{B - A} + \frac{\ln(E_d(A)) - \ln(E_d(C))}{C - A}}{2} * (A - R)\right), \text{Eqn. (9)}$$

where A, B, and C are, the shallowest, second shallowest, and third shallowest depth bins with light data that are deeper than the depth of the reference bin, respectively.

Calculate optical depth

For every depth bin deeper than the reference depth, optical depth is calculated using Eqn. 2.

Application to the Eastern Bering Sea

We tested the algorithm using light measurements collected during annual summer bottom-trawl surveys of the eastern Bering Sea during 2004–2018. The eastern Bering Sea shelf is a broad (~500 km wide) continental shelf system that slopes gently from the Alaska mainland to the continental shelf break at ~180 m bottom depth (Fig. 2). The eastern Bering Sea bottom-trawl survey sampled the same 376 stations each year, during late May-early August. Each year, two chartered commercial fishing vessels were used to conduct the survey following standardized survey sampling protocols. Surveys generally progressed from interior Bristol Bay in the southeast to the continental shelf break in the northwest. Water column light measurements were obtained every year, while surface light measurements were collected from 2006–2018. Multiple archival tags were used during the study, and archival tag intercalibration was not performed.

Bottom-trawl survey hauls had a target sampling duration of 30 minutes per haul, towing at a target vessel speed of 3 knots. Given the vessel speed and sampling duration, oblique profiles of light measurements were obtained ~1.5 nautical miles (nmi) apart during each haul. During casts, the trawl net and archival tag were > 50 m behind the survey vessel, and vessels did not produce noticeably bubbly propeller wake during casts. Survey protocols mandated that

hauls were conducted between 30 minutes after sunrise and 30 minutes before sunset (Stauffer 2004).

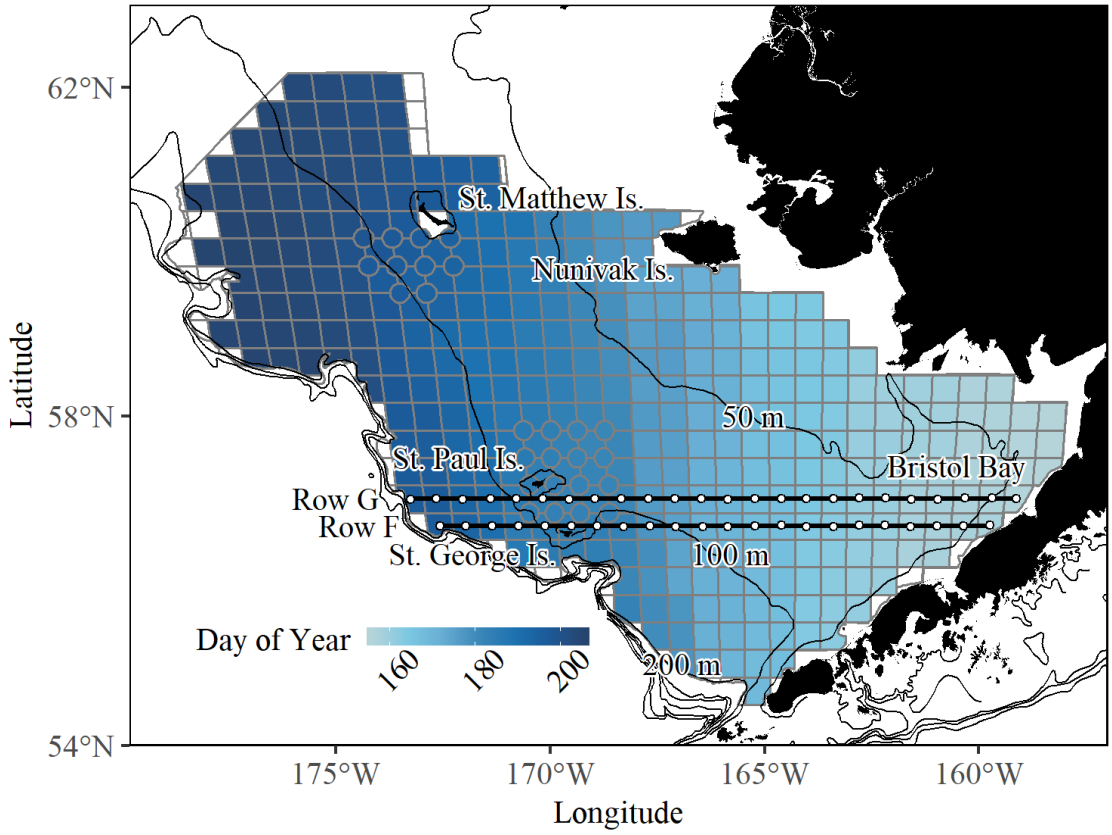

Figure 3. -- National Marine Fisheries Service bottom-trawl survey area of the eastern Bering Sea continental shelf. Grid cells denote the 376 survey stations. Fill color indicates the average day of year of sampling for stations during 2004–2018. Sampling locations for stations F and G during 2005–2006 are indicated by dots and the line.

Sampling was conducted under variable conditions of weather and sea state. Hauls were not conducted when the sea state was too rough to safely conduct survey operations. At the beginning of most hauls, wind speed (knots), wave height (ft), and swell height (ft) were recorded by the chief scientist on each survey vessel, based on a subjective assessment.

Applying the algorithm to the eastern Bering Sea light data required making choices about subroutine settings. We calculated the geometric mean $E_d(Z)$ for 2 m depth bins, which

afforded good vertical resolution of water column light while minimizing stochastic variation between bins. After applying the stepwise filter, casts missing $E_d(Z)$ from at least three consecutive depth bins were excluded from subsequent processing because we intended to use the 0-2 m depth bin as the reference depth, and light can decrease rapidly with depth when water clarity is low. To derive $K_d(Z)$, we constrained the span range between $6/Z_{max} \leq \text{span} \leq 1$, where Z_{max} was the maximum depth for the profile. The constraint ensured a minimum span width of four depth bins, regardless of profile depth. $K_d(Z)$ were calculated at 0.25 m depth intervals.

Evaluation of Algorithm Performance

Given the unique data collection method and approach to data processing, we sought to determine whether derived apparent optical properties were reproducible and precise. To do so, we tested for biases in data collection and algorithm subroutines, evaluated whether derived apparent optical properties yielded a reproducible characterization of light transmission over space and time, and quantified error in near-bottom optical depth, $OD(Z_{max})$, to assess the precision of the apparent optical properties. We defined $OD(Z_{max})$ as $OD(Z)$ for the deepest depth in a cast, typically ~2.5 m above the sea floor.

We hypothesized that upcasts and downcasts may yield different values of $OD(Z_{max})$ due to differences in trawl geometry between deployment (empty net) and retrieval (with catch), or a lagged response of photoelectric cell measurements during downcasts due to a slowing of the change in integer values recorded by the archival tag photoelectric cell as downwelling irradiance decreased. Therefore, we tested for differences in $OD(Z_{max})$ between upcasts and

downcasts using a paired Wilcoxon rank-signed test among hauls where upcasts and downcasts met quality control standards.

It was not clear if using Equation (8) would yield reasonable estimates of $E_d(1)$. Therefore, we tested whether Equation (8) provided a suitable approximation of $E_d(1)$ by estimating $\widehat{E_d(1)}$ for casts which had $E_d(1)$ data, then fit a linear regression between $\ln(E_d(1))$ and $\ln(\widehat{E_d(1)})$.

We hypothesized that wind and waves would influence the rate at which persistent orientation errors were detected by affecting reflectance and refraction of light at the air-sea boundary (Frouin et al. 1989, Kirk 2011). We used linear mixed-effects models to test whether subjective sea state variables (wind speed, wave height, swell height) had a detectable effect on near-surface light. In the light-only model representing no effect of sea state, $\ln((E_d(1))$ was the response, $\ln(E_d(S))$ was included as a fixed effect, and cast direction was included as a random effect. By comparing AIC values, we evaluated support for the light-only model relative to models representing the hypothesis that sea state affected light transmission at the air-sea boundary, which included wind speed, wave height, and swell height as fixed effects.

We sought to assess the precision of derived $OD(Z)$. Because the only data available to conduct such an assessment were archival tag light data, we performed a leave-one-out cross-validation on spatially interpolated $OD(Z_{max})$, for each survey station and year, to estimate prediction error (the sum of measurement error, process error, and model misspecification error) as a proxy for an upper limit on measurement error. For spatial interpolation, $OD(Z_{max})$ were averaged between upcasts and downcasts at a single station, and the aggregate cast location was taken to be the midpoint between the downcast start and upcast end. To reduce the potential for misspecification error to bias prediction error, we tested multiple spatial interpolation methods

for each year. Spatial interpolation methods were inverse-distance weighting, nearest-neighbor distance, Gaussian thin-plate splines, and ordinary kriging. For ordinary kriging, we tested the fit of seven semivariance structures: Gaussian, exponential, spherical, Bessel, power, logarithmic, pentaspherical, Matérn, and Stein's Matérn. The spatial interpolation method with the lowest root-mean square error (RMSE) was used to estimate the upper limit on measurement error. By definition,

$$\mathrm{RMSE_y} = \frac{\sum_{i=1}^{N_y} \sqrt{\left(\mathrm{OD}(Z_{max})_{i,y} - \mathrm{OD}(\widehat{Z_{max}})_{i,y}\right)^2}}{N_y}, \qquad \text{Eqn. (10)}$$

where $\mathrm{RMSE_y}$ is the root mean-square error for year y, N_y is the number of stations successfully sampled during year y, $\mathrm{OD}(Z_{max})_{i,y}$ is the derived near-bottom optical depth for station i in year y, and $\mathrm{OD}(\widehat{Z_{max}})_{i,y}$ is predicted from spatial interpolation.

We evaluated whether $K_d(Z)$ were reproducible by visually inspecting plots, and by calculating the between-cast Pearson correlation coefficient, r, for $K_d(Z)$ for four station-cast combinations. Combinations were upcasts and downcasts from single hauls, 999 randomly selected pairs profiles from adjacent stations (based on nearest-neighbor distance) within year, 999 randomly selected pairs of $K_d(Z)$ profiles from individual stations between years, and 999 randomly selected pairs of $K_d(Z)$ profiles within years. Correlations were calculated for depths where $K_d(Z)$ derived for both profiles. If $K_d(Z)$ were reproducible and consistent, we expected that spatial autocorrelation in optically active constituents of the water column would lead to r being highest between upcasts and downcasts from a single haul and lowest between random pairs of casts within-year, with 'adjacent station' and 'within-station between year' falling between.

RESULTS

Most casts from the eastern Bering Sea continental shelf passed data quality checks, but downcast data passed checks more frequently than upcasts. Out of 10,837 casts (5,419 downcasts, 5,418 upcasts) from 5,419 hauls with light data, 7,887 (72.8%) passed data quality checks. Seventy-nine percent (79.0%) of downcasts passed data quality checks, compared to 66.6% of upcasts. Out of the 5,419 hauls with light data, 4,563 hauls (84.2%) had at least one cast which passed data quality checks. The probabilities of downcasts and upcasts passing data quality checks were not independent, as 56.2% of hauls (3,043/5,419) had both upcasts and downcasts that passed data quality checks, compared to an expected 52.6% under the assumption of independence (one-sample Z-test for proportions; $\chi^2 = 27.64$; $p < 1.5e^{-7}$).

Due to the gently sloping bathymetry of the eastern Bering Sea and tendency for surveys to sample near the center of survey grid cells, the sampling depths at individual stations were highly consistent among years. Overall, 96.9% of casts sampled to a maximum depth within 3 m of the station median maximum sampling depth during 2004–2018. This suggests casts from individual survey stations can be treated as a station-specific apparent optical properties time series.

Omission rates of $E_d(Z)$ by the stepwise point removal subroutine varied by depth and cast direction. Near-surface $E_d(Z)$ were omitted more often than $E_d(Z)$ deeper in the water column and omission rates were higher for upcasts than downcasts (Fig. 4). Deeper in the water column, $E_d(Z)$ were omitted from downcasts at a higher rate than from upcasts.

There was no meaningful effect of sea-state variables on light transmission through the sea surface, based on the comparison of AIC for generalized linear mixed-effects models with and without sea state variables (Table 1). The sea-state model with the lowest AIC included

wind, although, because the effect size was small, sea-state had a negligible effect on light transmission.

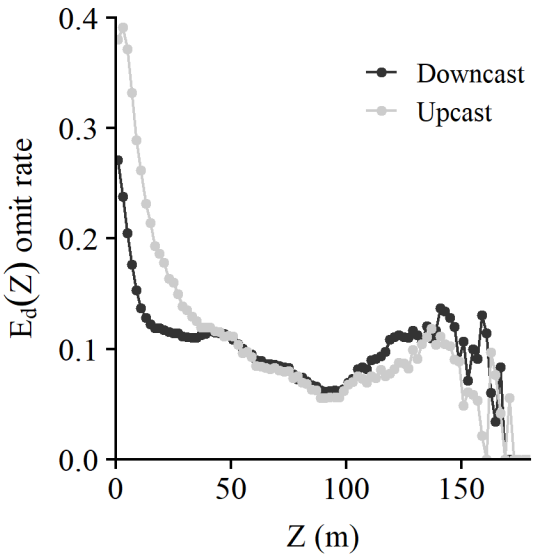

Figure 4. -- Binned $E_d(Z)$ omission rates for the stepwise point removal subroutine, by cast direction and depth bin.

Table 1. -- Results of generalized linear mixed-effects models for sea-state variables showing the fixed effects structure of the model, intercept (β_0), slope parameter for $\log_{10}(E_d(S))$, slope parameter for swell height, wave height, or wind speed (β_2), number of fixed effects parameters (k), and AIC value for the model.

Fixed Effects	**β_0**	**β_1**	**β_2**	**k**	**AIC**
$\log_{10}(E_d(S)) + \varepsilon$	-0.14	0.80		4	7,187.82
$\log_{10}(E_d(S)) + \text{Swell} + \varepsilon$	-0.14	0.80	8.47E-05	5	7,189.81
$\log_{10}(E_d(S)) + \text{Wave} + \varepsilon$	-0.14	0.80	-3.45E-03	5	7,188.03
$\log_{10}(E_d(S)) + \text{Wind} + \varepsilon$	-0.16	0.80	1.35E-03	5	7,187.32

The subroutine for detecting persistent orientation error yielded classifications that were consistent between the direct method and indirect method, and between depth bins. Kernel density distributions of direct method τ and indirect method residuals were bimodal, consistent

with the expectation that persistent orientation errors would result in darker-than-expected $E_d(Z)$ (Fig. 6A-B).There was strong agreement between persistent orientation error detection rates for the direct method and indirect method, as indicated by the strong positive correlation between direct method τ and indirect method residual ($r^2 = 0.80$; Fig. 5C).

The direct method detected persistent orientation errors at a higher rate than the indirect method, although error classifications were the same for 94.0% of casts (Table 2). Between depth bins, persistent orientation error classifications by each method were the same for >96.7% of casts (Table 3). Incorrect deployment of the archival tag assembly may have been prevalent in some years, as persistent orientation error detection rates varied by year (Fig. 7).

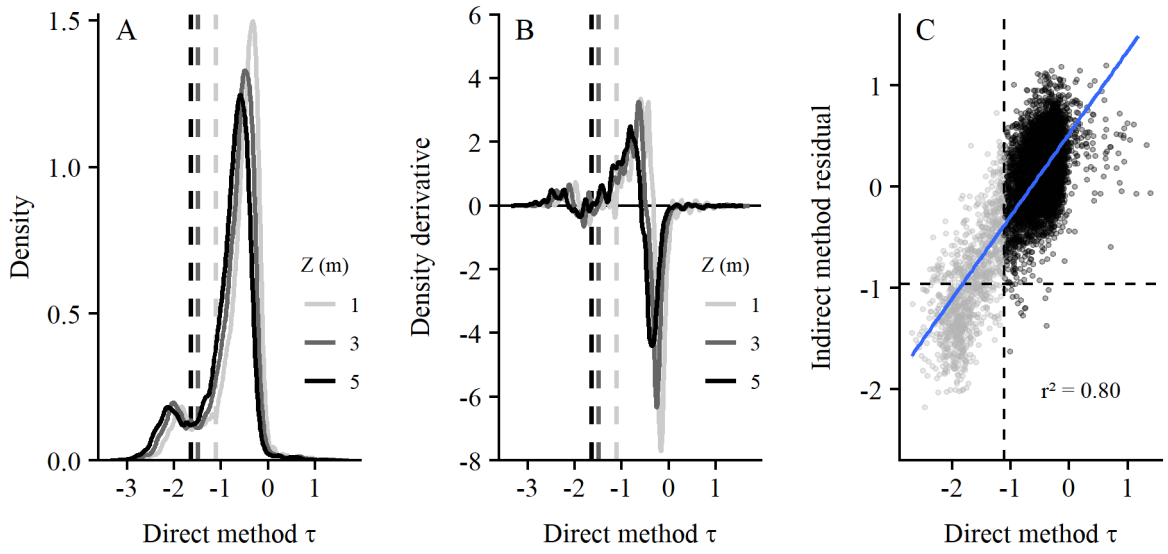

Figure 5. -- Persistent orientation error classification (A) kernel density function, by depth bin, for direct method τ, (B) first derivative of the kernel density function, by depth bin (denoted by line shading). (C) Correlation between direct method residuals and indirect method residuals for the 1 m depth bin. Dashed lines denote thresholds for persistent orientation error, black points denote casts without orientation error, grey points denote casts with orientation error, solid blue line shows regression between direct method τ and indirect method residuals.

For casts where $E_d(1)$ were omitted, the estimated reference light subroutine (Eqn. 6) provided a reasonable approximation of $E_d(1)$, based on the strong correlation between $E_d(1)$ and $\widehat{E_d(1)}$ (Fig. 7). Using the estimate reference light subroutine, prediction errors corresponding with greater than an order of magnitude of variation in light occurred for 0.2% of casts (10/5,696), while the ratio of $\widehat{E_d(1)}/E_d(1)$ was 0.55–1.66 for 95% of casts.

Downcasts yielded $OD(Z_{max})$ that were higher than $OD(Z_{max})$ from upcasts (Fig. 8; paired t-test: N = 1,932; t = 4.01; p = 6.35e-05). However, the mean difference in $OD(Z_{max})$ between upcasts and downcasts was small (95% CI: 0.04–0.12), corresponding with near-bottom light levels 4–13% darker on average for downcasts. The bias was not associated with sampling depth, as Z_{max} did not have a significant influence on $OD(Z_{max})_D$-$OD(Z_{max})_U$ (one-way ANOVA: $F_{1,1931} = 0.06$, p = 0.81). Between-cast differences corresponded with less than an order of magnitude of variation in light ($|OD(Z_{max})_D - OD(Z_{max})_U| < 2.303$) for 97.7% of hauls (1,888/1,933).

Table 2. -- Comparison of persistent orientation error detection rates between the direct method and indirect method. Number in parenthesis denotes the number of casts.

		Direct	
	Orientation	**Good**	**Bad**
Indirect	**Good**	0.869 (7,593)	0.055 (477)
	Bad	0.005 (44)	0.071 (623)

Table 3. -- Comparison of persistent orientation error detection rates between depth bins using the direct method and indirect method. Number in parenthesis denotes the number of casts.

Depth (m)	Direct		Indirect	
	3	**5**	**3**	**5**
1	0.981 (5,315)	0.967 (5,175)	0.983 (6,401)	0.979 (6,251)
3	-	0.983 (6,727)	-	0.972 (8,103)

Derived OD(Z_{max}) were reproducible and consistent, based on prediction error from spatial interpolation. Using the best-fit spatial interpolation method for each year, the median prediction error for OD(Z_{max}) was 0.61 (range: 0.00–9.64), and annual median prediction errors ranged from 0.43 (2004) to 0.86 (2015; Fig. 9). Only 5.8% of casts had prediction errors corresponding with greater than an order of magnitude of variation in light. Sampling coverage affected prediction error from spatial interpolation, as annual mean prediction error was inversely correlated with number of stations with casts that passed data quality control checks (Fig. 10; r = -0.57). There was interannual variation in spatial patterns of near-bottom optical depth on the eastern Bering Sea shelf (Appendix A).

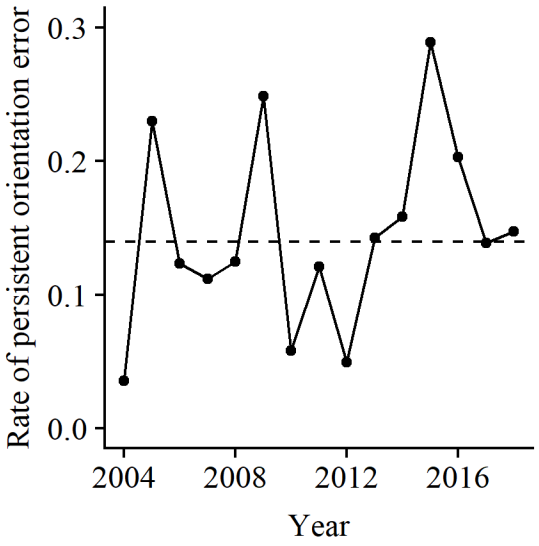

Figure 6. -- Persistent orientation error detection rates by year. Dashed line denotes the mean persistent orientation error detection rate during 2004–2018.

Derived $K_d(Z)$ characterized the vertical structure of light-attenuating features in the water column in a consistent and reproducible manner. Correlation between $K_d(Z)$ profiles was highest for within-haul comparisons (median r = 0.75; Fig. 11), followed by adjacent stations within-year (median r = 0.51), within-station between years (median r = 0.37), and random profiles within-year (median r = 0.06), which was consistent with expectation.

Visual inspection of $K_d(Z)$ profiles revealed similar-shaped profiles at individual stations during multiple years (Appendix B), indicating the vertical structure of light attenuating layers was similar between years. Atypical profiles often occurred at multiple stations in close-proximity during a single year, as shown by vertical profiles of $K_d(Z)$ and transects of OD(Z) along station rows F&G during 2006–2007 (Figs. 1 and 12; Appendix B), indicating atypical profiles were due to environmental variation rather than measurement error.

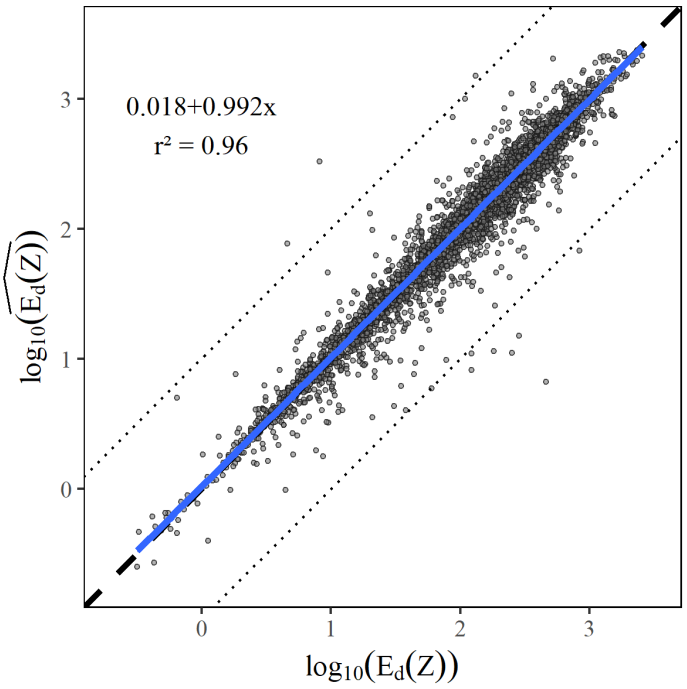

Figure 7. -- Observed $E_d(Z)$ (horizontal axis) versus $E_d(Z)$ estimated for the 1 m depth bin using the 'estimate reference light' subroutine (Eqn. 8).

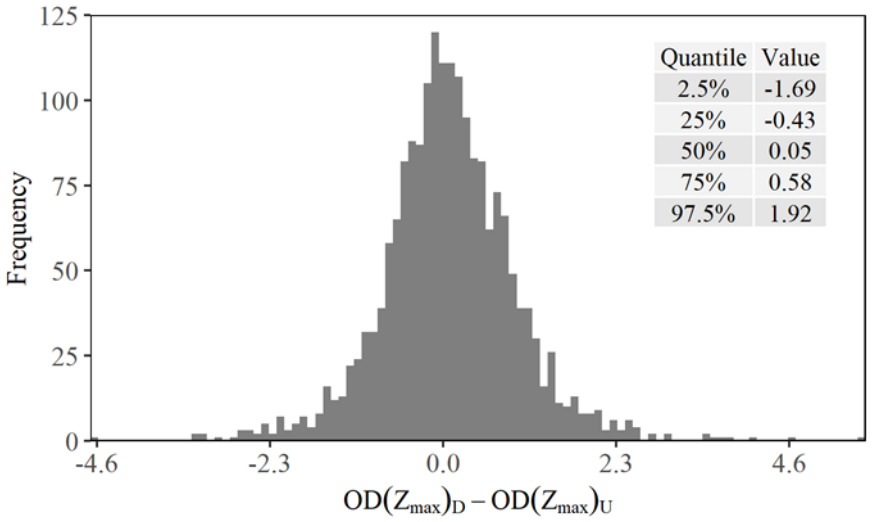

Figure 8. -- Frequency distribution of differences in near-bottom optical depth derived from downcast, $OD(Z_{max})_D$, and upcast, $OD(Z_{max})_U$, data from single hauls. Inset shows the quantiles for differences.

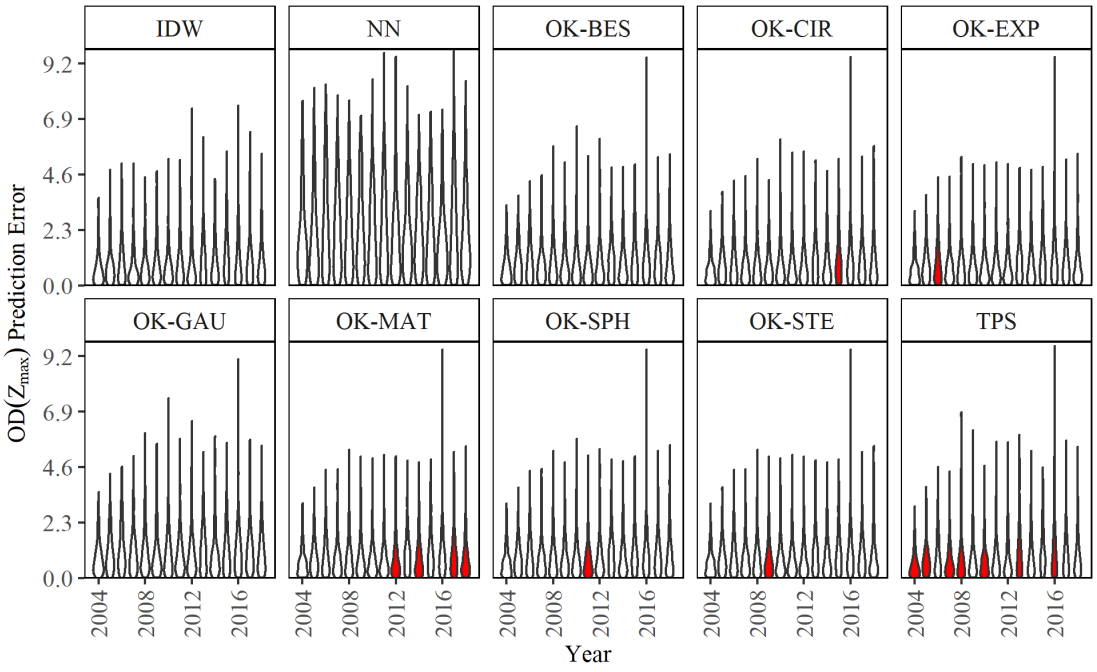

.Figure 9. -- Kernel density distributions of prediction error in near-bottom optical depth, $OD(Z_{max})$, obtained from leave-one-out cross-validation using 10 spatial interpolation methods. Filled bars denote the method with the lowest mean prediction error for a given year. Panel titles denote interpolation method: inverse distance weighting (IDW); nearest neighbor (NN); ordinary kriging with Bessel (OK-BES), circular (OK-CIR), exponential (OK-EXP), gaussian (OK-GAU), Matern (OK-MAT), spherical (OK-SPH), or Stein's Matern (OK-STE) variogram; Gaussian thin-plate spline (TPS).

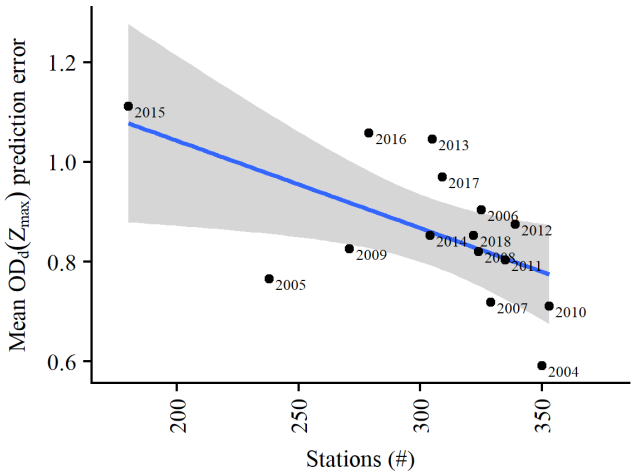

Figure 10. -- Number of stations with good quality cast data versus mean prediction error from best-fit spatial interpolation method for each year. Line and shaded area denote the mean and 95% CI for linear regression.

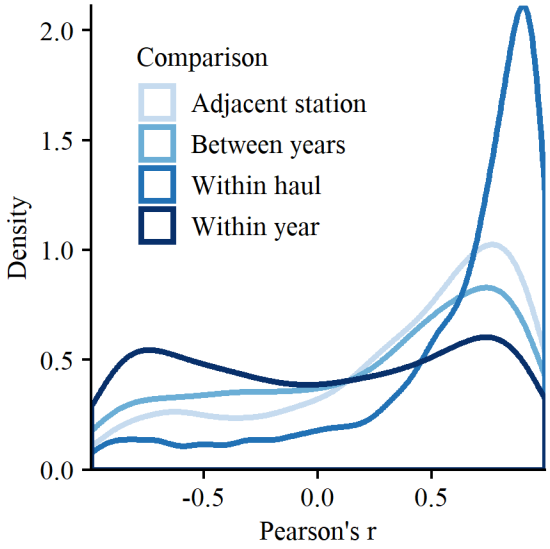

Figure 11. -- Kernel density distribution of Pearson's r for $K_d(Z)$ correlations between upcasts and downcasts from a single haul (Within haul; n = 3,043); random pairs of casts from adjacent stations within year (Adjacent station; n = 999), random pairs of casts from a single station between years (Between years; n = 999), and random pairs of casts within year (Within year; n = 999).

DISCUSSION

Our work demonstrates that light data collected using trawl-mounted archival tags can be used to derive apparent optical properties in coastal marine ecosystems. Based on prediction error from spatial interpolation and comparisons between upcasts and downcasts from single hauls, measurement errors in $OD(Z_{max})$ correspond with less than an order of magnitude of variation in near-bottom light. Within-hauls, profiles of $K_d(Z)$ were similar between upcasts and downcasts, similar-shaped profiles of $K_d(Z)$ occurred at individual stations during multiple years, and atypical profiles of $K_d(Z)$ often occurred at several adjacent stations during a single year. Together, these results suggest the derived apparent optical properties characterized true variation in optically active constituents of the water column over the eastern Bering Sea shelf in a reliable and reproducible manner**.**

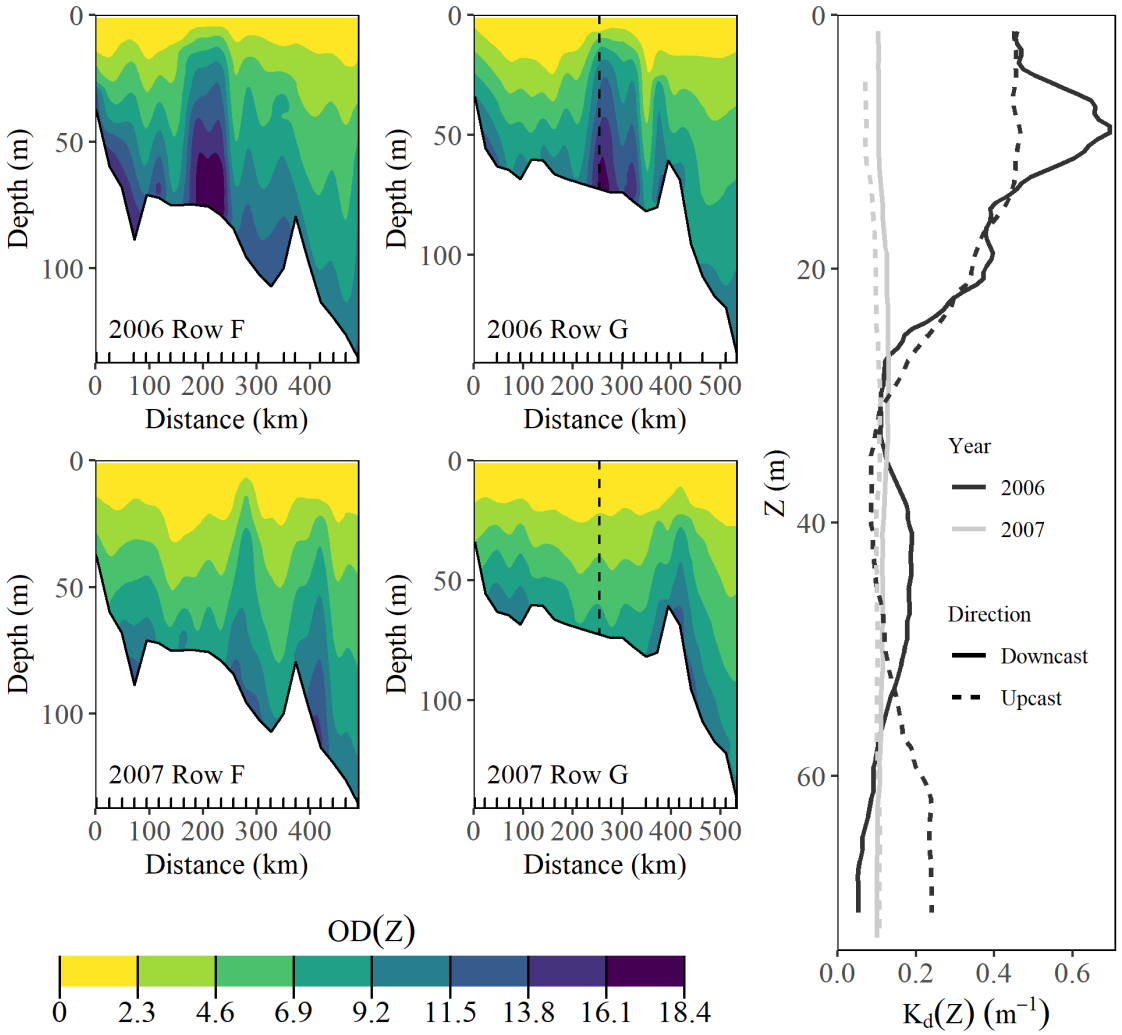

Figure 12. -- Left and center panels: interpolated transects of optical depth, OD(Z), along parallel onshore-offshore (east-west) station rows F & G (Fig. 2) during 2006–2007. Tick marks along the horizontal axis denote locations with haul data which passed quality control checks. Dashed lines on the center panels denote location of station G-04. Right panel: profiles of the vertical attenuation coefficient of downwelling irradiance, $K_d(Z)$, for upcasts and downcasts from station G-04 during 2006–2007. During each year, casts were collected ~1.5 nmi apart.

The plausible upper limit on measurement error in $OD(Z_{max})$ in the eastern Bering Sea provides insight into measurement error that may be expected if the algorithm is used to derive apparent optical properties from other regions. The gridded survey design used in the eastern Bering Sea provided an ideal opportunity to quantify error over many years, in a manner that

may not be possible in regions with different sampling schemes and complex bathymetry. Among years, the lowest median prediction error was 0.42, during 2004, the year with the highest proportion of stations with casts passing quality control checks. Because prediction error is the sum of process error, measurement error, and misspecification error, we suggest the plausible upper limit on measurement error in $OD(Z_{max})$ for a single cast is likely less than 0.42.

It is unclear why $OD(Z_{max})$ was higher for downcasts compared to upcasts from the same haul. Differences in trawl geometry between deployment and retrieval may have caused the orientation of the archival tag photoelectric cell, relative to angular distribution of the downwelling light field, to differ between downcasts and upcasts. However, between-cast differences in $OD(Z_{max})$ were relatively small, indicating that over the ~1.5 nmi distance between downcasts and upcasts, $OD(Z_{max})$ from either an upcast or downcast is likely to provide a representative approximation of $OD(Z_{max})$ at a station.

Although we did not detect a meaningful effect of wave height, swell height, or wind speed on near-surface light measurements from the eastern Bering Sea, sea state does affect the transmission of light through the sea surface. Bubbles formed by breaking waves increase reflectance at the sea surface and increase backscattering below the sea surface, which reduces light transmission (Frouin et al. 1996, Stramski and Tegowski 2001). The height and frequency of waves affects the amount of variation and frequency of variation in light in a fixed location (Wijesekera et al. 2005). We may not have detected an effect due to high process noise in near-surface light measurements, a lack of sampling under conditions that would increase reflectance, or observer bias. Frouin et al. (1996) suggested that white-caps caused by wind speeds > 8 $m \cdot s^{-1}$ (15.6 knots) would increase reflectance to levels which would affect remote sensing. During 2004–2018, wind-speeds >15.6 knots were reported for 22.4% of hauls. Wave and wind data

were based on subjective observations, so observer biases may have masked effects of sea state on light.

High orientation error rates during some years may have been a result of high prevalence of incorrect deployment of the archival tag on the bottom-trawl gear. During some years and on some vessels, error rates were high, and seemingly random, which may suggest inconsistent deployment of the archival tag on the trawl gear. At other times, crew changes and survey leg breaks were followed by a consecutive series of orientation errors, which were followed by consistently correct orientation later-on. Design changes to the archival tag base plate may be help to reduce orientation error rates.

Supplementing or replacing archival tags with purpose-built sampling equipment would improve monitoring of the subsurface visual environment. Archival tag photo electric cells were not equipped with cosine correcting diffusers, so there may have been angle-dependent biases in light measurements, especially near the sea surface (Duntley 1963). Archival tag photoelectric cells did not provide information about the spectral distribution of light, which is important for vision because animal photoreceptors are sensitive to specific wavelengths of light (e.g., Britt et al. 2001, Britt 2009, Cronin et al. 2014). Passive spectral measurements could be obtained using a multispectral irradiance meter or archival tags equipped with photoelectric cells that have color filters. The vertical attenuation coefficient of downwelling irradiance provides information about water clarity, although it does not provide direct information about how constituents of the water column affect the propagation of image-forming light for vision. Propagation of image-forming light is affected by beam attenuation and forward scattering, inherent optical properties, in addition to the diffuse attenuation coefficient (Lee et al. 2015). Direct information about how

variation in water clarity affects image propagation can be gleaned from measurements of beam attenuation obtained using a multispectral integrating nephelometer or beam transmissometer.

The subroutines used to detect persistent orientation errors do not provide a basis for detecting orientation or obstruction of the archival tag deep in the water column or while the trawl is on-bottom. Our choice of the maximum depth bin used to detect persistent orientation errors was primarily based on a need to estimate light for the 0-2 m depth bin for casts where light data were missing or omitted. However, an additional consideration was that spatial and temporal variation in water clarity causes a depth-dependent increase in variance in the relationship between surface and subsurface light. As such, algorithm subroutines for detecting persistent orientation errors will become less reliable as the depth of measurements used to detect persistent orientation errors increases.

A notable shortcoming of our study is that we did not regularly evaluate the accuracy of light measurements, or assess the spectral response of archival tags. The conversion function in the algorithm is based on the spectral response of archival tags under green (555 nm) and white (broad visible spectrum) light. Future research is needed to assess the accuracy and response of archival tag light measurements under a variety of light spectra by comparing archival tag measurements to measurements from purpose-built light sensors. Then, in situ studies should be conducted to determine whether archival tag light measurements can reasonably predict measurements from purpose-built equipment. Considering the precision and reproducibility of our measurements, it seems likely that reliable empirical relationships would exist. Indeed, O'Toole et al. (2014) found that attenuation coefficients derived using light measurements from TDR-Mk series archival tags attached to southern elephant seals had a strong correlation with chlorophyll-a concentration derived from satellite measurements of the Southern Ocean.

However, although the accuracy of the raw light measurements is not known, our approach to deriving apparent optical properties only assumed tags had a consistent spectral response among tags and a consistent intensity-response relationship for individual tags, with no consideration for absolute light sensitivity or measurement accuracy.

Improvements to sampling equipment could clarify causes of persistent orientation errors and provide insight into whether they persist throughout hauls. Although archival tags have often been used to measure light during scientific bottom-trawls, methods for detecting persistent orientation errors had not been developed (Weinberg and Munro 1999, Kotwicki et al. 2009, Ryer et al. 2010, Bradburn and Keller 2015). The subroutine for detecting orientation errors assumes that orientation errors would result in darker-than-normal $E_d(Z)$. However, we were unable to directly test that assumption. We suspect that persistent orientation errors may have occurred due to improper deployment of the archival tag on the bottom-trawl (e.g., upside-down) or variation in the geometric configuration of the trawl gear. Deploying a three-axis accelerometer on the archival tag base plate, along with the archival tag, would provide information about archival tag orientation, allowing assessment of whether darker-than-normal $E_d(Z)$ were caused by changes in the orientation of the archival tag.

An alternative to using archival tags would be to deploy purpose-built light sensors during bottom-trawl surveys. Doing so would require ruggedized equipment capable of withstanding the harsh operating conditions demanded by bottom-trawl surveys. If such sampling were conducted, our algorithm could likely be adapted to derive apparent optical properties from the purpose-built equipment, as many of the challenges we encountered were a product of deploying sensors on trawl gear rather than being specific to the sampling equipment.

ACKNOWLEDGMENTS

We express our gratitude to Alex De Robertis, Kelly Kearney, and Stephani Zador for their constructive reviews of an earlier version of this manuscript. We thank Dave Beauchamp for contributions to the design and structure of our study. We thank survey participants, and the masters and crews of FV *Alaska Knight*, FV *Aldebaran*, FV *Arcturus*, FV *Ocean Explorer*, and FV *Vesteraalen* for their assistance collecting data over many years. Funding for this research was provided by the NOAA Fisheries and the Environment (FATE) Program.

CITATIONS

Aiken, J., and I. Bellan. 1990. Optical oceanography: an assessment of a towed method. Pages 39–57 *in* P. J. Herring, A. K. Campbell, M. Whitfield, and L. Maddock (eds.). Life and Light in the Sea. Cambridge University Press.

Aksnes, D. L. 2007. Evidence for visual constraints in large marine fish stocks. Limnol. Oceanogr. 52(1):198–203.

Aksnes, D. L., J. Nejstgaard, E. Sædberg, and T. Sørnes. 2004. Optical control of fish and zooplankton populations. Limnol. Oceanogr. 49(1):233–238.

Aksnes, D. L., and A. Utne. 1997. A revised model of visual range in fish. Sarsia 82:137–147.

Baker, K. S., and R. C. Smith. 1979. Quasi-inherent characteristics of the diffuse attenuation coefficient for irradiance. Ocean Optics IV 208:60–63.

Baker, M. R., and A. B. Hollowed. 2014. Delineating ecological regions in marine systems: Integrating physical structure and community composition to inform spatial management in the eastern Bering Sea. Deep-sea Res. Pt. II 109:215–240. Elsevier.

Beauchamp, D. A., C. M. Baldwin, J. L. Vogel, and C. P. Gubala. 1999. Estimating diel, depth-specific foraging opportunities with a visual encounter rate model for pelagic piscivores. Can. J. Fish. Aquat. Sci. 56(S1):128–139.

Bradburn, M. J., and A. A. Keller. 2015. Impact of light on catch rate of four demersal fish species during the 2009-2010 U.S. west coast groundfish bottom trawl survey. Fish. Res. 164:193–200. Elsevier B.V.

Britt, L. L. 2009. Ontogenetic changes in the visual ecology of northeast Pacific marine fishes. University of Washington, Seattle WA.

Britt, L. L., E. R. Loew, and W. N. McFarland. 2001. Visual pigments in the early life stages of Pacific northwest marine fishes. J. Exp. Biol. 204(14):2581–2587.

Buijse, A. D., L. A. Schaap, and T. P. Bult. 1992. Influence of water clarity on the catchability of six freshwater. Can. J. Fish. Aquat. Sci. 49:885–893.

Capuzzo, E., S. J. Painting, R. M. Forster, N. Greenwood, D. T. Stephens, and O. A. Mikkelsen. 2013. Variability in the sub-surface light climate at ecohydrodynamically distinct sites in the North Sea. Biogeochemistry 113(1–3):85–103.

Cokelet, E. D. 2016. 3-D water properties and geostrophic circulation on the eastern Bering Sea shelf. Deep-sea Res. Pt. II: Top. Stud. Oceanogr. 134:65–85. Elsevier.

Conner, J., D. Nichol, and R. R. Lauth. 2017. Results of the 2015 eastern Bering Sea continental shelf bottom trawl survey of groundfish and invertebrate resources. U. S. Dep. Commer., NOAA Tech. Memo. NMFS-AFSC-353, 154 p.

Cronin, T. W., S. Johnsen, N. J. Marshall, and E. J. Warrant. 2014. Visual Ecology. Princeton University Press, Princeton, New Jersey.

Douglas, R. H., and C. W. Hawryshyn. 1990. Behavioral studies of fish vision: an Analysis of visual capabilities. Pages 373–418 *in* R. Douglas and M. Djamgoz (eds.) The Visual System of Fish. Springer, Dordrecht.

Duntley, S. Q. 1963. Light in the sea. J. Optical Soc. Am. 53(2):214–233.

Eiane, K., D. L. Aksnes, E. Bagøien, and S. Kaartvedt. 1999. Fish or jellies — a question of visibility ? Limnol. Oceanogr. 44(5):1352–1357.

Fiksen, Ø., D. L. Aksnes, M. H. Flyum, and J. Giske. 2002. The influence of turbidity on growth and survival of fish larvae: a Numerical analysis: Hydrobiologia 484: 49–59.

Frouin, R., D. W. Lingner, C. Gautier, K. S. Baker, and R. C. Smith. 1989. A simple analytical formula to compute clear sky total and photosynthetically available solar irradiance at the ocean surface. J. Geophys. Res. 94(C7):9731.

Frouin, R., M. Schwindling, and P.-Y. Deschamps. 1996. Spectral reflectance of sea foam in the visible and near-infrared: In situ measurements and remote sensing implications. J. Geophys. Res. 101(C6):14361–14371.

Glass, C. W., and C. S. Wardle. 1989. Comparison of the reactions of fish to a trawl gear, at high and low light intensities. Fish. Res. 7(3):249–266.

Glass, C. W., C. S. Wardle, and W. Mojsiewicz. 1986. A light intensity threshold for schooling in the Atlantic mackerel, *Scomber scombrus*. J. Fish Biol. 29(Supplement A):71–81.

Heidenreich, N. B., A. Schindler, and S. Sperlich. 2013. Bandwidth selection for kernel density estimation: A review of fully automatic selectors. AStA Adv. Stat. Analysis 97(4):403–433.

Henderson, M. A., and T. G. Northcote. 1985. Visual prey detection and foraging in sympatric cutthroat trout (*Salmo clarki clarki*) and Dolly Varden (*Salvelinus malma*). Can. J. Fish. Aquat. Sci. 42:785–790.

Hoff, G. R. 2016. Results of the 2016 eastern Bering Sea upper continental slope survey of groundfish and invertebrate resources. U. S. Dep. Commer., NOAA Tech. Memo. NMFS-AFSC-256, 272 p.

Holsman, K. K., and K. Aydin. 2015. Comparative methods for evaluating climate change impacts on the foraging ecology of Alaskan groundfish. Mar. Ecol. Progr. Ser. 521:217–235.

Hurst, T. P., C. H. Ryer, J. M. Ramsey, and S. A. Haines. 2007. Divergent foraging strategies of three co-occurring north Pacific flatfishes. Mar. Biol. 151(3):1087–1098.

Hurvich, C. M., J. S. Simonoff, and C.-L. Tsai. 1998. Smoothing parameter selection in nonparametric regression using an improved Akaike information criterion. J. Royal Stat. Soc. B 60(2):271–293.

Jaud, T., A.-C. Cile Dragon, J. V. Garcia, and C. Guinet. 2012. Relationship between chlorophyll a concentration, light attenuation and diving depth of the southern elephant seal *Mirounga leonina*. PLoS ONE 7(10):e47444.

Kaartvedt, S., W. Melle, T. Knutsen, and H. R. Skjoldal. 1996. Vertical distribution of fish and krill beneath water of varying optical properties. Mar. Ecol. Progr. Ser. 136(1–3):51–58.

Kawana, K. 1975. Turbidity distribution of the Bering Sea in the summer. Bull. Faculty Fish. Hokkaido Univ. 26(1):73–86.

Keele, L. J. 2008. Semiparametric Regression for the Social Sciences. John Wiley & Sons Ltd, Chichester.

Kirk, J. T. O. 2011. Light and photosynthesis in aquatic ecosystems, 3rd edition. Cambridge University Press, New York.

Klevjer, T. A., X. Irigoien, A. Røstad, E. Fraile-Nuez, V. M. Benítez-Barrios, and S. Kaartvedt. 2016. Large scale patterns in vertical distribution and behaviour of mesopelagic scattering layers. Sci. Rep. 6 (January):1–11. Nature Publishing Group.

Kotwicki, S., J. K. Horne, A. E. Punt, and J. N. Ianelli. 2015. Factors affecting the availability of walleye pollock to acoustic and bottom trawl survey gear. ICES J. Mar. Sci. 72(5):1425–1439.

Kotwicki, S., J. N. Ianelli, and A. E. Punt. 2014. Correcting density-dependent effects in abundance estimates from bottom-trawl surveys. ICES J. Mar. Sci. 71:1107–1116.

Kotwicki, S., P. H. Ressler, J. N. Ianelli, A. E. Punt, and J. K. Horne. 2018. Combining data from bottom trawl and acoustic surveys to estimate an index of abundance for semipelagic species. Can. J. Fish. Aquat Sci. 75:60–71.

Kotwicki, S., A. De Robertis, P. von Szalay, and R. Towler. 2009. The effect of light intensity on the availability of walleye pollock (*Theragra chalcogramma*) to bottom trawl and acoustic surveys. Can. J. Fish. Aquat. Sci. 66(6):983–994.

Laman, E. A., S. Kotwicki, and C. N. Rooper. 2014. Correlating environmental and biogenic factors with abundance and distribution of Pacific ocean perch (*Sebastes alutus*) in the Aleutian Islands, Alaska. Fish. Bull., U.S. 113(3):270–289.

Laman, E. A., C. N. Rooper, K. Turner, S. Rooney, D. W. Cooper, and M. Zimmermann. 2018. Using species distribution models to describe essential fish habitat in Alaska. Can. J. Fish. Aquat. Sci. 75(8):1230–1255.

Langbehn, T. J., and Ø. Varpe. 2017. Sea-ice loss boosts visual search: Fish foraging and changing pelagic interactions in polar oceans. Global Change Biol. 23(12):5318–5330.

Lee, Z., S. Shang, C. Hu, K. Du, A. Weidemann, W. Hou, J. Lin, and G. Lin. 2015. Secchi disk depth: a New theory and mechanistic model for underwater visibility. Remote Sensing Environ. 169:139–149. Elsevier B.V.

Lovvorn, J. R., C. L. Baduini, and G. L. Hunt Jr. 2001. Modeling underwater visual and filter feeding by planktivorous shearwaters in unusual sea conditions. Ecology 82(8):2342–2356.

Lythgoe, J. 1979. The Ecology of Vision. Clarendon Press, Oxford, United Kingdom.

Mazur, M. M., and D. A. Beauchamp. 2003. A comparison of visual prey detection among species of piscivorous salmonids: Effects of light and low turbidities. Environ. Biol. Fish. 67(4):397–405.

McManus, D. A., and C. S. Smyth. 1970. Turbid bottom water on the continental shelf of the northern Bering Sea. J. Sediment. Petrol. 40(3):869–873.

Mobley, C. D. 1994. Light and water: Radiative transfer in natural waters. Academic Press.

Naik, P., E. J. D'Sa, J. I. Goés, and H. R. Gomes. 2010. Assessment of particulate absorption properties in the southeastern Bering Sea from in-situ and remote sensing data. J. Appl. Remote Sensing 4:43520–43561.

Naik, P., E. J. D'Sa, H. do R. Gomes, J. I. Goés, and C. B. Mouw. 2013. Light absorption properties of southeastern Bering Sea waters: Analysis, parameterization and implications for remote sensing. Remote Sensing Environ. 134:120–134. Elsevier Inc.

Nelson, G. A. 2018. fishmethods: Fishery science methods and models. R package.

O'Toole, M. D., M. A. Lea, C. Guinet, and M. A. Hindell. 2014. Estimating trans-seasonal variability in water column biomass for a highly migratory, deep diving predator. PLoS ONE 9(11).

Olla, B. L., M. W. Davis, and D. C. Rose. 2000. Differences in orientation and swimming of walleye pollock *Theragra chalcogramma* in a trawl net under light and dark conditions: concordance between rield and laboratory observations. Fish. Res. 44:261–266.

Olla, B. L., M. W. Davis, and C. B. Schreck. 1997. Effects of simulated traling on sablefish and walleye pollock: the role of light intensity, net velocity and towing duration. J. Fish Biol. 50:1181–1194.

Roe, H. S. J. 1983. Vertical distributions of euphausiids and fish in relation to light intensity in the Northeastern Atlantic. Mar. Biol. 77(3):287–298.

Rohan, S. K. 2020. trawllight: Derive apparent optical properties from trawl-mounted light sensors. https://rdrr.io/github/sean-rohan/trawllight/

Rooper, C. N., G. R. Hoff, D. E. Stevenson, J. W. Orr, and I. B. Spies. 2019. Skate egg nursery habitat in the eastern Bering Sea: A predictive model. Mar. Ecol. Progr. Ser. 609:163–178.

Røstad, A., S. Kaartvedt, and D. L. Aksnes. 2016. Light comfort zones of mesopelagic acoustic scattering layers in two contrasting optical environments. Deep-sea Res. Pt. I: Oceanogr. Res. Papers 113:1–6. Elsevier.

Ryer, C. H. 2008. A review of flatfish behavior relative to trawls. Fish. Res. 90:138–146.

Ryer, C. H., and L. A. K. Barnett. 2006. Influence of illumination and temperature upon flatfish reactivity and herding behavior: Potential implications for trawl capture efficiency. Fish. Res. 81(2–3):242–250.

Ryer, C. H., and B. L. Olla. 1998. Effect of light on juvenile walleye pollock shoaling and their interaction with predators. Mar. Ecol. Progr. Ser. 167:215–226.

Ryer, C. H., and B. L. Olla. 1999. Light-induced changes in the prey consumption and behavior of two juvenile planktivorous fish. Mar. Ecol. Progr. Ser. 181:41–51.

Ryer, C. H., and B. L. Olla. 2000. Avoidance of an approaching net by juvenile walleye pollock *Theragra chalcogramma* in the laboratory: the Influence of light intensity. Fish. Res. 45:195–199.

Ryer, C. H., C. S. Rose, and P. J. Iseri. 2010. Flatfish herding behavior in response to trawl sweeps: a Comparison of diel responses to conventional sweeps and elevated sweeps. Fish. Bull., U.S. 108(2):145–154.

Savchuk, O. Y., J. D. Hart, and S. J. Sheather. 2010. Indirect cross-validation for density estimation. J. Am. Stat. Assoc. 105(489):415–423.

Savidge, G., D. R. Turner, P. H. Burkill, A. J. Watson, M. V. Angel, R. D. Pingree, H. Leach, and K. J. Richards. 1992. The BOFS 1990 spring bloom experiment : Temporal evolution and spatial variability of the hydrographic field. Progr. Oceanogr. 29:235–281.

Sigler, M. F., P. J. Stabeno, L. B. Eisner, J. M. Napp, and F. J. Mueter. 2014. Spring and fall phytoplankton blooms in a productive subarctic ecosystem, the eastern Bering Sea, during 1995-2011. Deep-sea Res. Pt. II: Top. Stud. Oceanogr. 109:71–83. Elsevier.

Smith, R. C., and K. S. Baker. 1984. The analysis of ocean optical data. Pages 119–126 *in* M. A. Blizard (ed.) SPIE, Ocean Optics VII.

Sørnes, T. A., and D. L. Aksnes. 2004. Predation efficiency in visual and tactile zooplanktivores. Limnol. Oceanogr. 49(1):69–75.

Staby, A., and D. L. Aksnes. 2011. Follow the light — diurnal and seasonal variations in vertical distribution of the mesopelagic fish *Maurolicus muelleri*. Mar. Ecol. Progr. Ser. 422:265–273.

Stapanian, M. A., P. M. Kocovsky, and J. V. Adams. 2009. Change in diel catchability of young-of-year yellow perch associated with establishment of dreissenid mussels. Freshw. Biol. 54(8):1593–1604.

Stauffer, G. 2004. NOAA protocols for groundfish bottom-trawl surveys of the Nation's fishery resources. U. S. Dep. Commer., NOAA Tech. Memo. NMFS-F/SPO-65, 205 p.

Stevenson, D. E., and R. R. Lauth. 2019. Bottom trawl surveys in the northern Bering Sea indicate recent shifts in the distribution of marine species. Polar Biol. 42(2):407–421. Springer Berlin Heidelberg.

Stramski, D., and J. Tegowski. 2001. Effects of intermittent entrainment of air bubbles by breaking wind waves on ocean reflectance and underwater light field. J. Geophys. Res.: Oceans 106(C12):31345–31360.

von Szalay, P. G., N. W. Raring, C. N. Rooper, and E. A. Laman. 2017. Data Report: 2016 Aleutian Islands Bottom trawl survey. U. S. Dep. Commer., NOAA Tech. Memo. NMFS-AFSC-349, 150 p.

Utne-Palm, A. 2002. Visual feeding of fish in a turbid environment: Physical and behavioural aspects. Mar. Freshw. Behav. Physiol. 35(1–2):111–128.

Vacquié-Garcia, J., J. Mallefet, F. Bailleul, B. Picard, and C. Guinet. 2017. Marine bioluminescence: measurement by a classical light sensor and related foraging behavior of a deep diving predator. Photochem. Photobiol. 93(5):1312–1319.

Varpe, Ø., M. Daase, and T. Kristiansen. 2015. A fish-eye view on the new Arctic lightscape. ICES J. Mar. Sci. 72(9):2532–2538.

Vestfals, C. D., L. Ciannelli, and G. R. Hoff. 2016. Changes in habitat utilization of slope-spawning flatfish across a bathymetric gradient. ICES J. Mar. Sci. 73(7):1875–1889.

Vogel, J. L., and D. A. Beauchamp. 1999. Effects of light, prey size, and turbidity on reaction distances of lake trout (*Salvelinus namaycush*) to salmonid prey. Can. J. Fish. Aquat. Sci. 56(7):1293–1297.

Wand, M. ., and M. C. Jones. 1994. Kernel smoothing. Monographs on statistics and applied probability. Vol. 60. Chapman and Hall, London.

Warrant, E. J., and N. A. Locket. 2004. Vision in the deep sea. Biol. Rev. 79(3):671–712.

Weinberg, K. L., and P. T. Munro. 1999. The effect of artificial light on escapement beneath a survey trawl. Fish. Sci. 56:266–274.

Wernand, M. R., H. J. van der Woerd, and W. W. C. Gieskes. 2013. Trends in ocean colour and chlorophyll concentration from 1889 to 2000, worldwide. PLoS ONE 8(6):e63766.

Wijesekera, H., W. S. Pegau, and T. Boyd. 2005. Effect of surface waves on the irradiance distribution in the upper ocean. Opt. Express. 13(23):9257–9264.

Wood, S. N. 2011. Fast stable restricted maximum likelihood and marginal likelihood estimation of semiparametric generalized linear models. J. Royal Stat. Soc. Ser. B: Stat. Methodol. 73(1):3–36.

Yeung, C., and M.-S. Yang. 2018. Spatial variation in habitat quality for juvenile flatfish in the southeastern Bering Sea and its implications for productivity in a warming ecosystem. J. Sea Res. 139(June):62–72.

APPENDIX A: OD(Z_{max}) BY YEAR

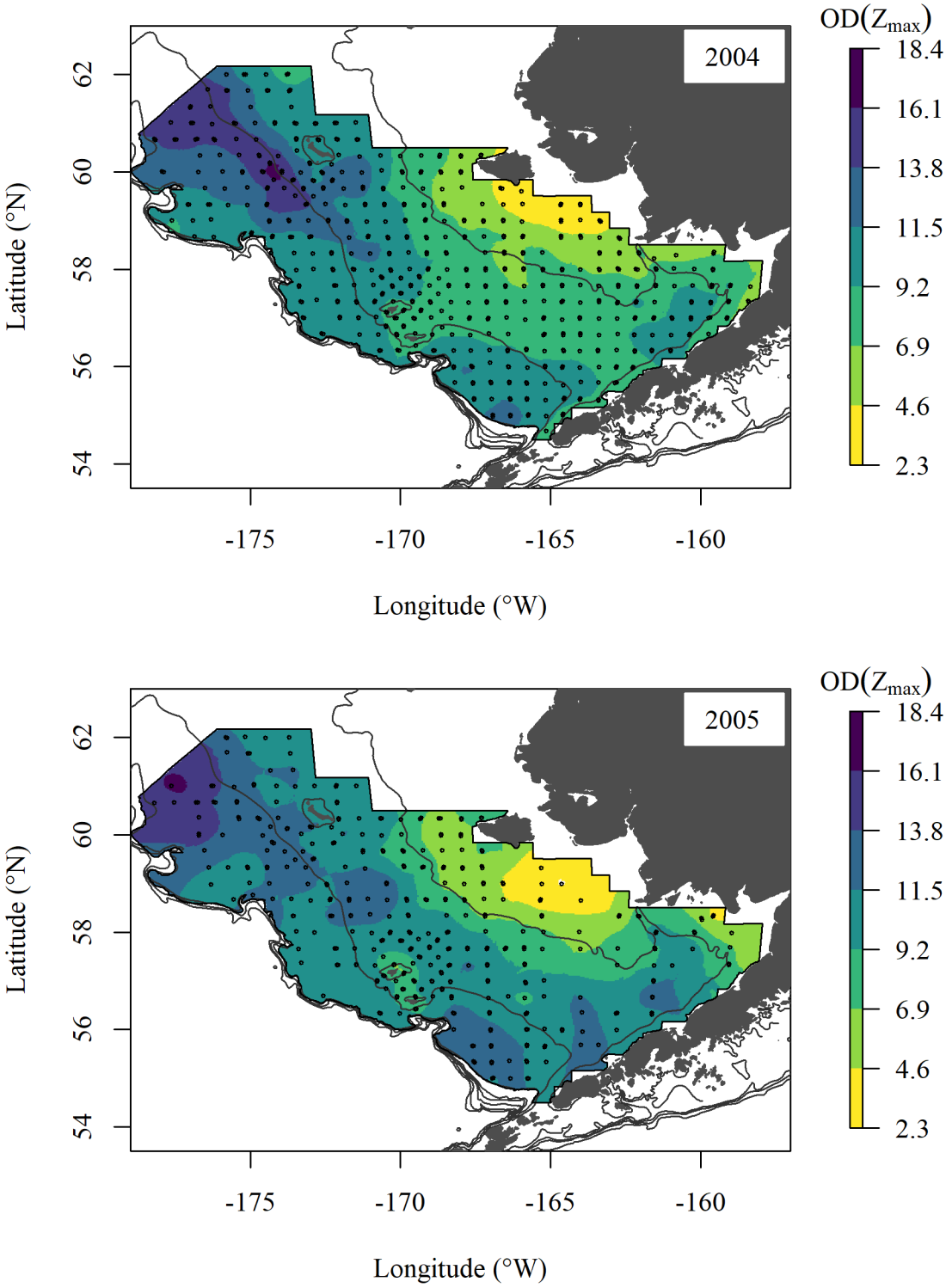

Appendix Figure A-1. -- Near-bottom optical depth in the eastern Bering Sea continental shelf survey area, by year. Points denote stations with cast data which met quality control standards.

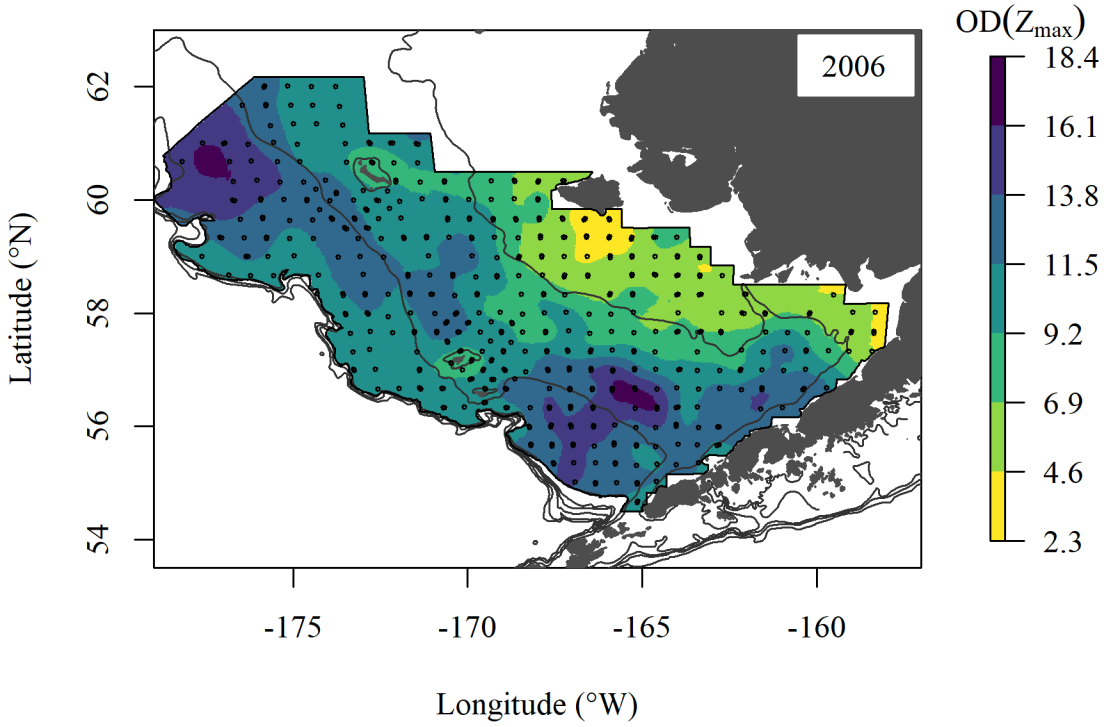

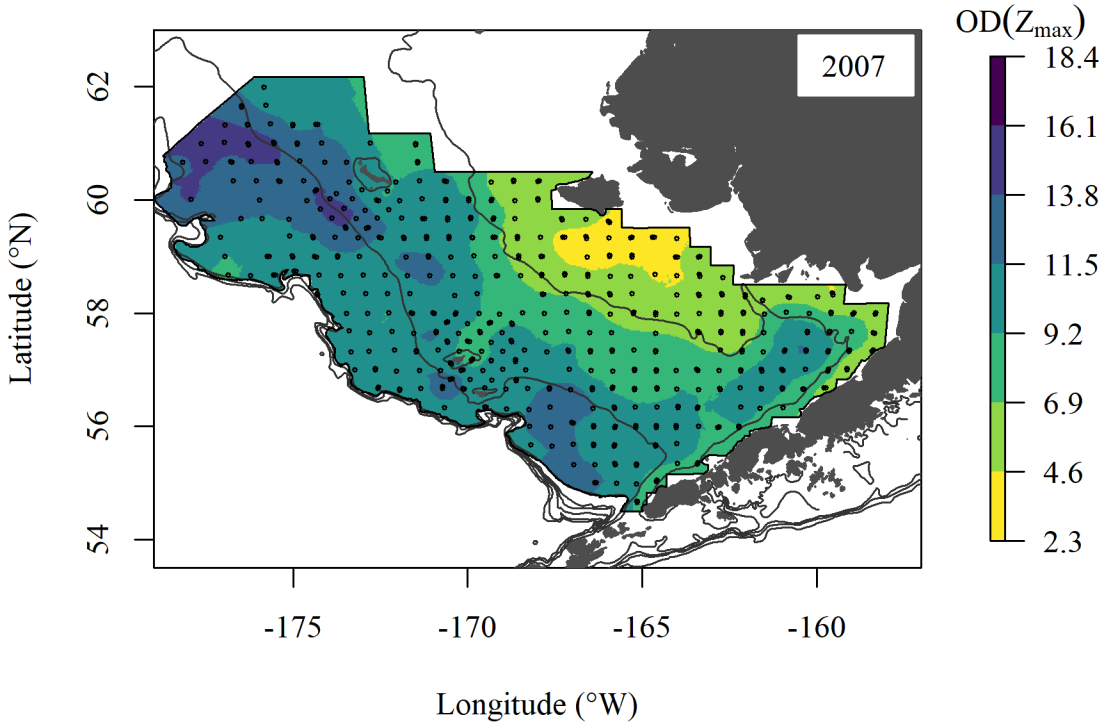

Appendix Figure A-1. -- Continued.

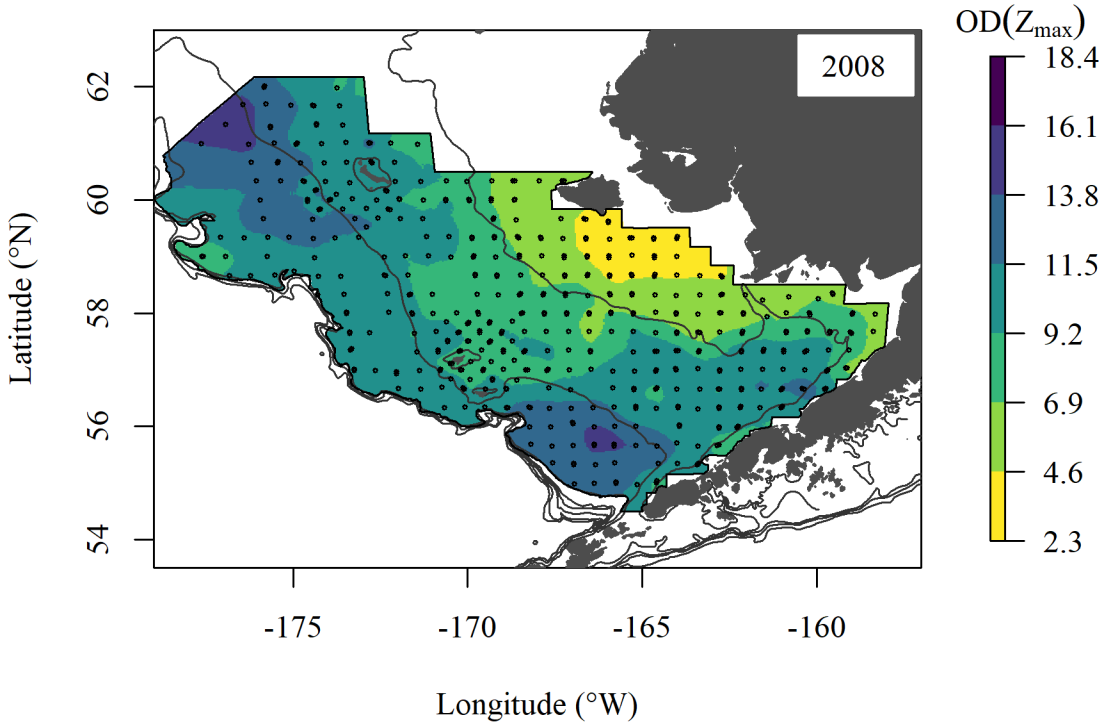

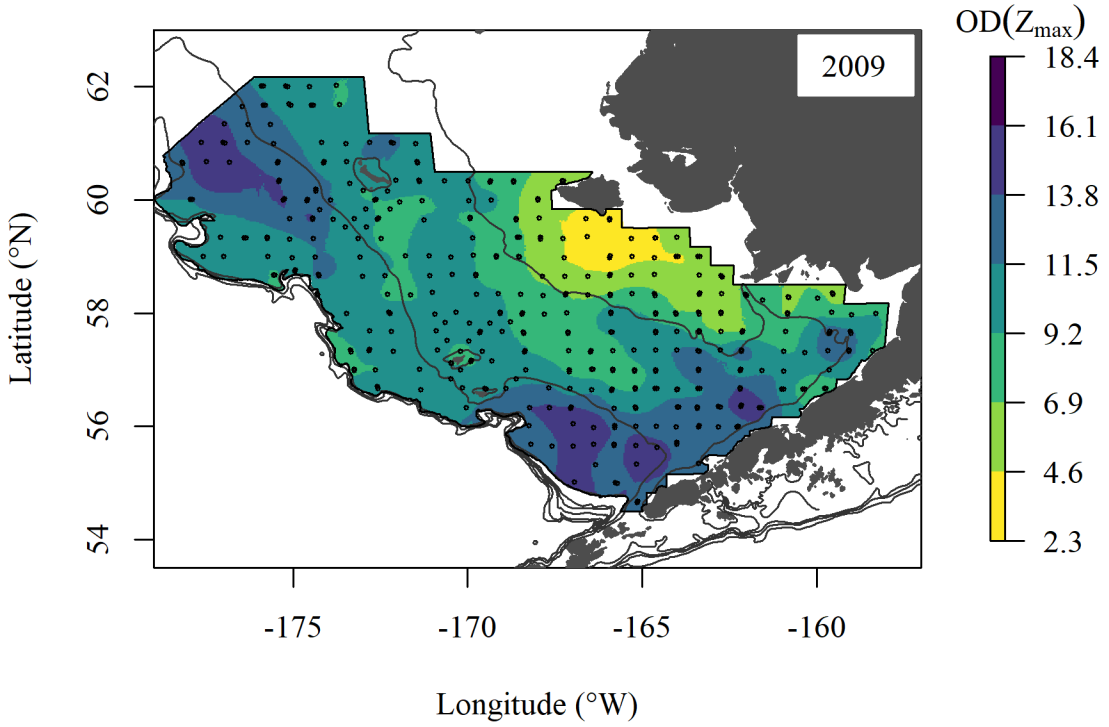

Appendix Figure A-1. -- Continued.

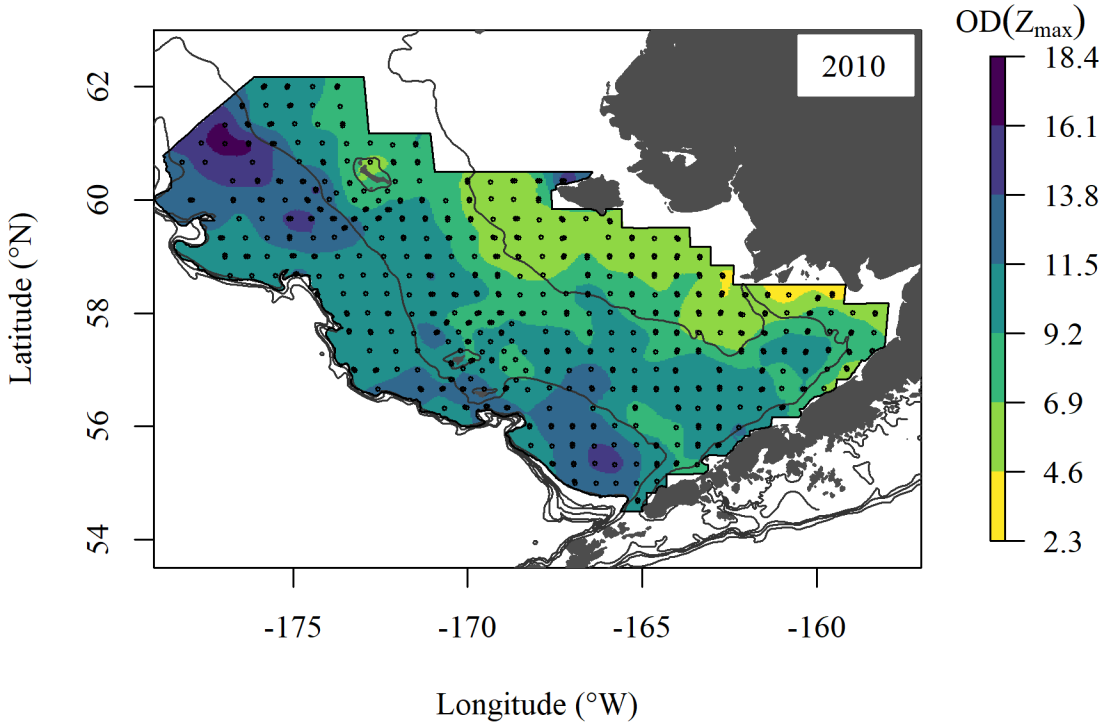

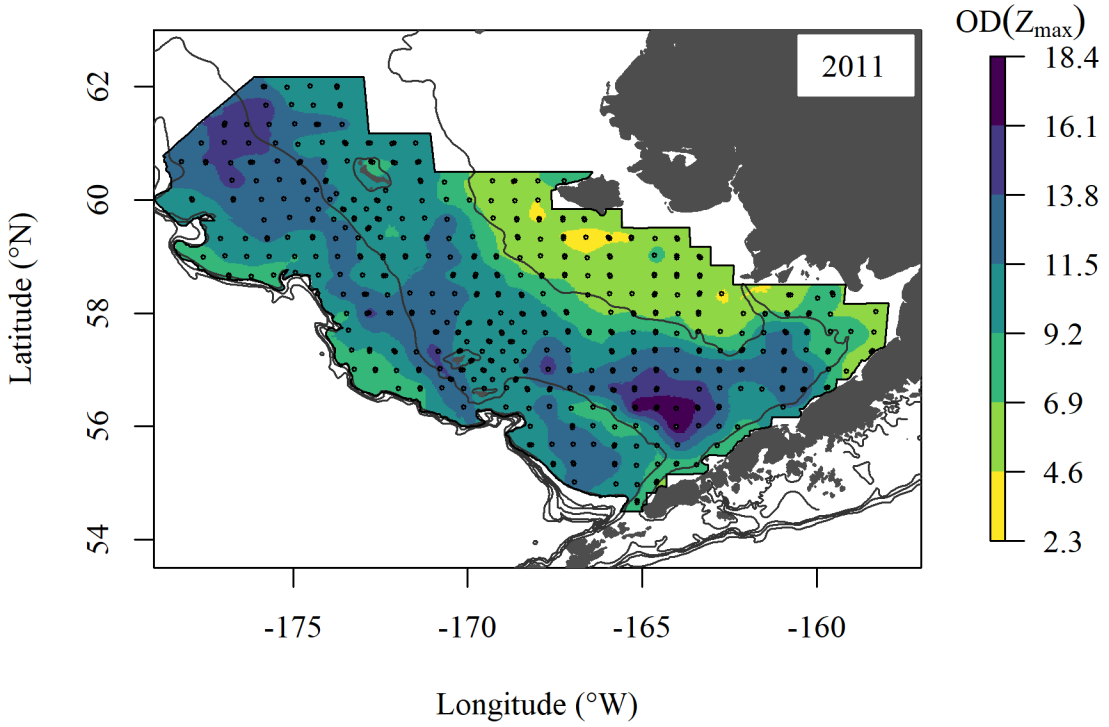

Appendix Figure A-1. -- Continued.

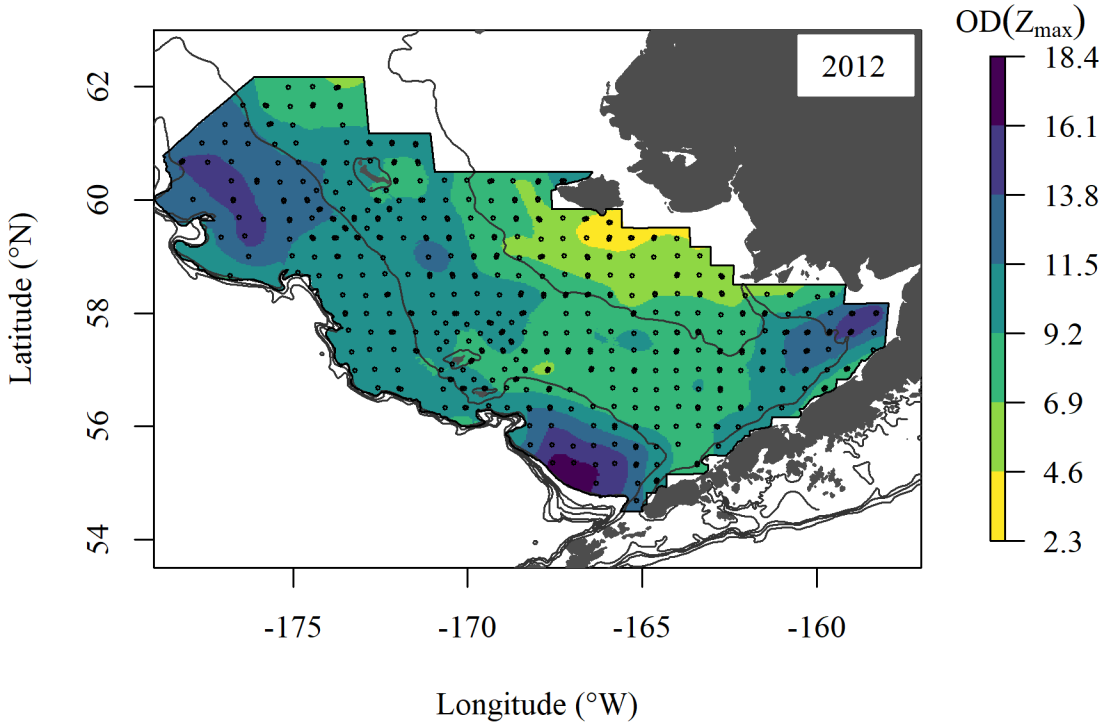

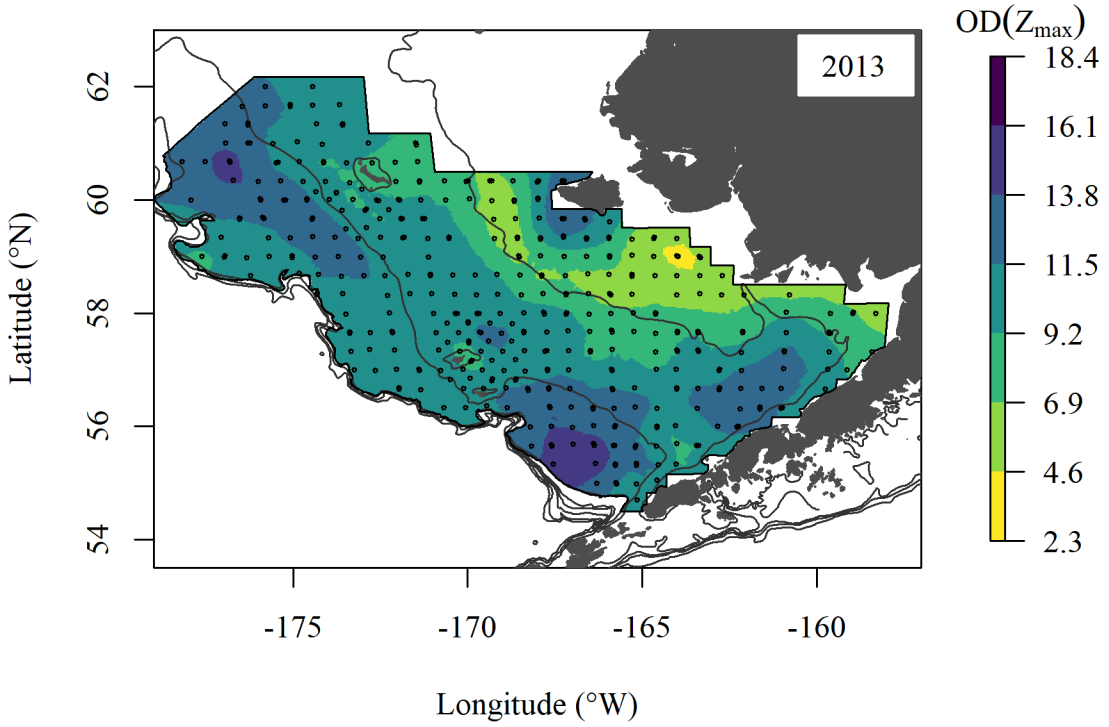

Appendix Figure A-1. -- Continued.

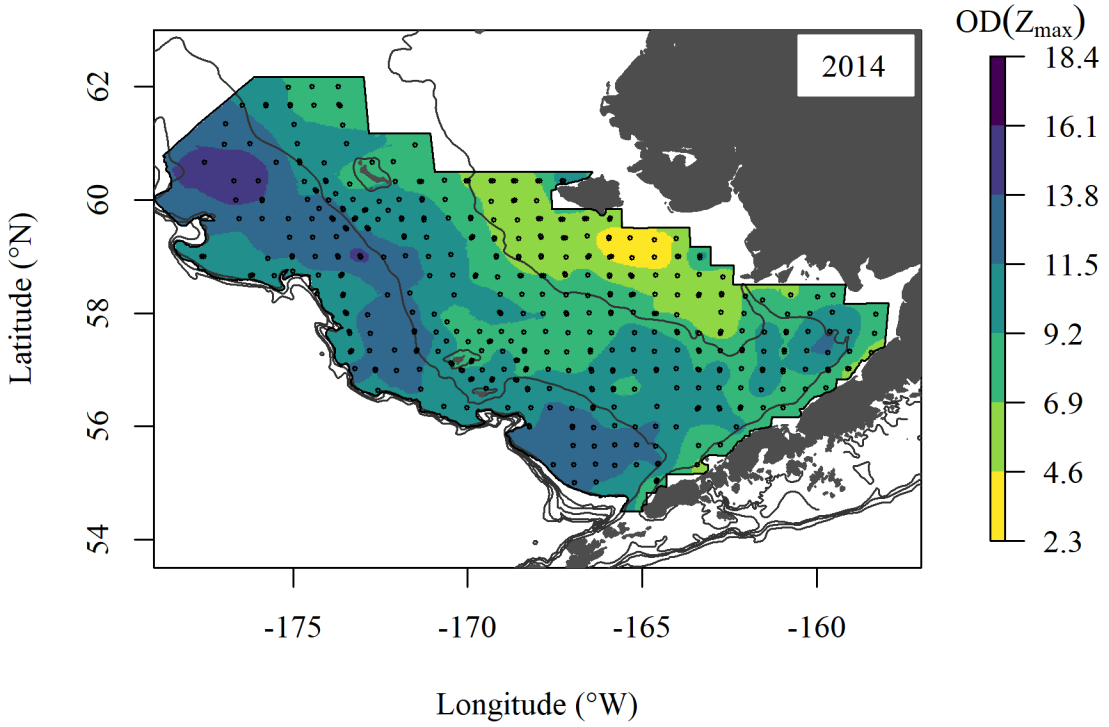

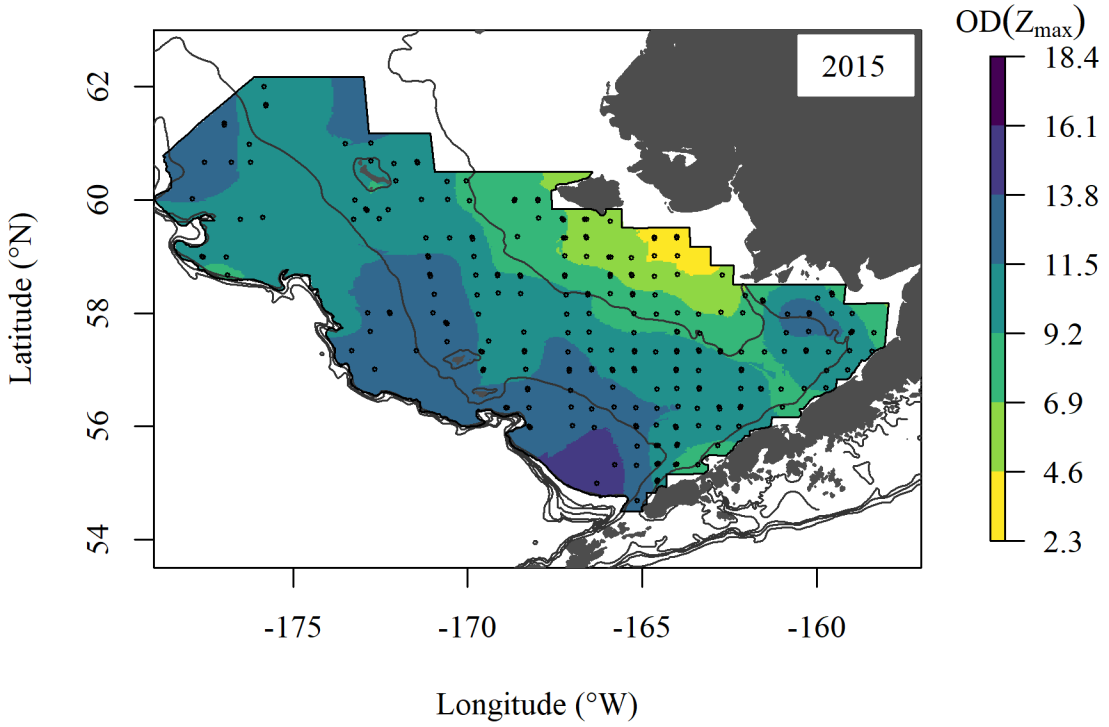

Appendix Figure A-1. -- Continued.

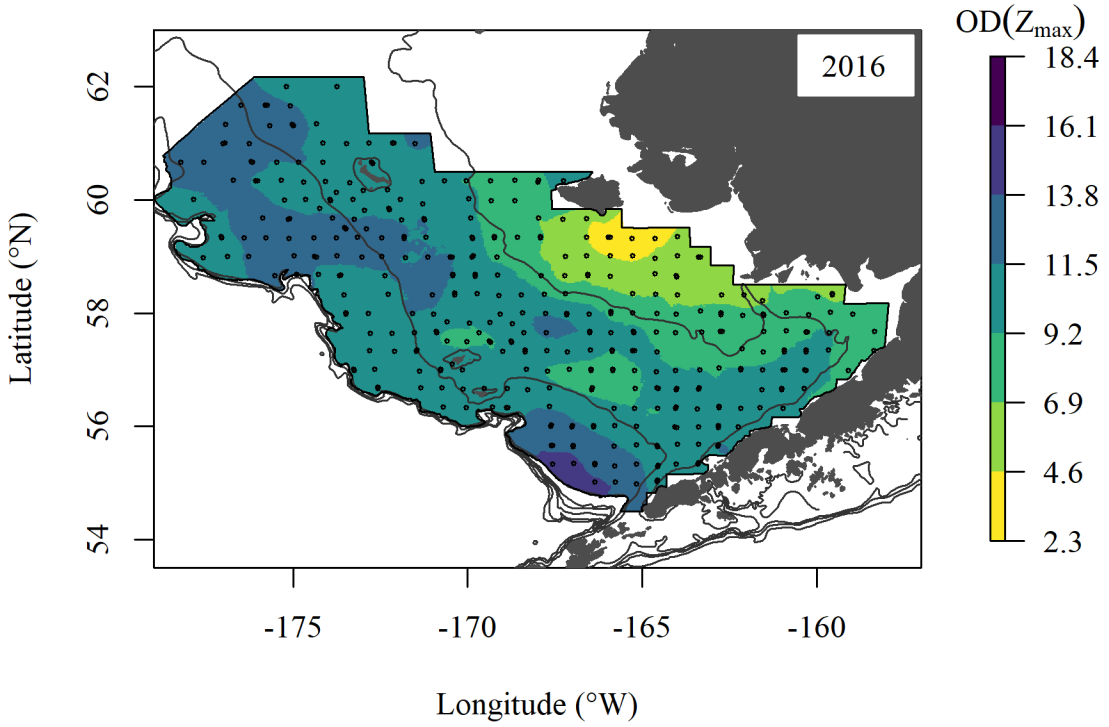

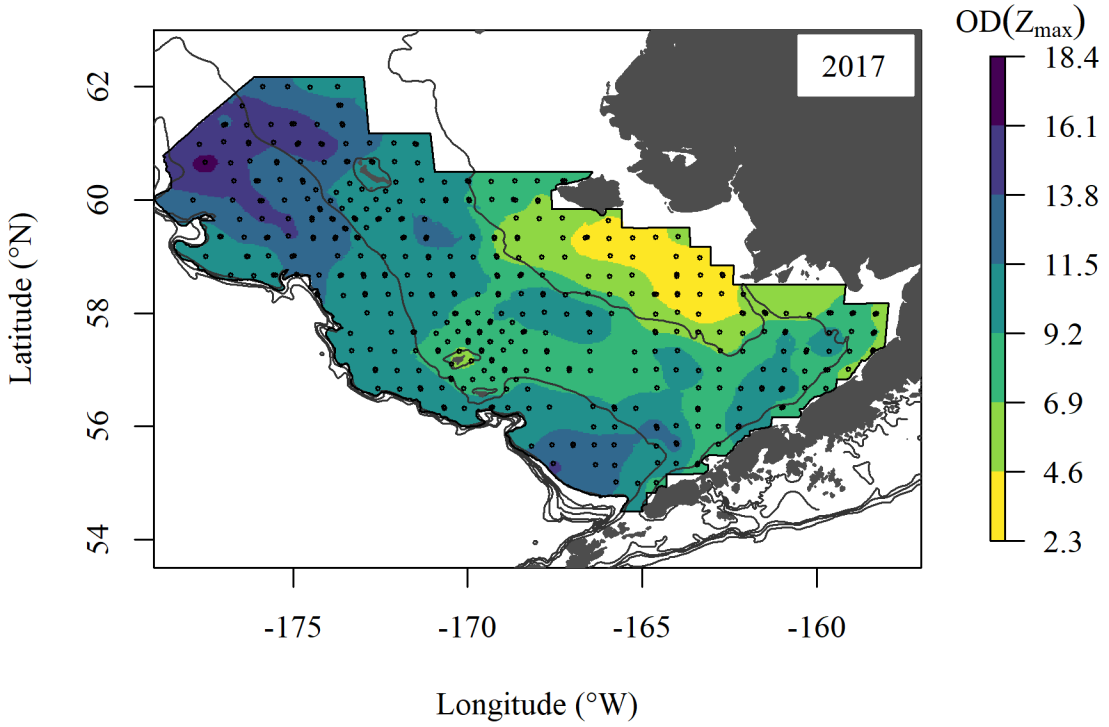

Appendix Figure A-1. -- Continued.

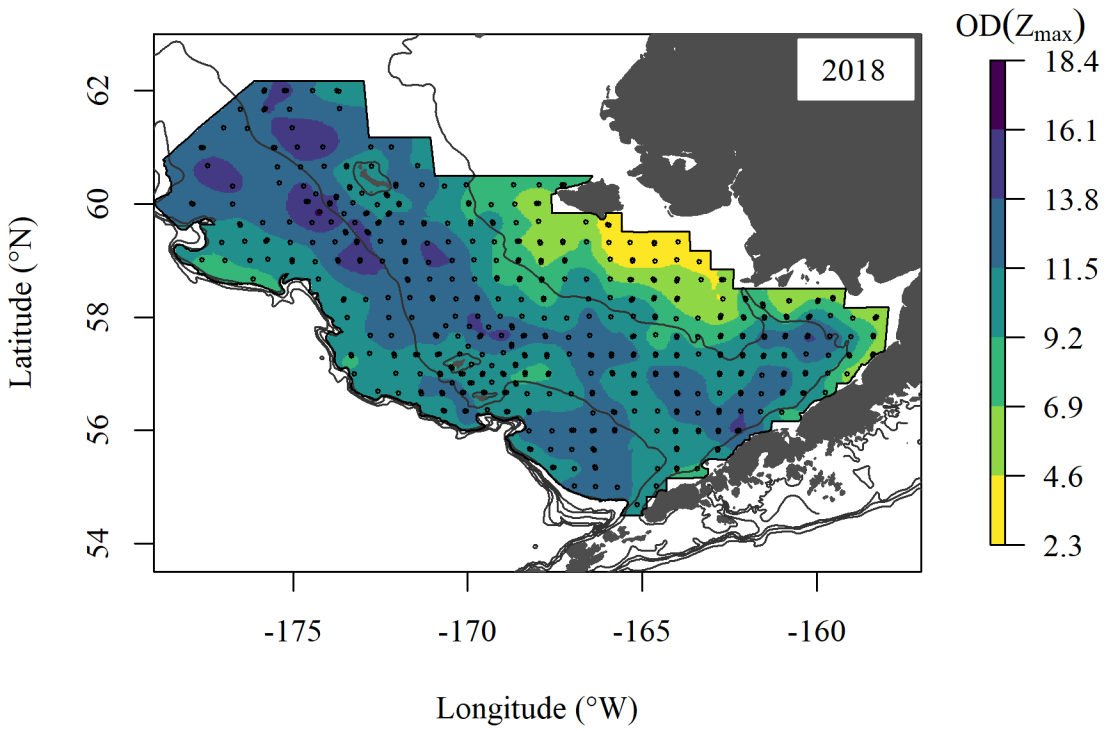

Appendix Figure A-1. -- Continued.

APPENDIX B: $K_d(Z)$ BY STATION AND YEAR

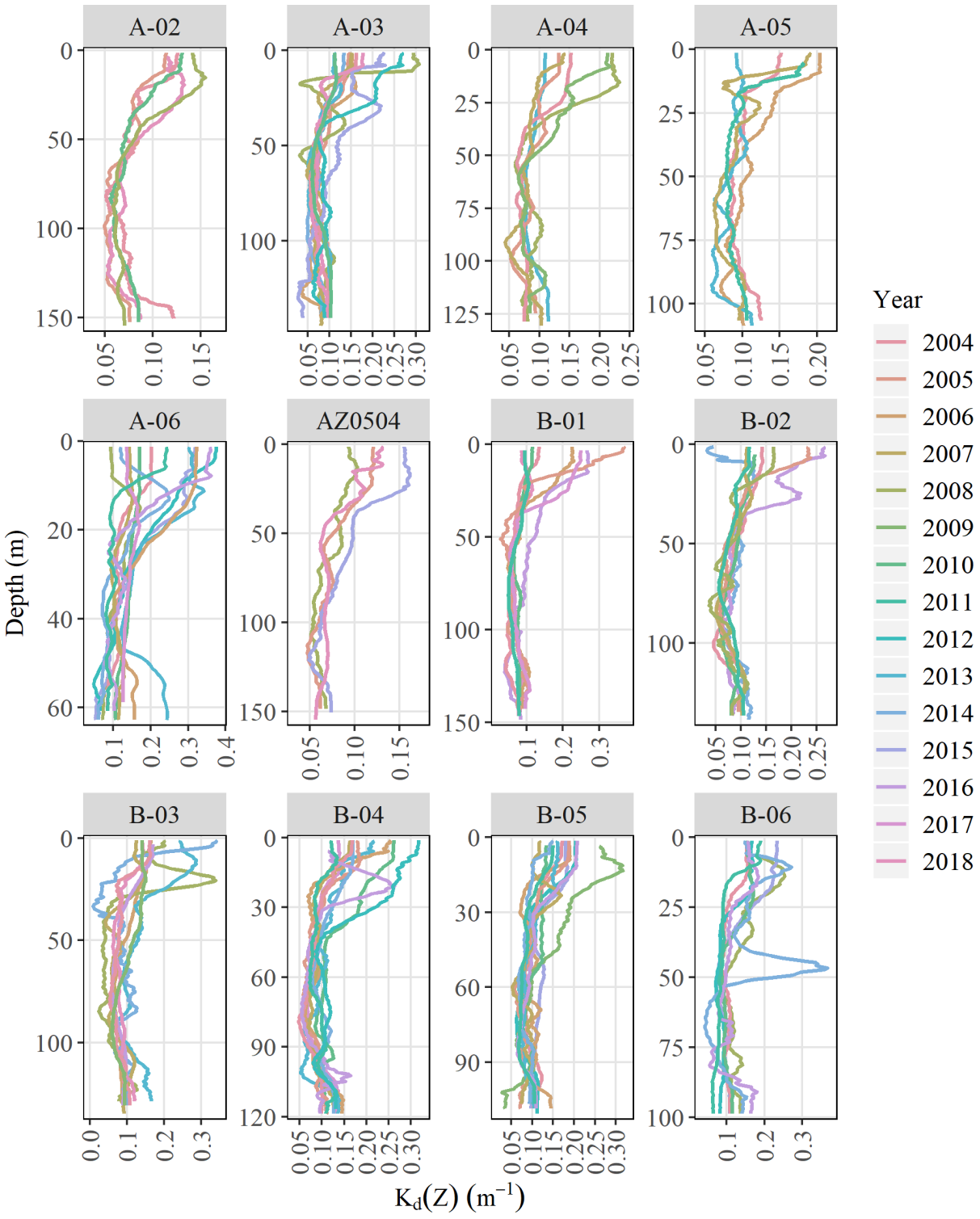

Appendix Figure B-1. -- Vertical attenuation coefficient of downwelling irradiance, $K_d(Z)$, from downcasts, by station (panel titles) and year.

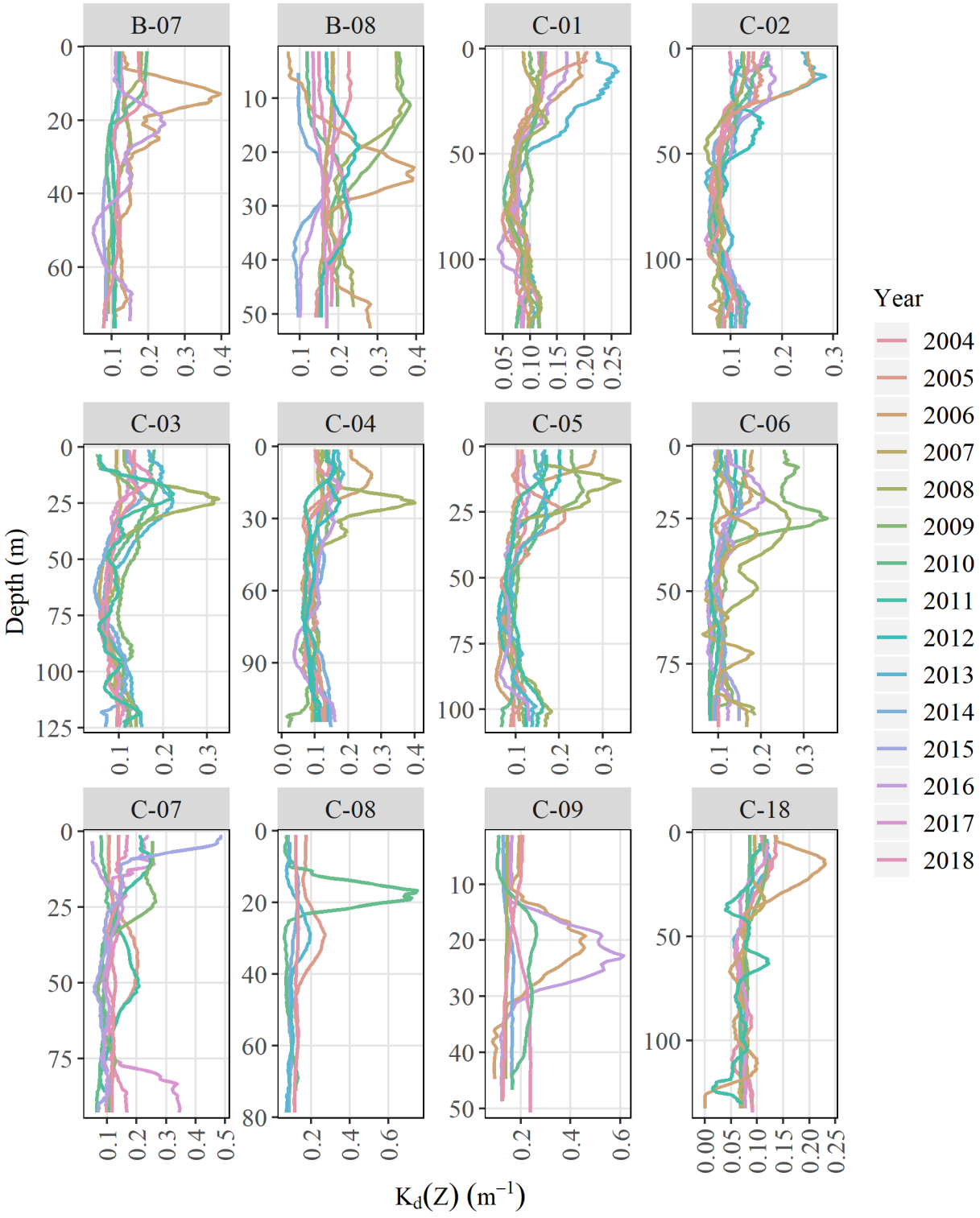

Appendix Figure B-1. -- Continued.

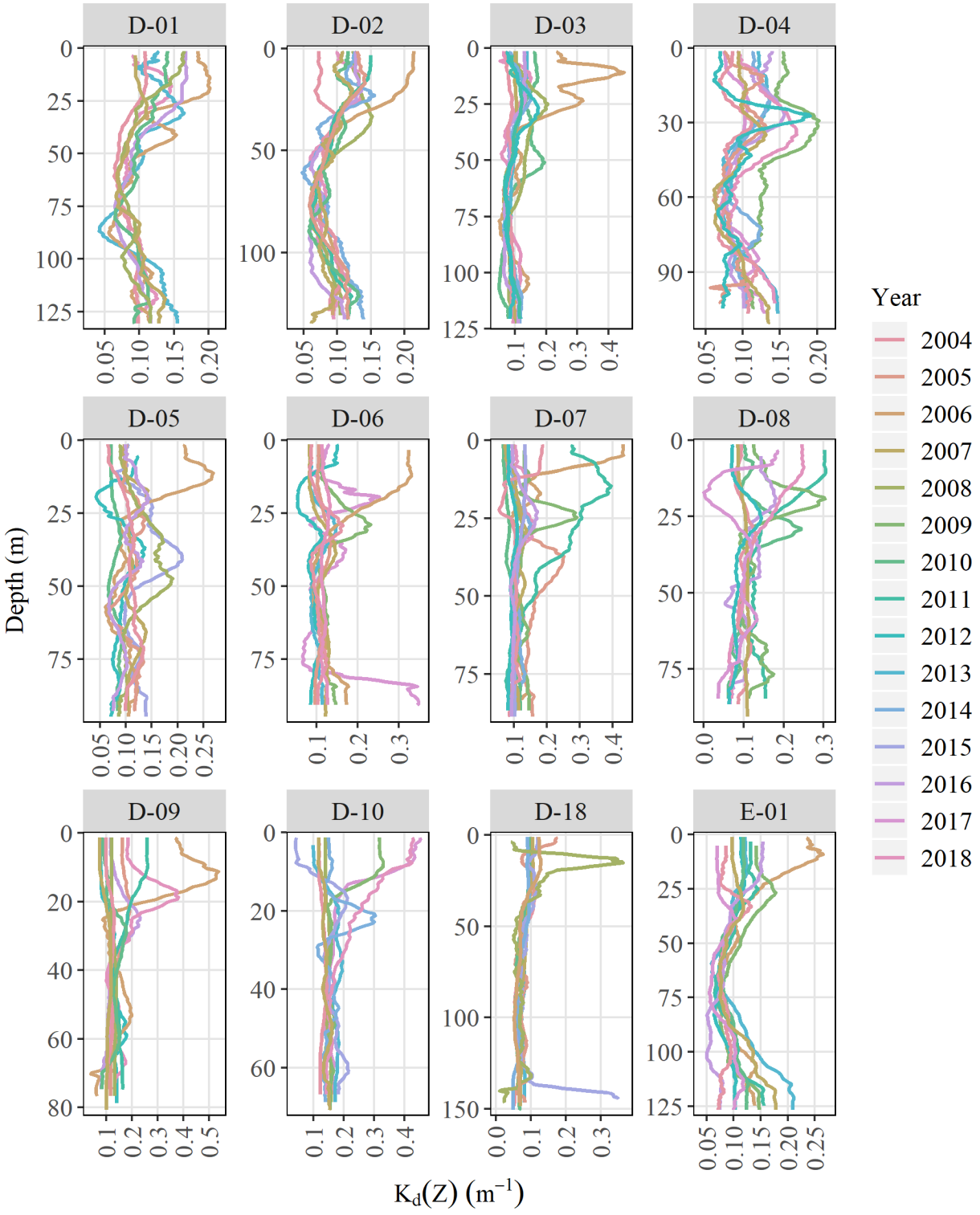

Appendix Figure B-1. -- Continued.

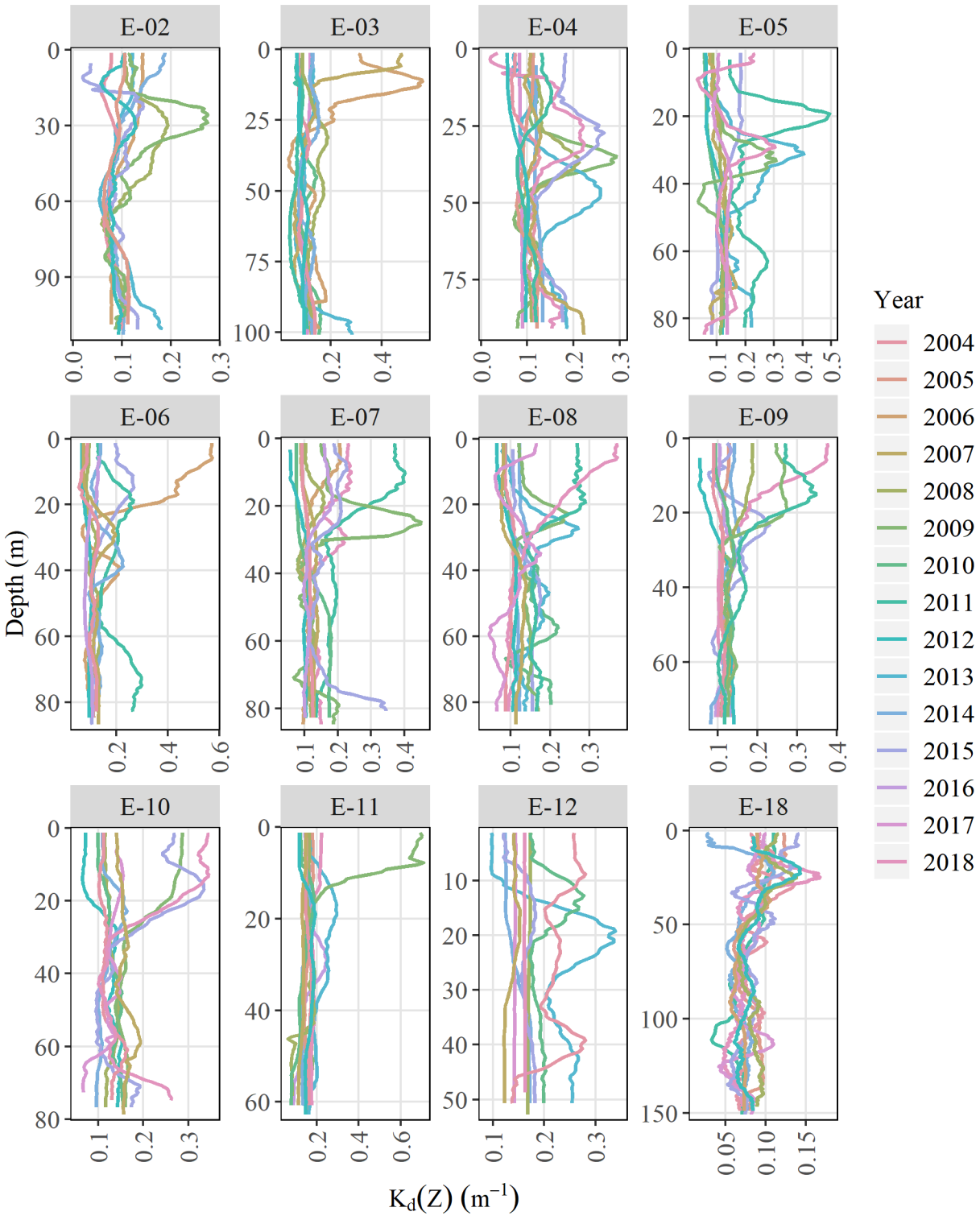

Appendix Figure B-1. -- Continued.

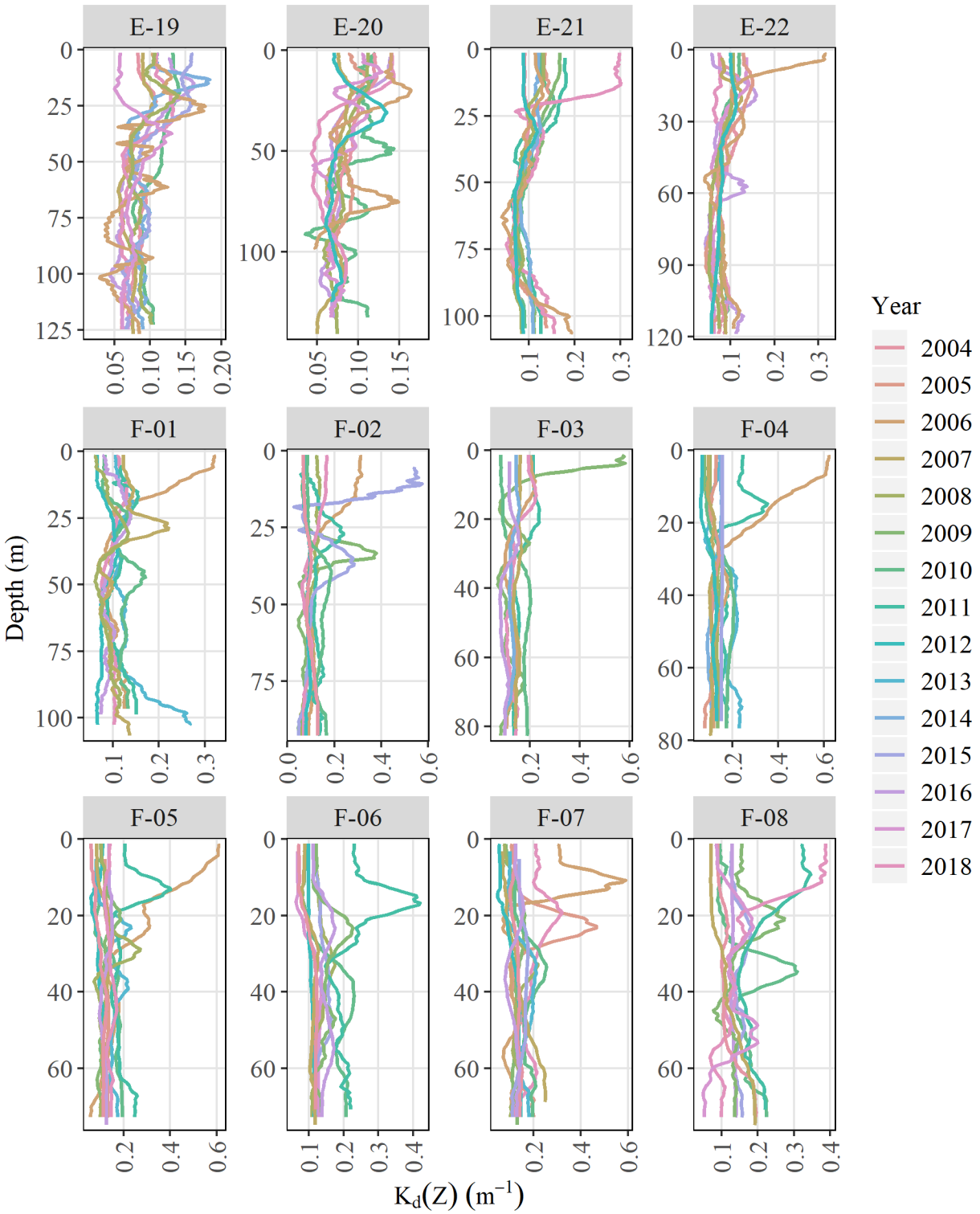

Appendix Figure B-1. -- Continued.

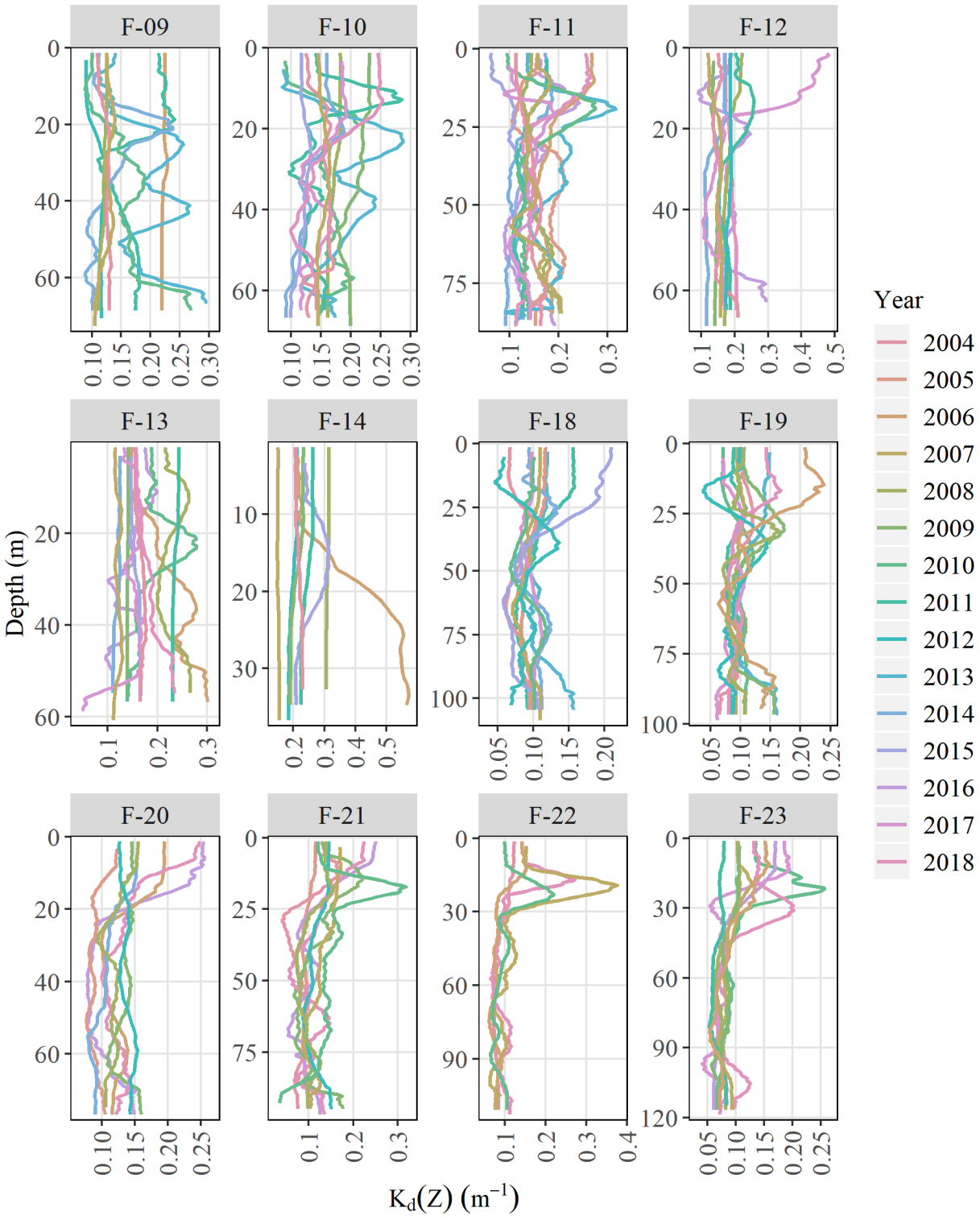

Appendix Figure B-1. -- Continued.

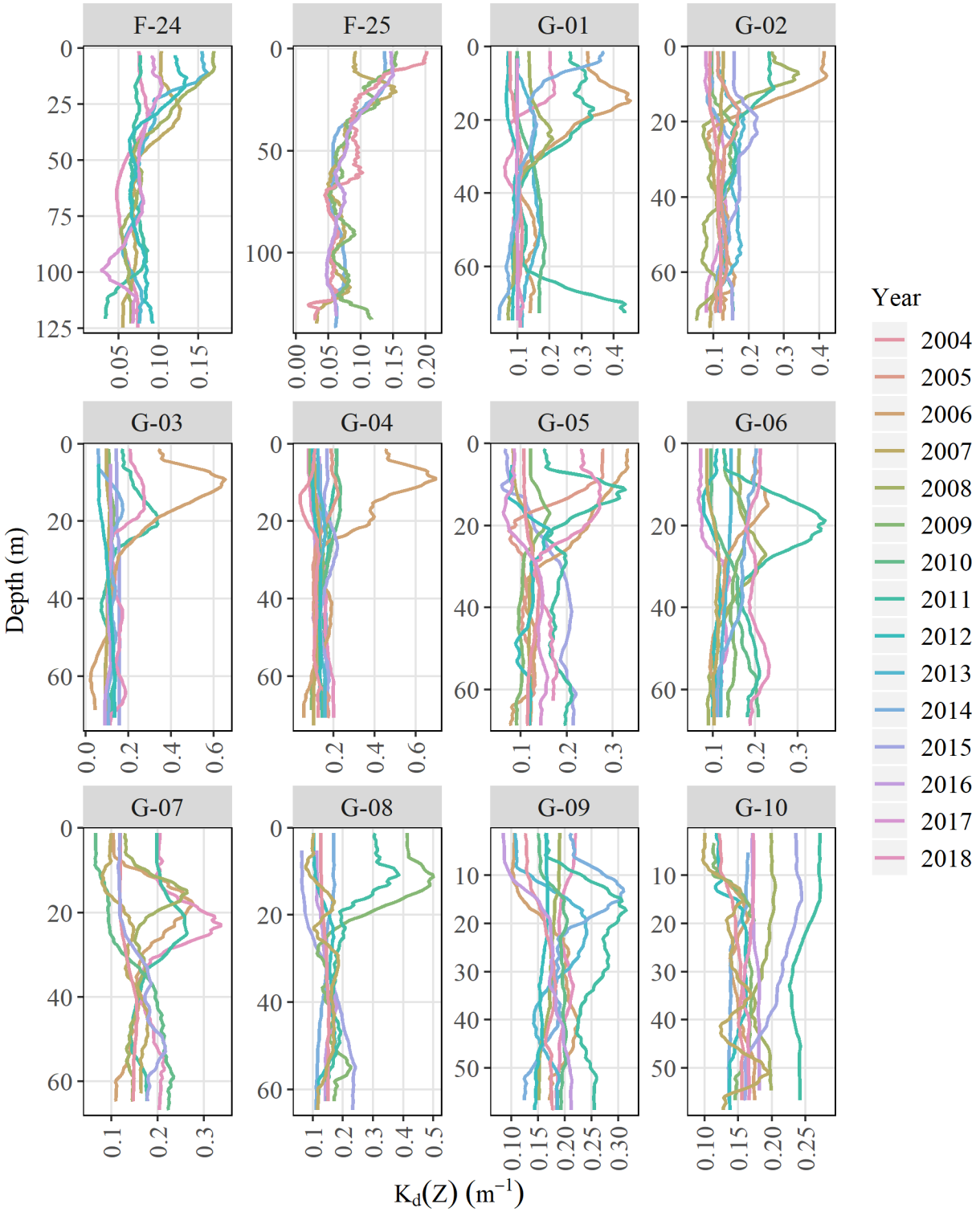

Appendix Figure B-1. -- Continued.

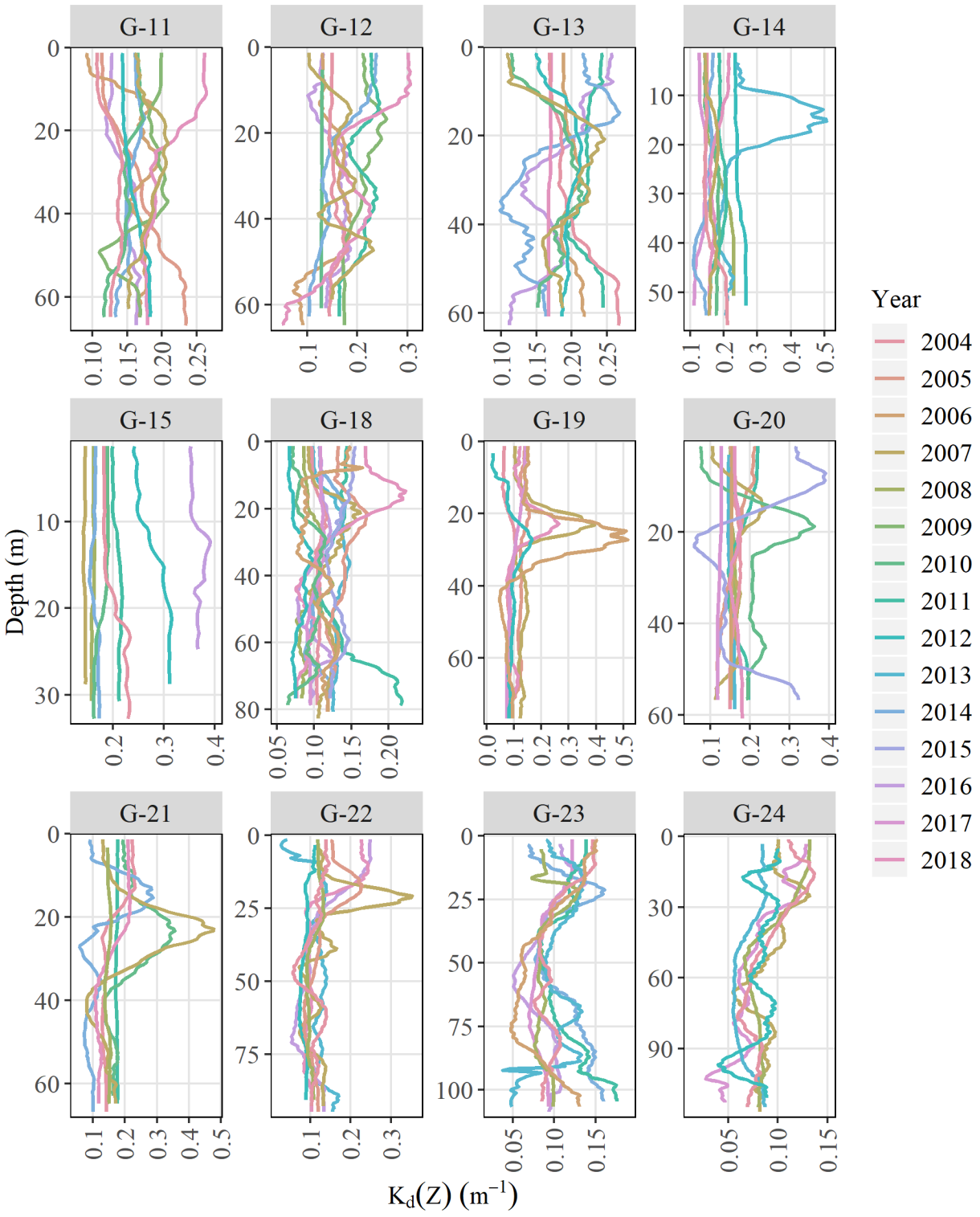

Appendix Figure B-1. -- Continued.

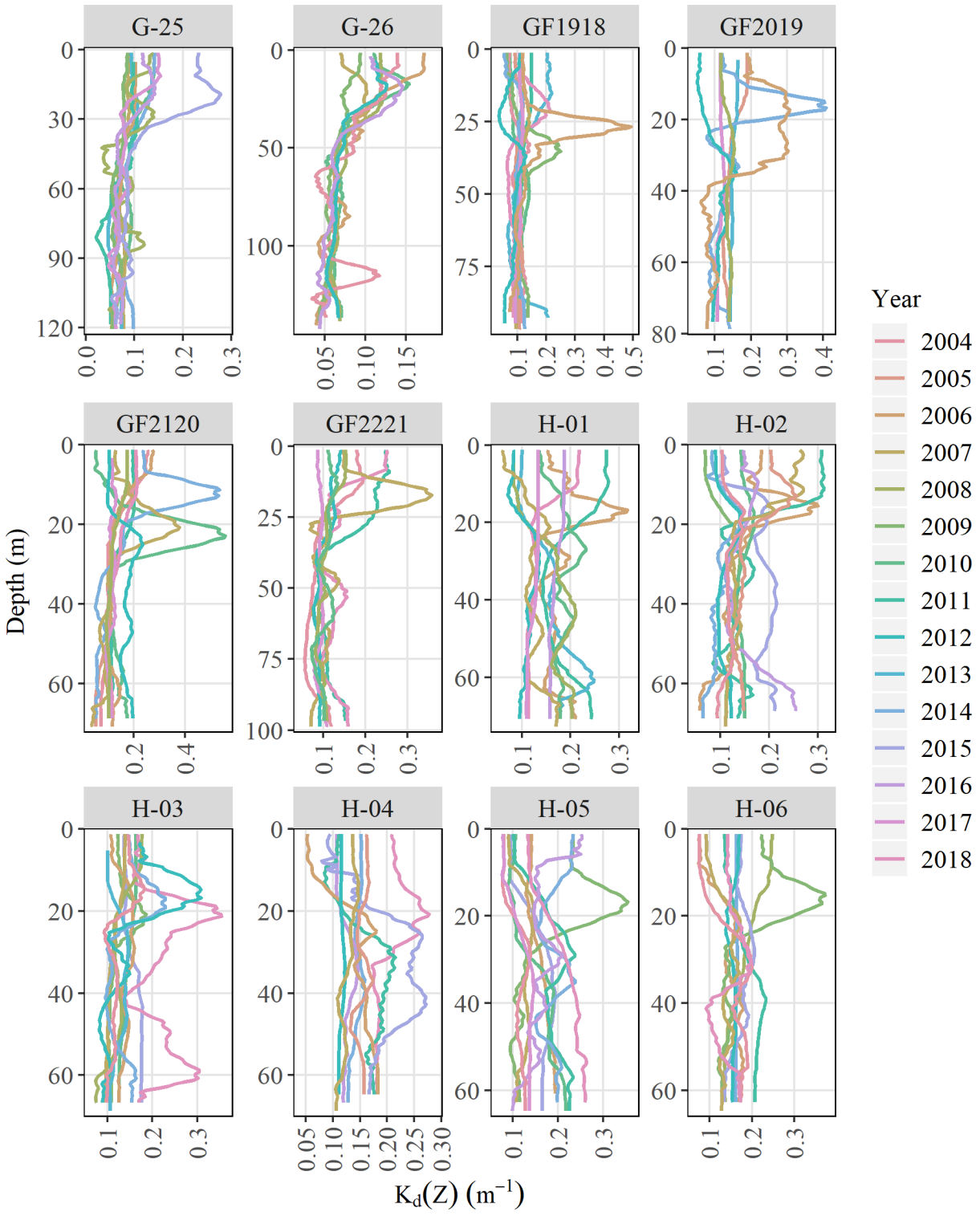

Appendix Figure B-1. -- Continued.

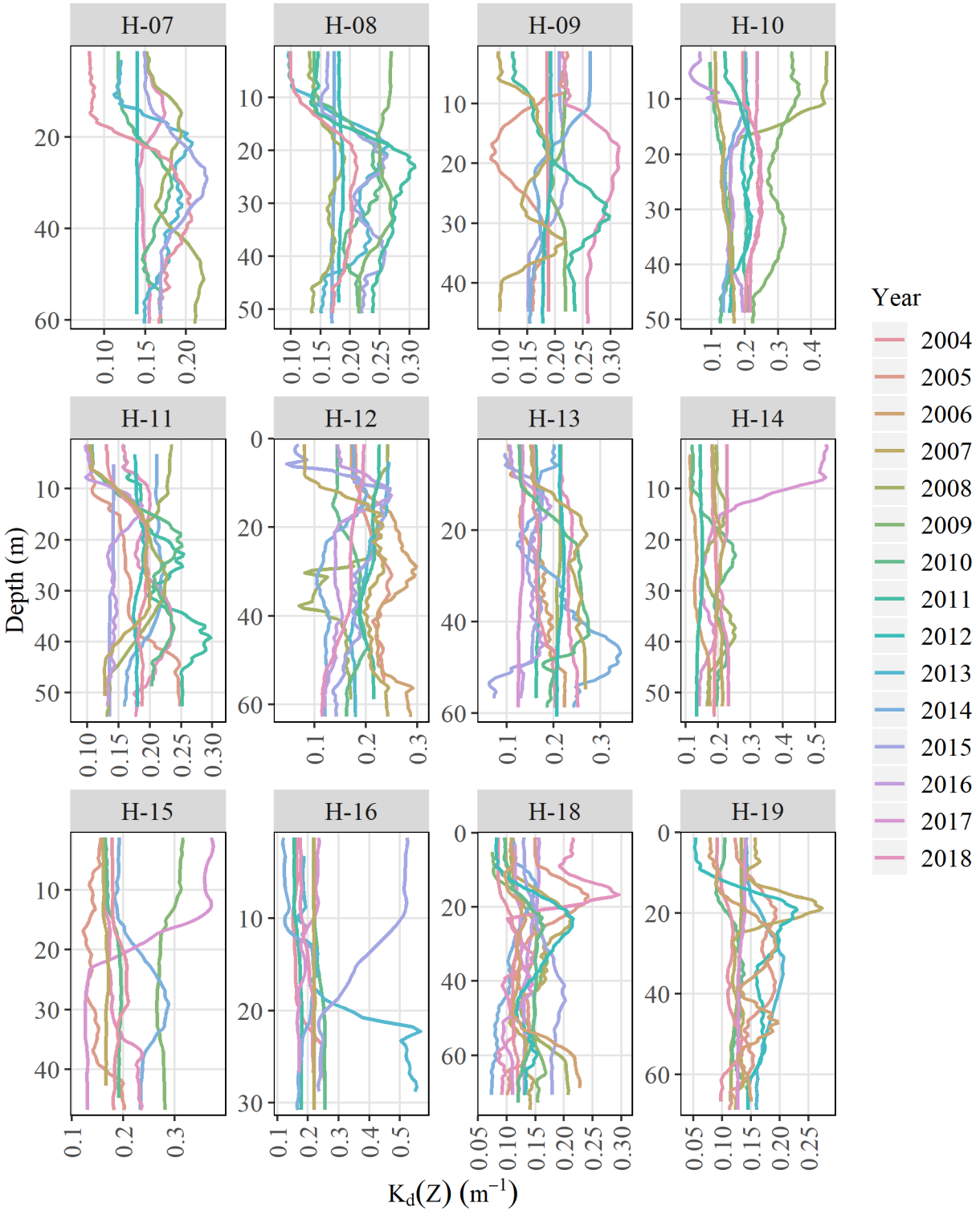

Appendix Figure B-1. -- Continued.

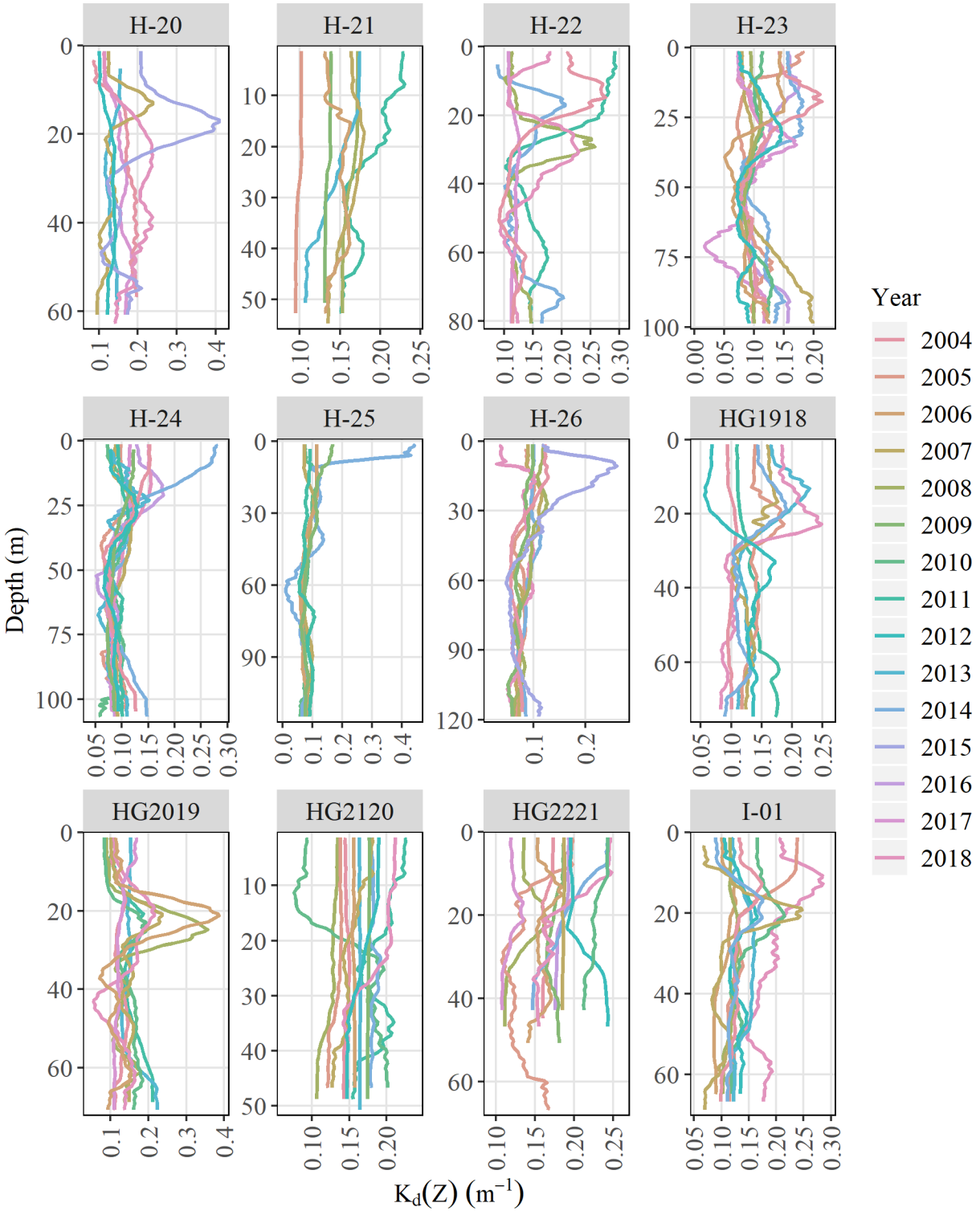

Appendix Figure B-1. -- Continued.

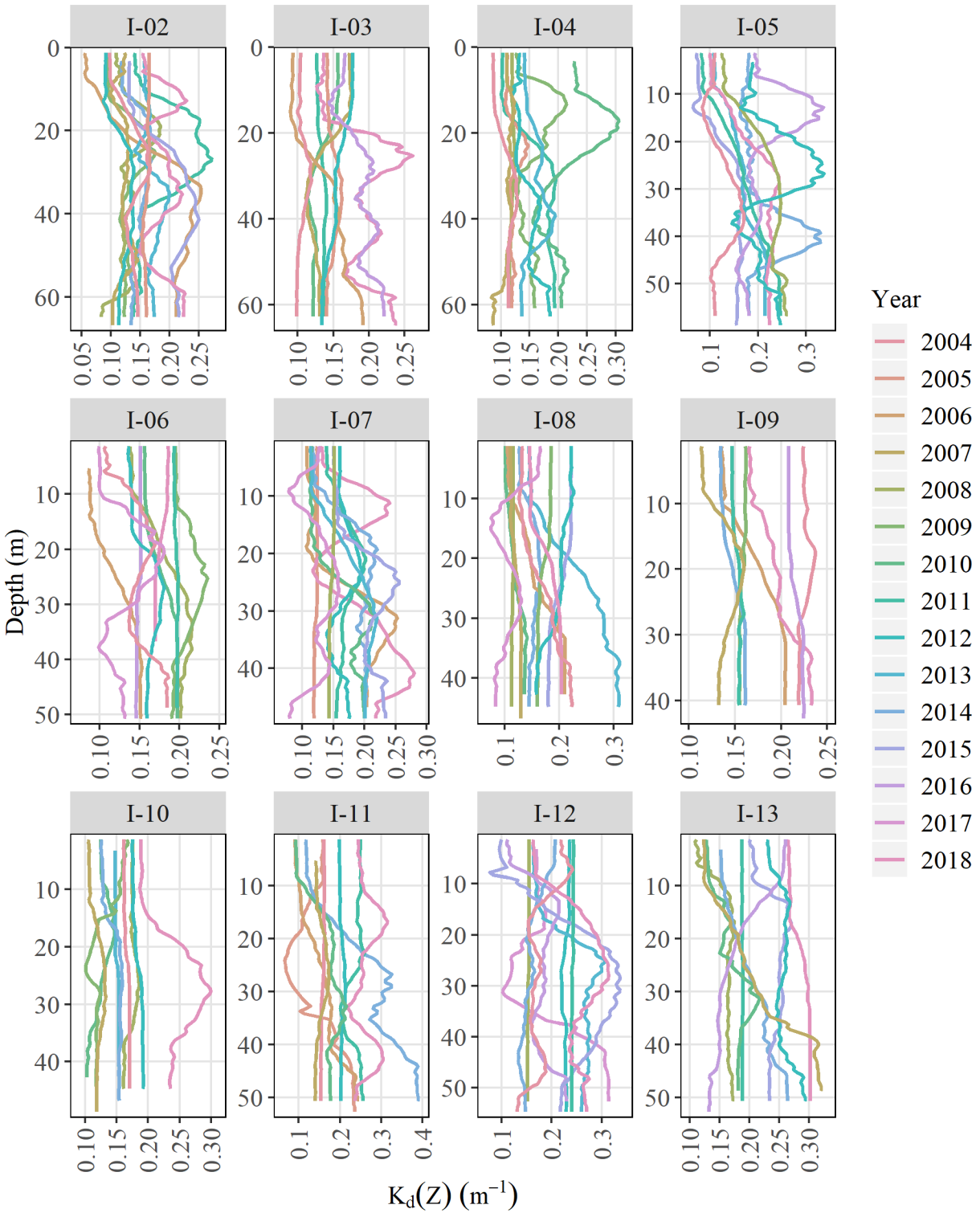

Appendix Figure B-1. -- Continued.

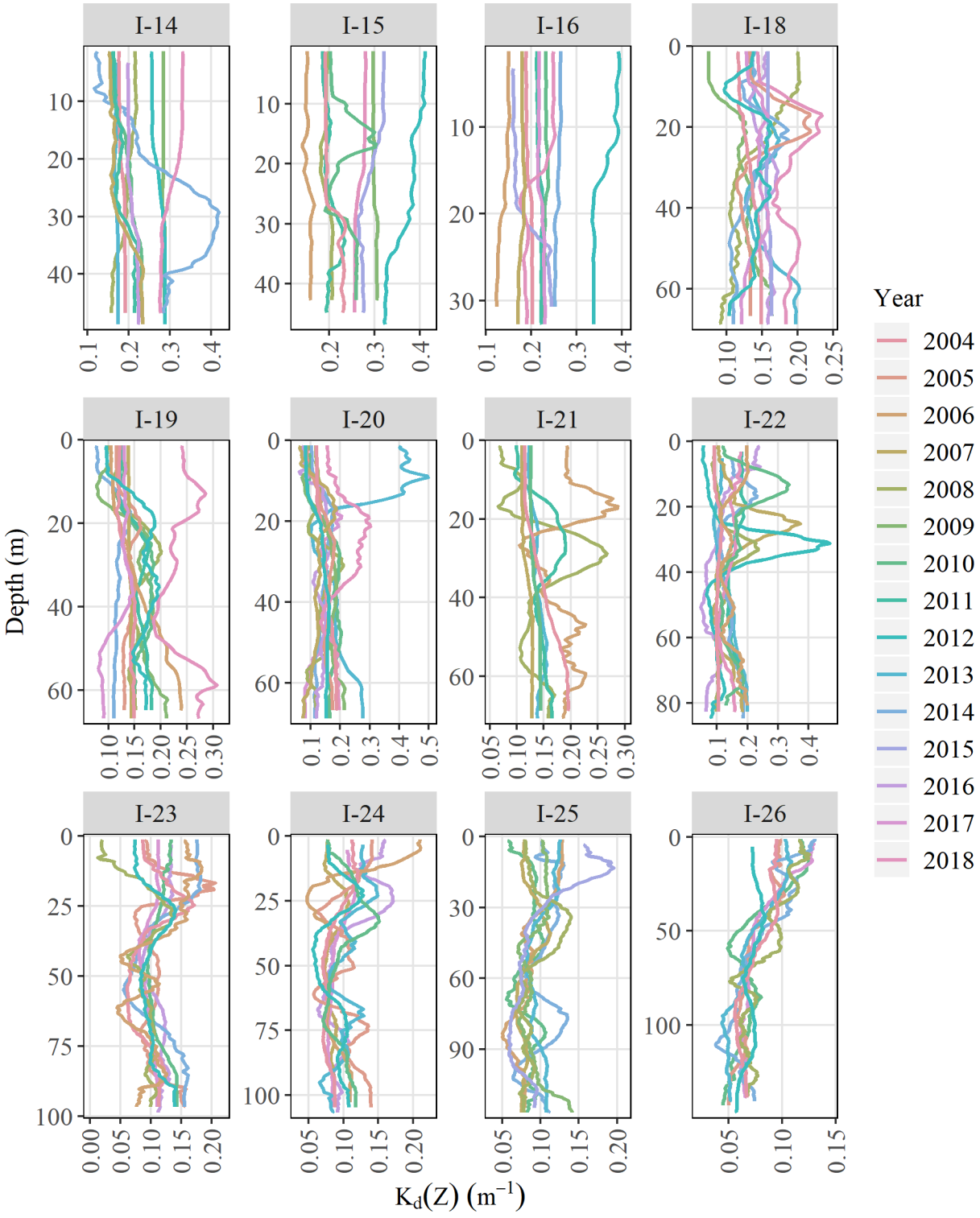

Appendix Figure B-1. -- Continued.

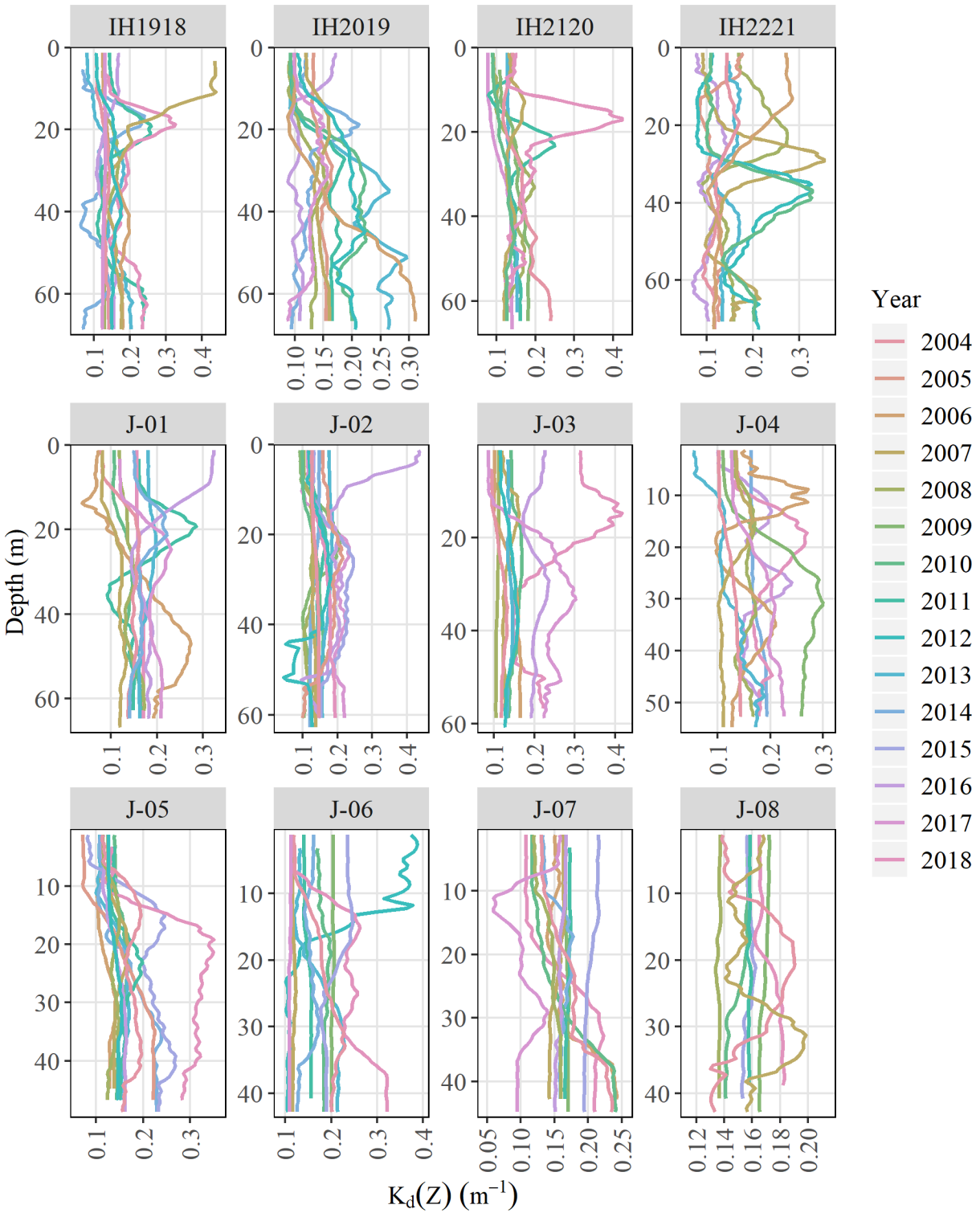

Appendix Figure B-1. -- Continued.

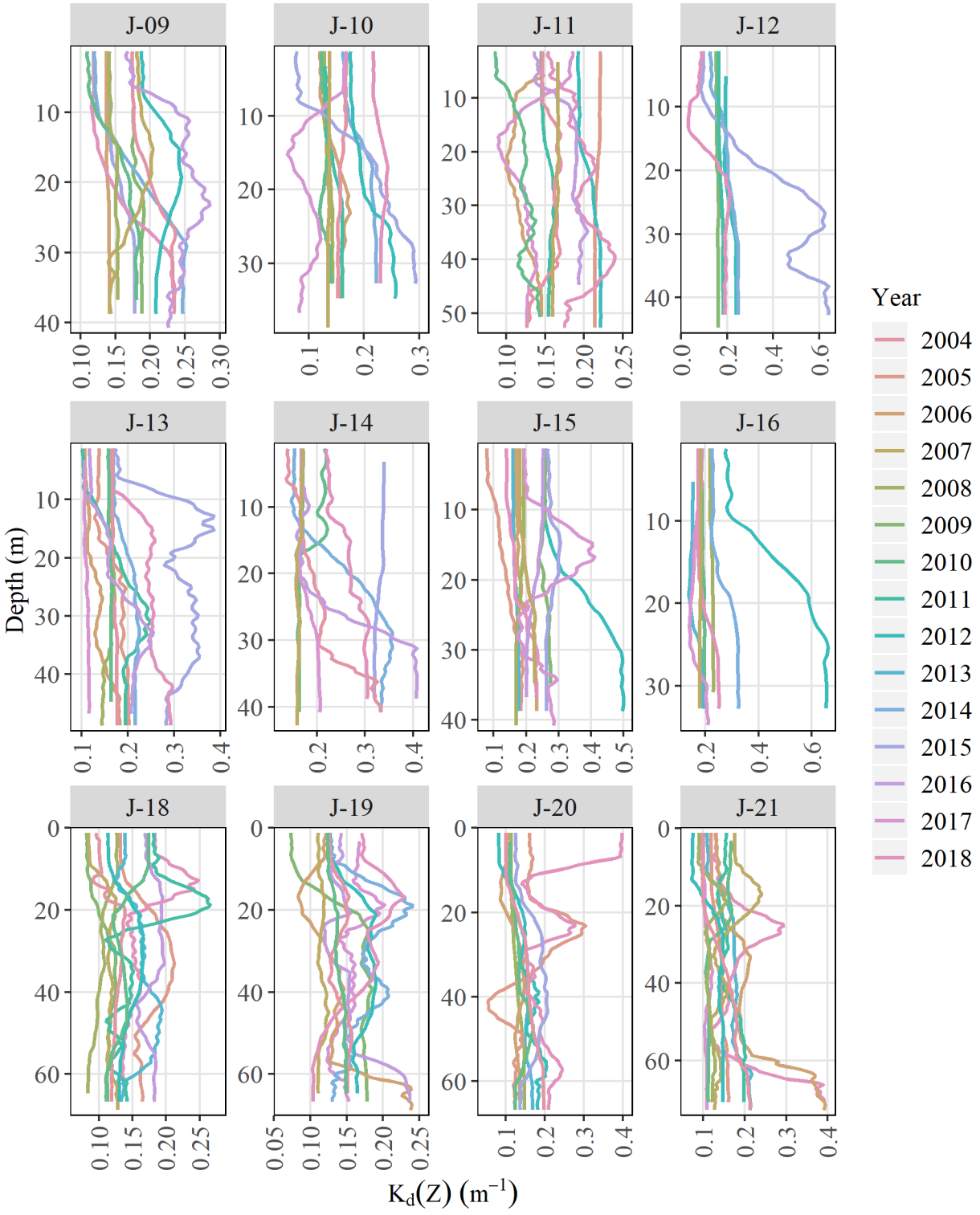

Appendix Figure B-1. -- Continued.

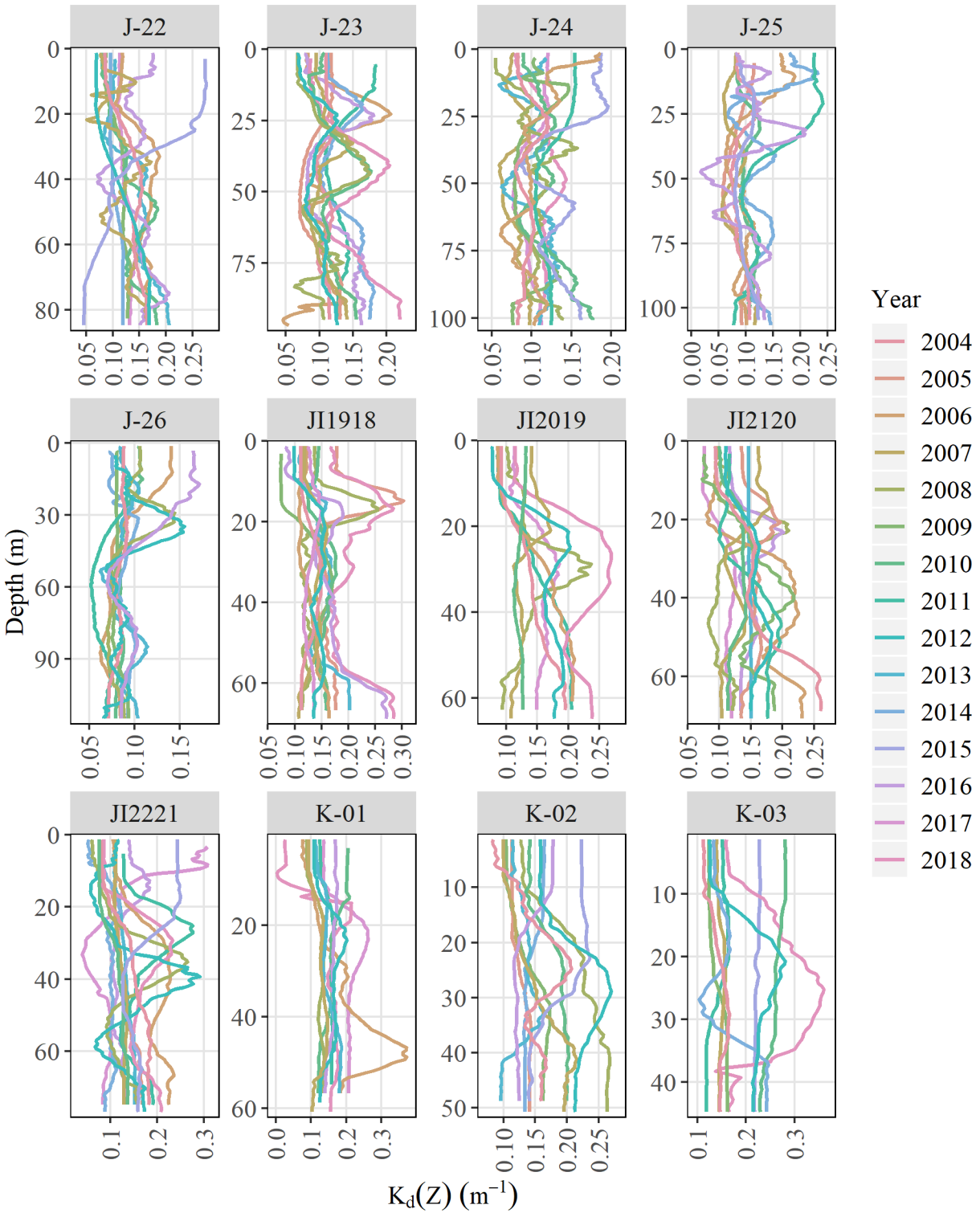

Appendix Figure B-1. -- Continued.

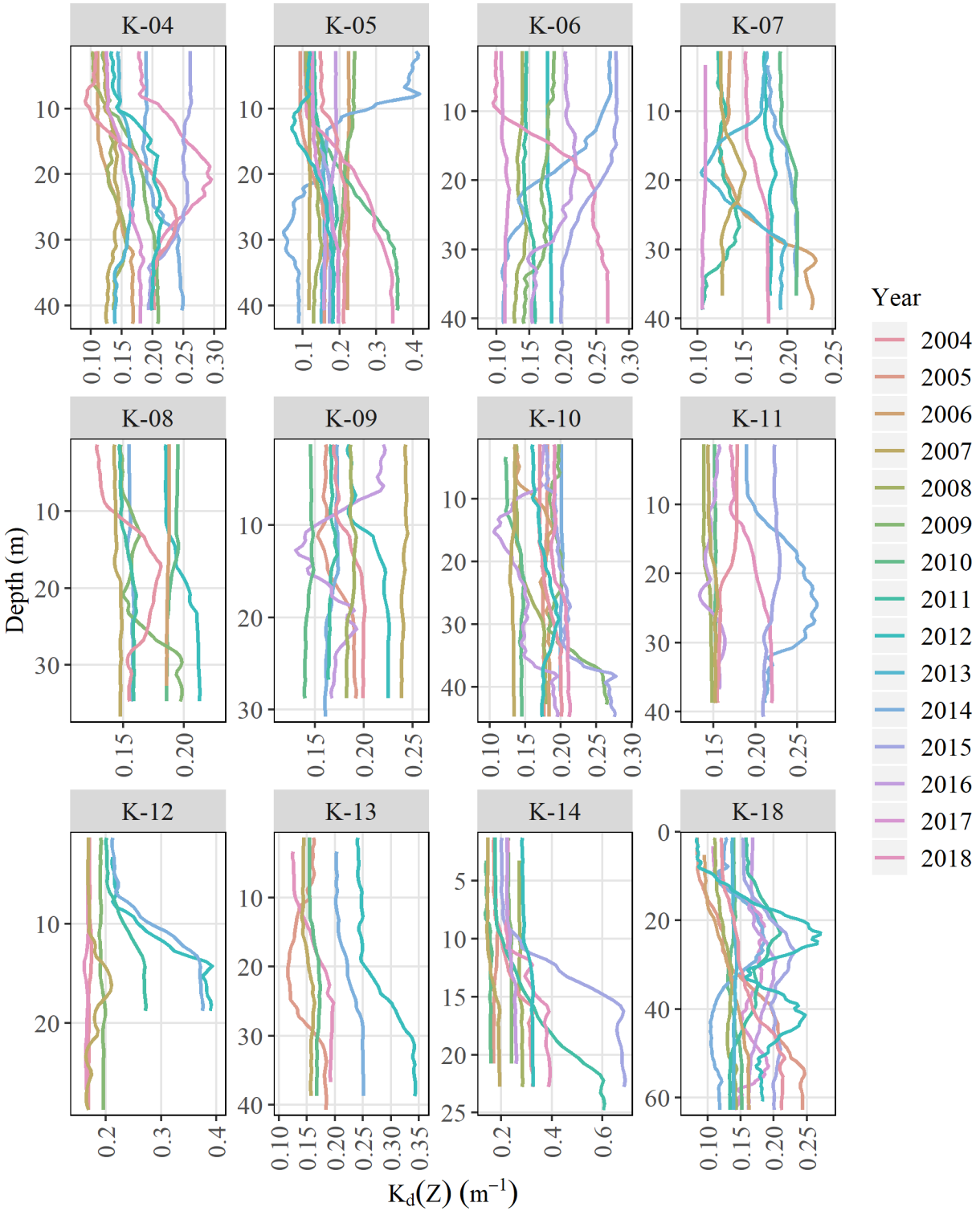

Appendix Figure B-1. -- Continued.

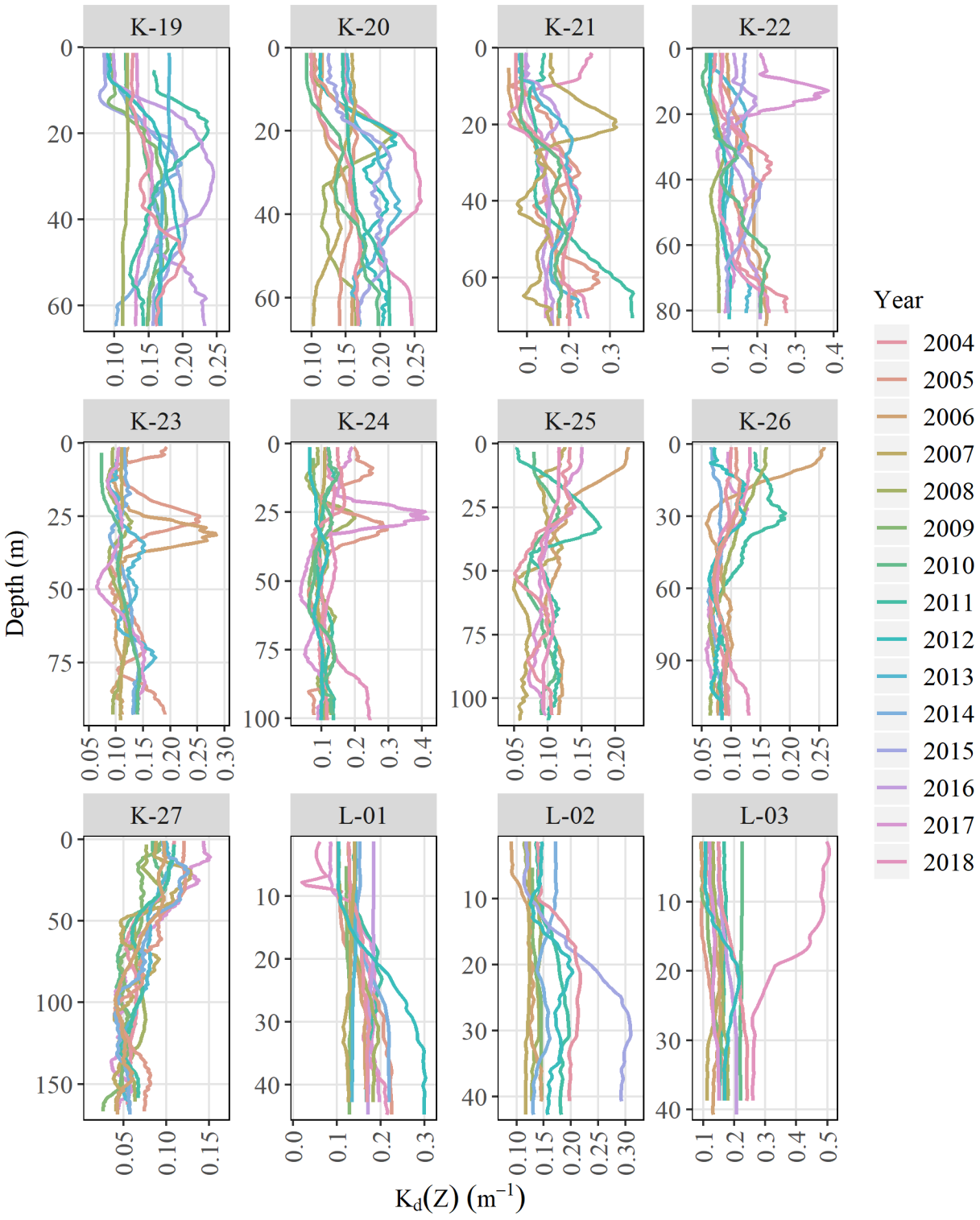

Appendix Figure B-1. -- Continued.

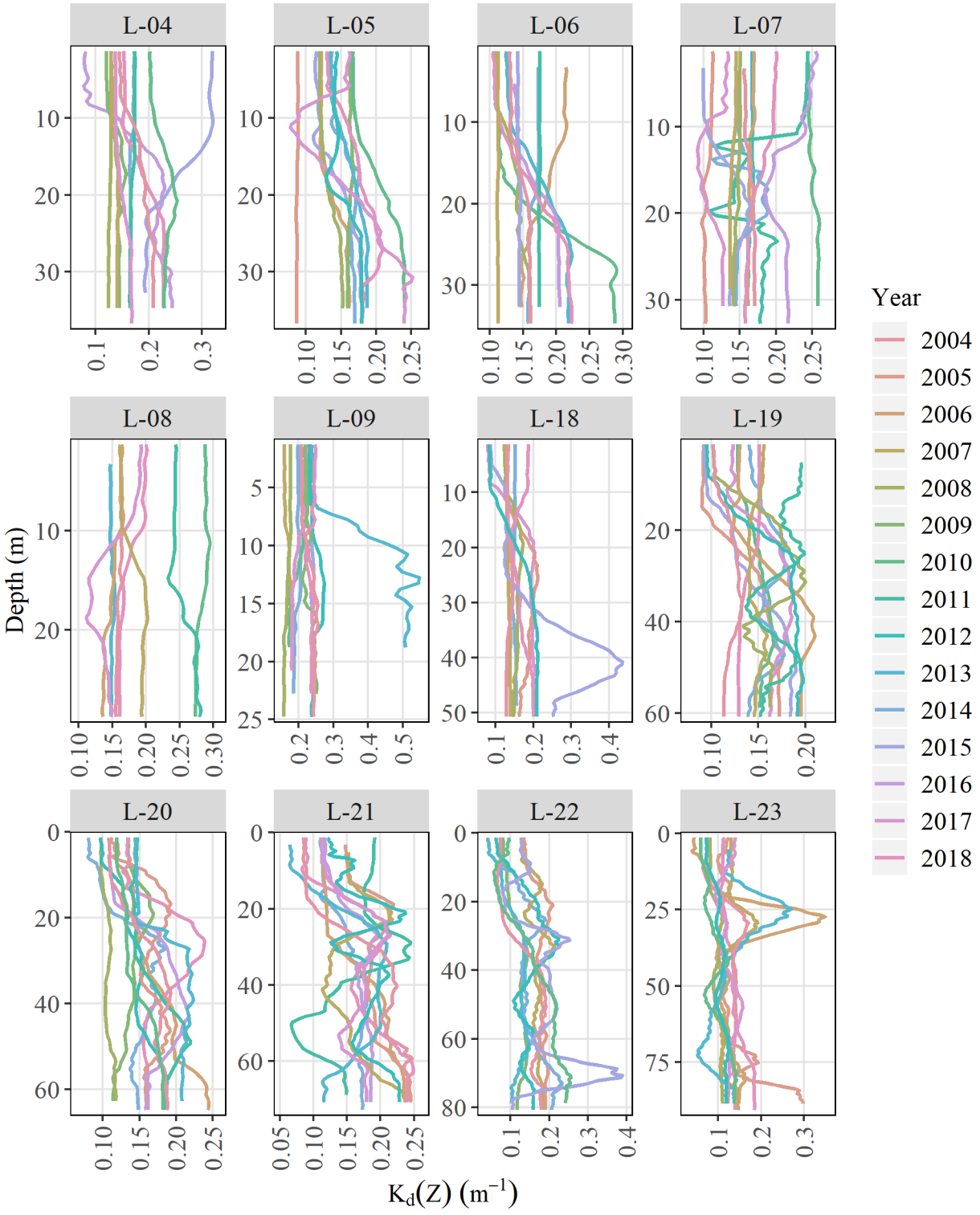

Appendix Figure B-1. -- Continued.

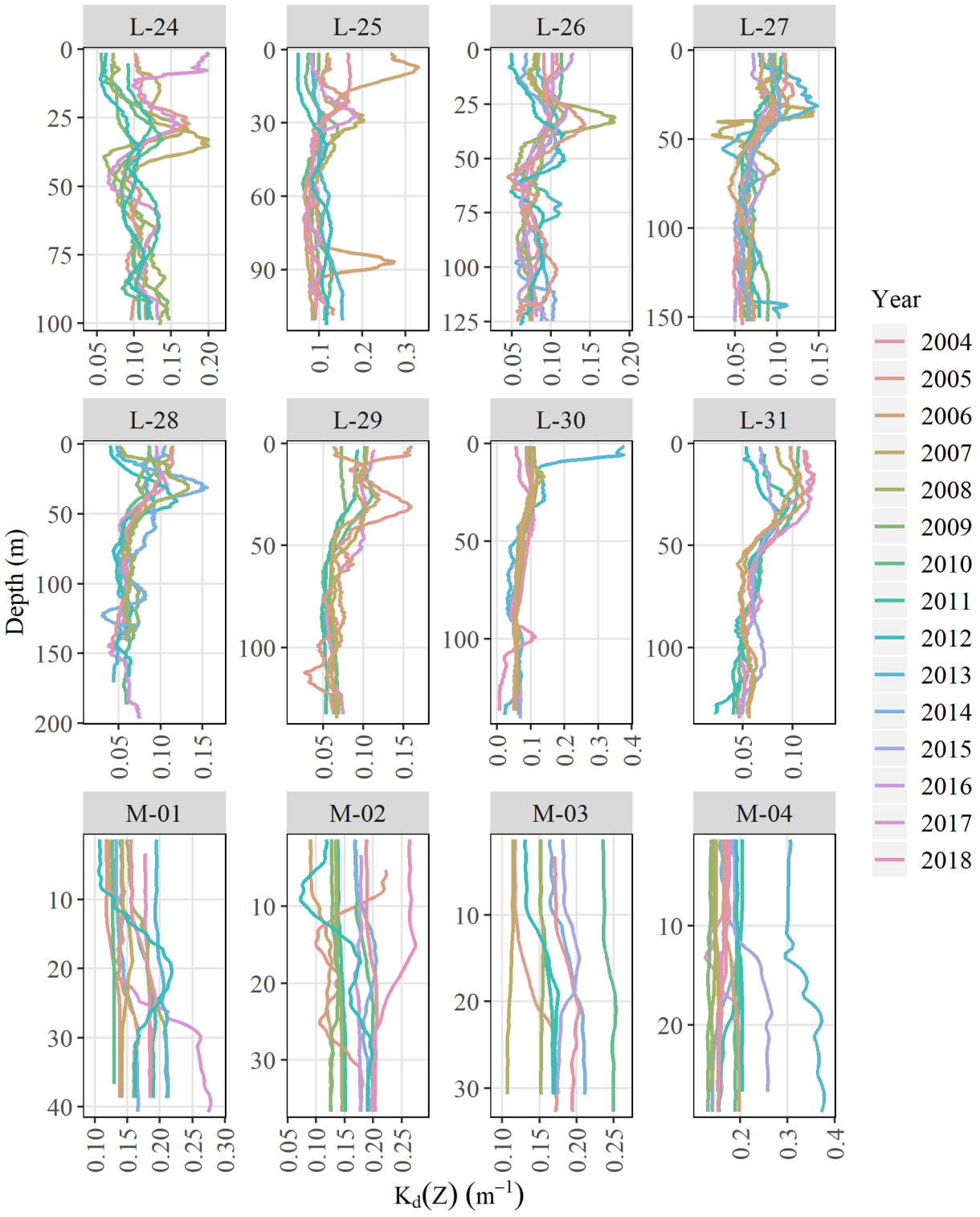

Appendix Figure B-1. -- Continued.

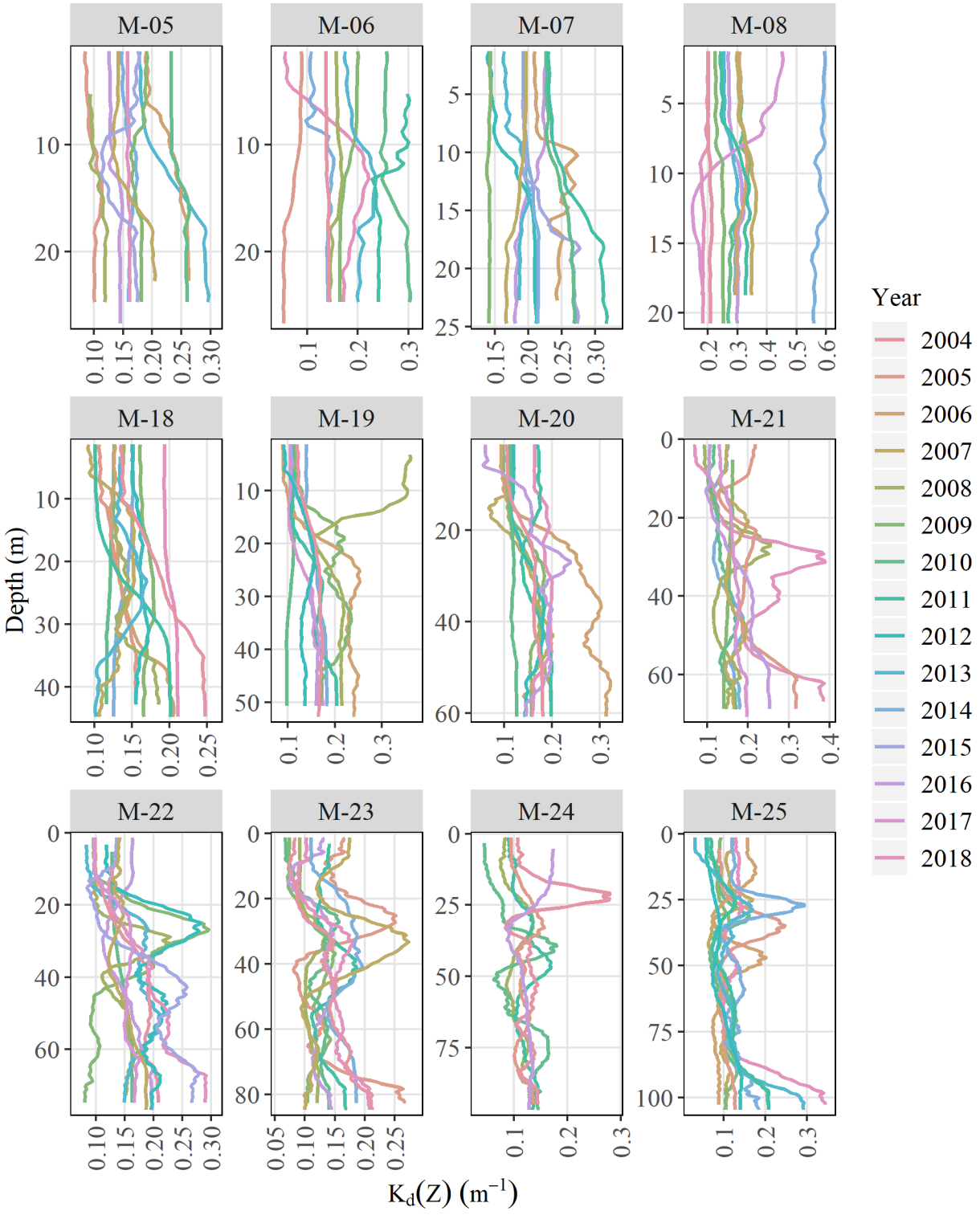

Appendix Figure B-1. -- Continued.

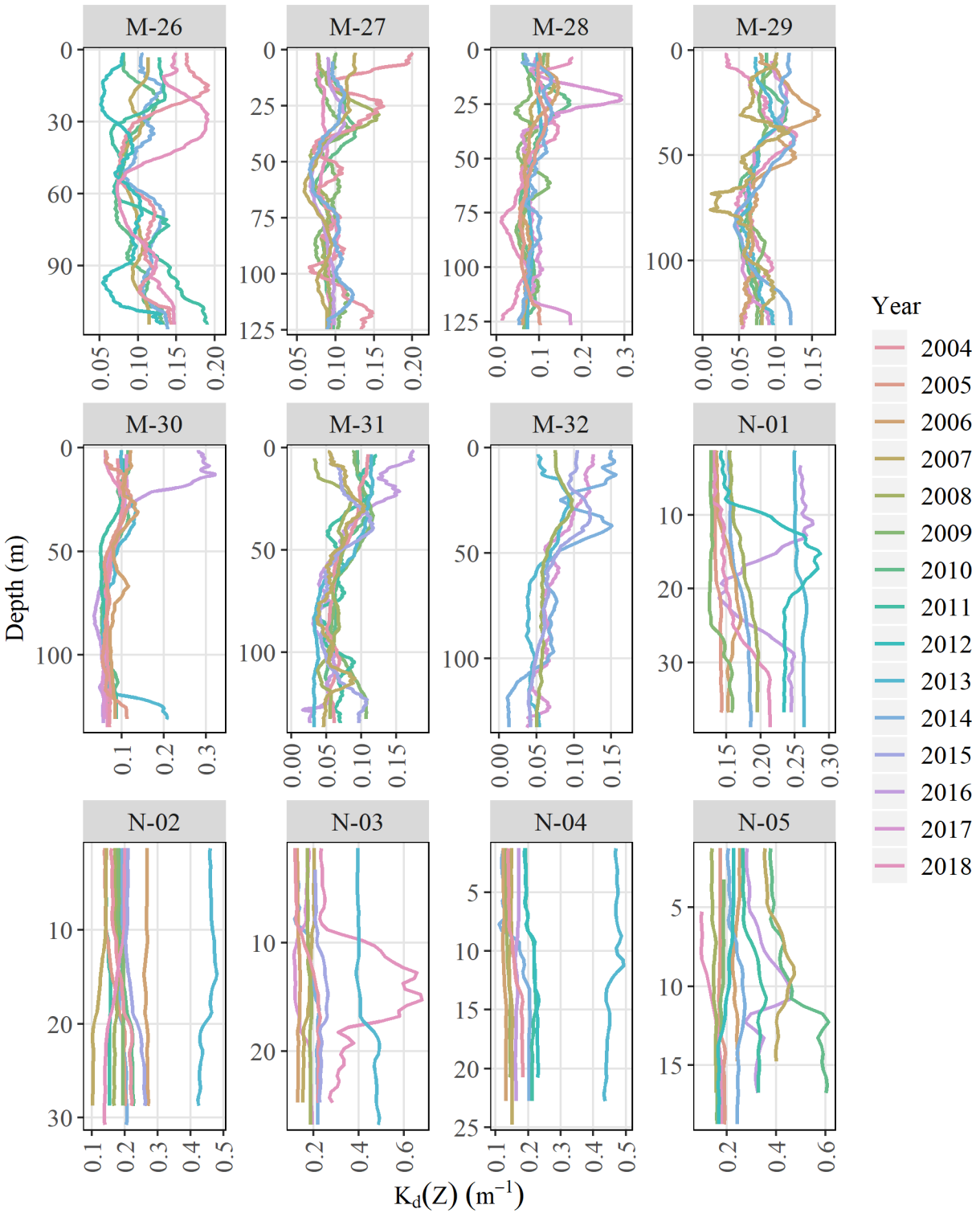

Appendix Figure B-1. -- Continued.

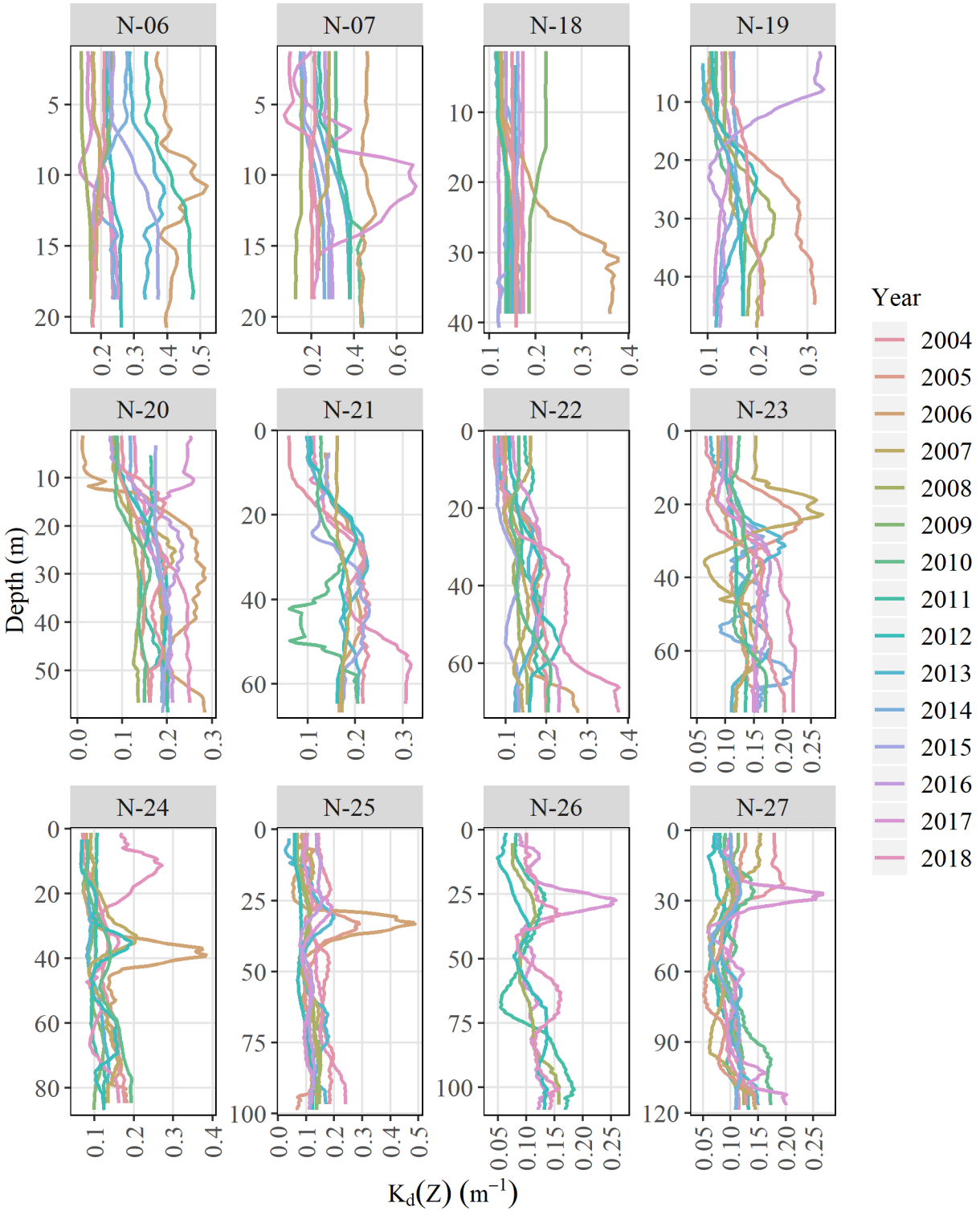

Appendix Figure B-1. -- Continued.

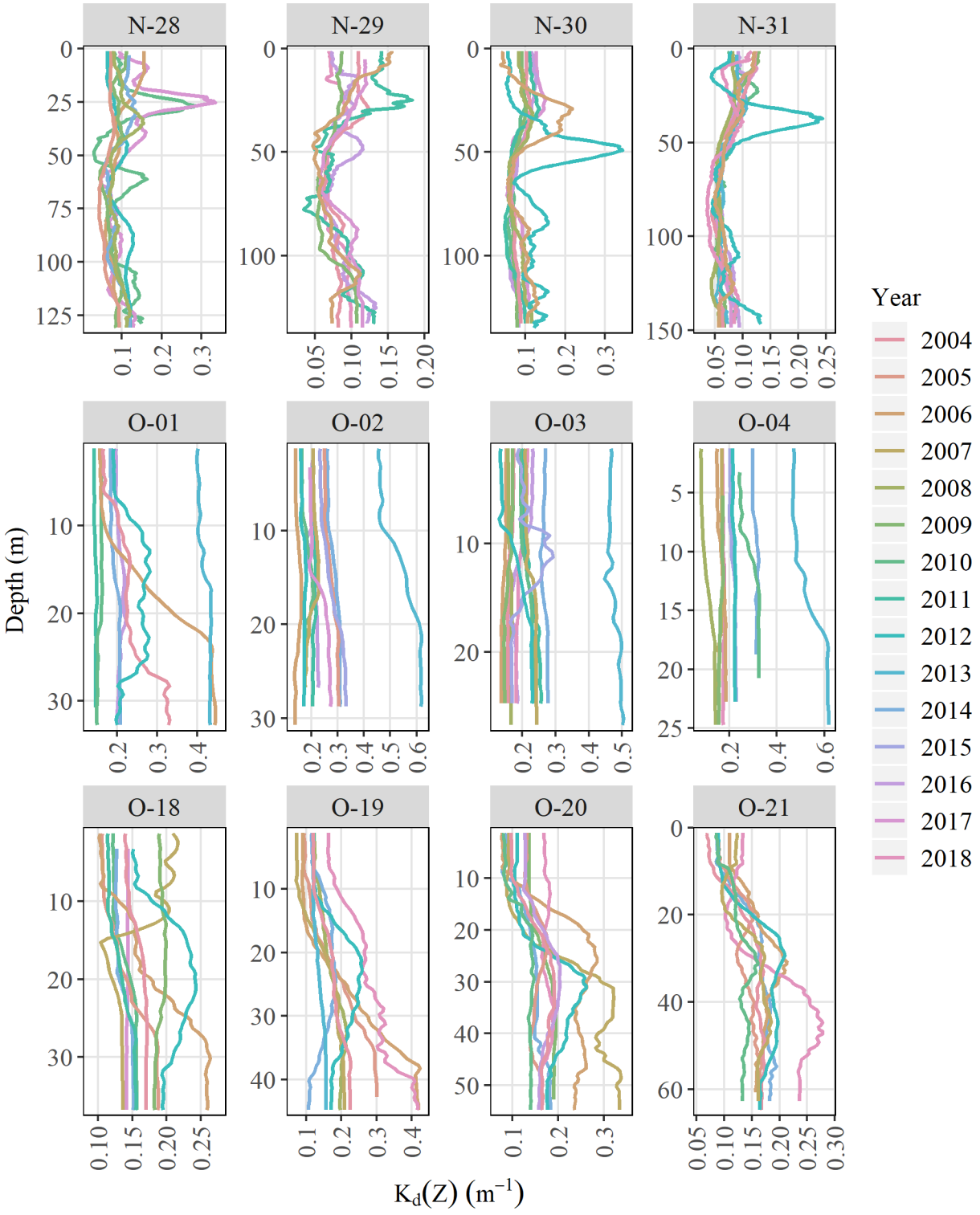

Appendix Figure B-1. -- Continued.

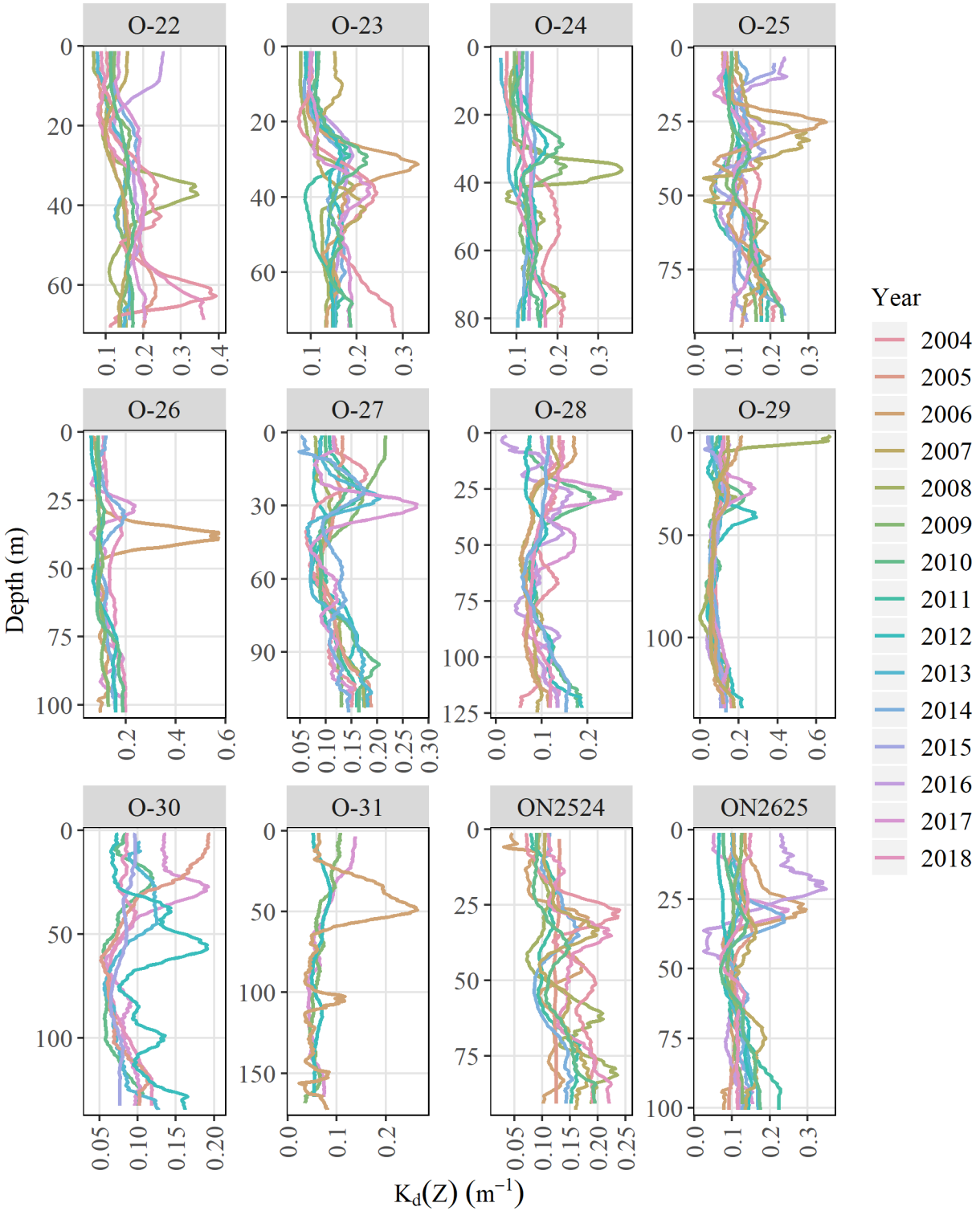

Appendix Figure B-1. -- Continued.

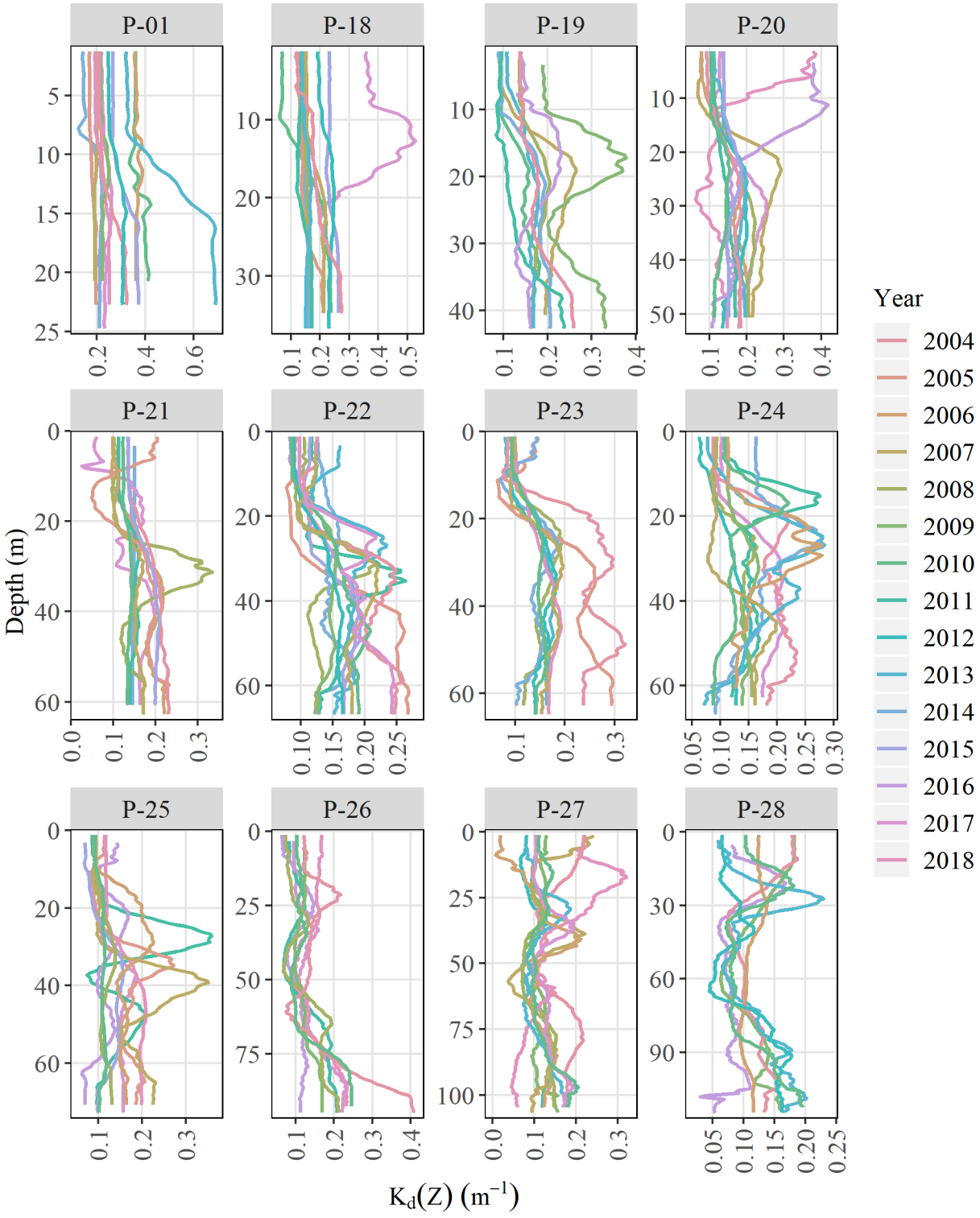

Appendix Figure B-1. -- Continued.

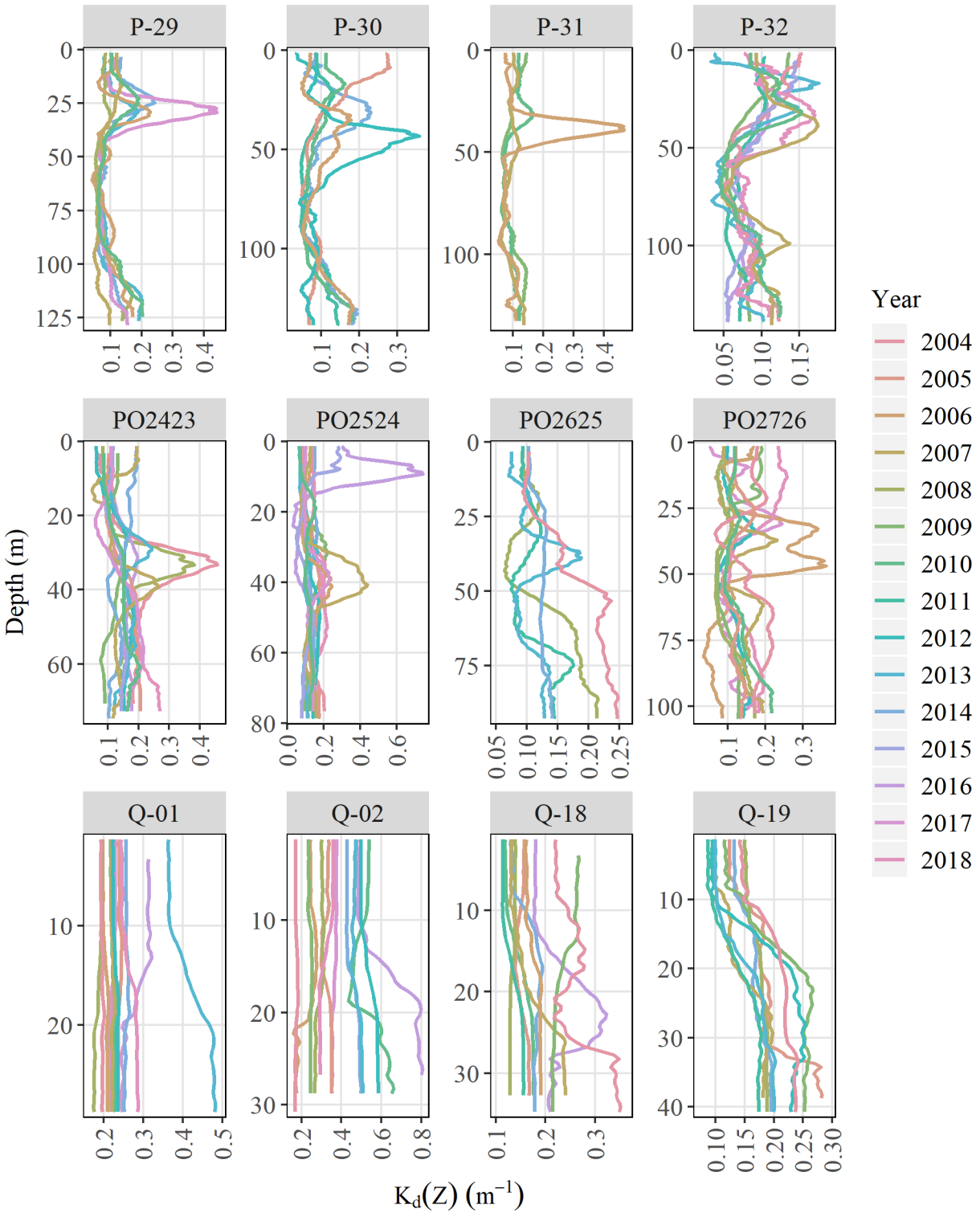

Appendix Figure B-1. -- Continued.

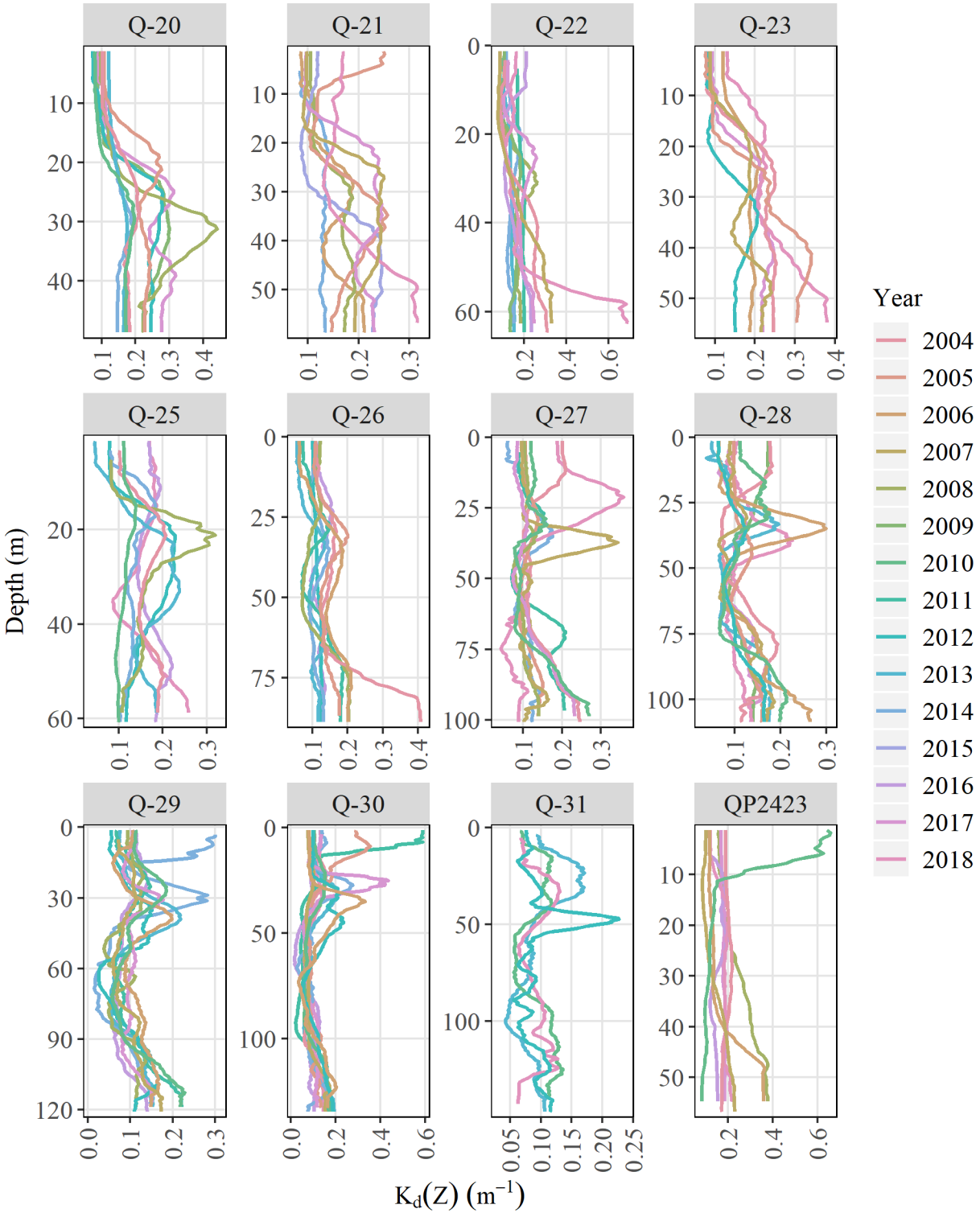

Appendix Figure B-1. -- Continued.

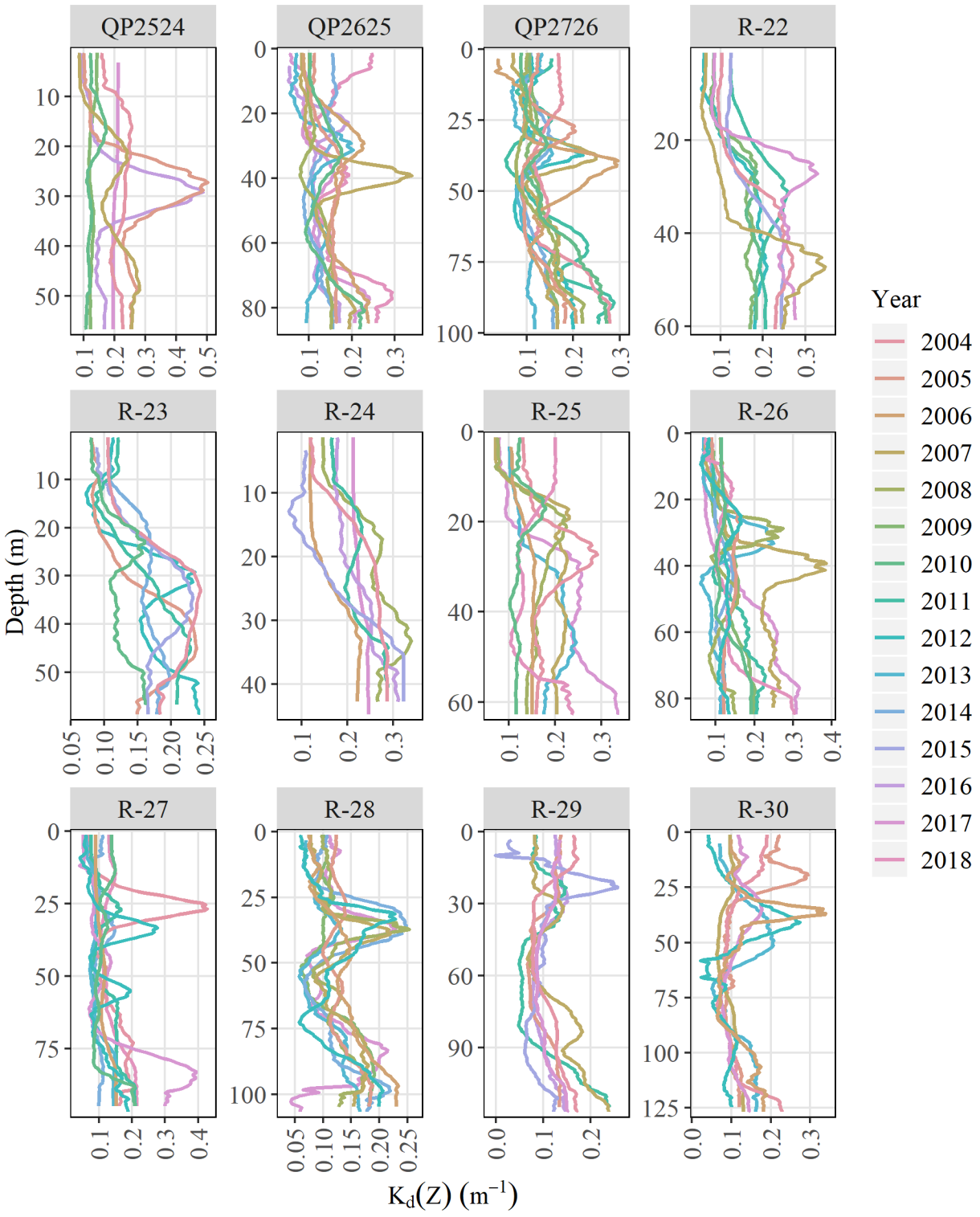

Appendix Figure B-1. -- Continued.

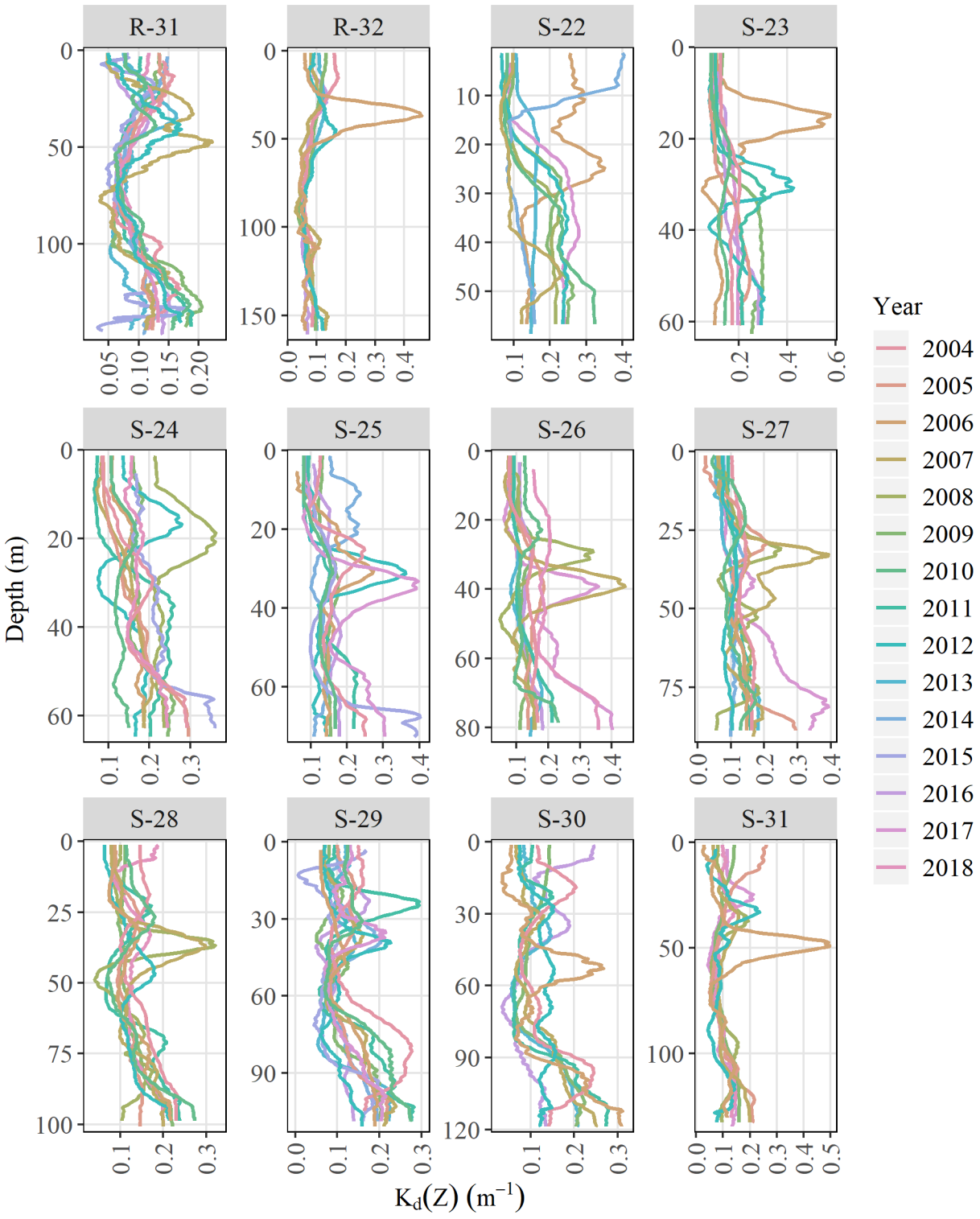

Appendix Figure B-1. -- Continued.

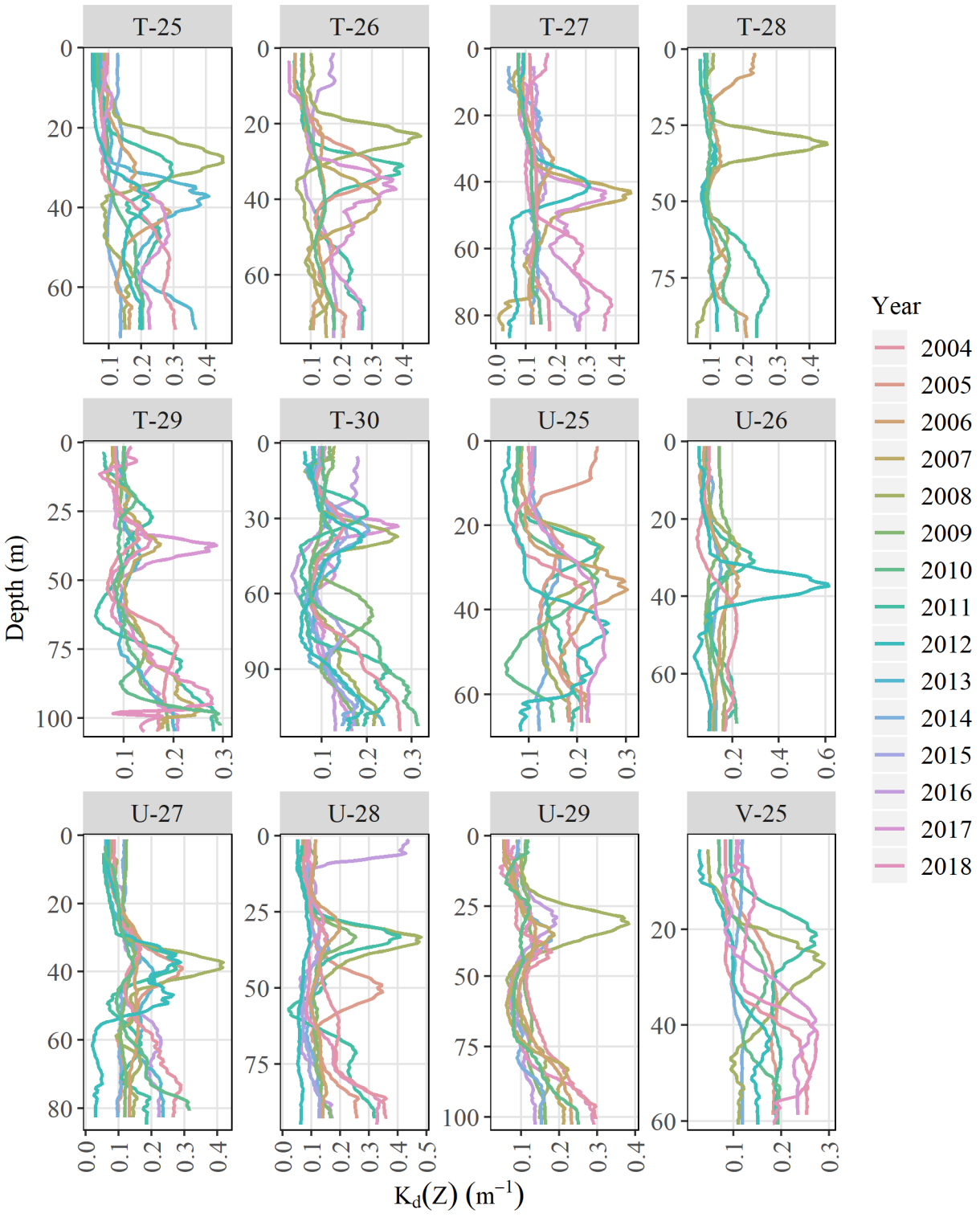

Appendix Figure B-1. -- Continued.

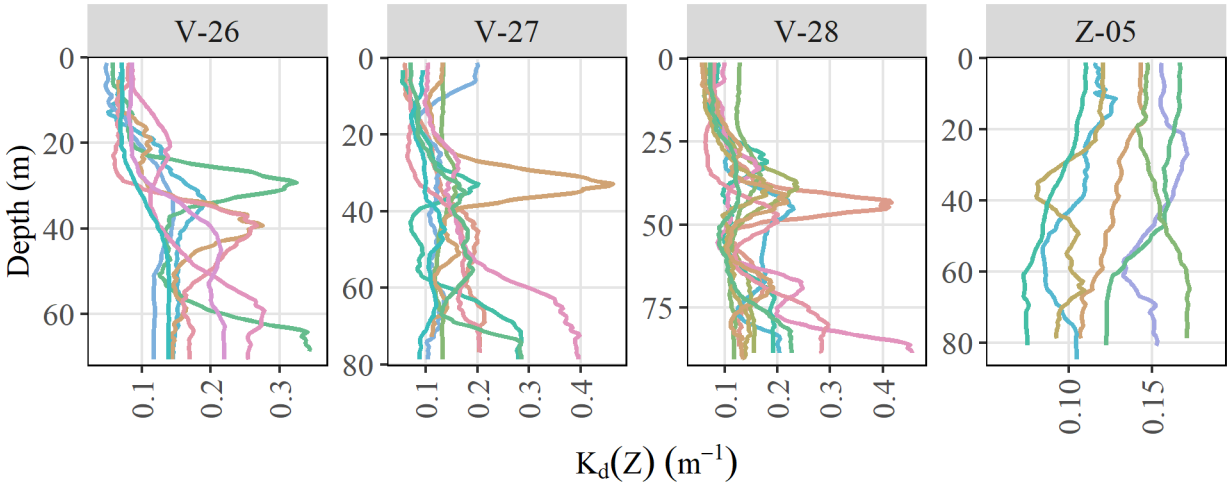

Appendix Figure B-1. -- Continued.

APPENDIX C: DATA PRODUCT

The experimental apparent optical properties data product for the eastern Bering Sea continental shelf[1] contains haul information, cast direction, optical depth, vertical attenuation coefficient of downwelling irradiance, and a flag indicating whether $E_d(1)$ was observed or estimated for a cast. Optical depth (Appendix Table C-1) and vertical attenuation coefficient (Appendix Table C-2) data are contained in separate data tables.

Appendix Table C-1. -- Field names and descriptions for optical depth.

Field Name	Description
latitude	Latitude (decimal degrees)
longitude	Longitude (decimal degrees)
time	Sampling time, AKST (UTC-8)
vessel	AFSC/RACE vessel code
cruise	AFSC/RACE cruise code
haul	AFSC/RACE haul code
stationid	AFSC/RACE station code
updown	Cast direction (upcast or downcast)
est_ref	Light level for the reference depth is estimated (True/False)
optical_depth	Optical depth
depth	Center of the depth bin (2 m bins)

Appendix Table C-2. -- Field names and variable descriptions for vertical attenuation coefficient table.

Field Name	Description
latitude	Latitude (decimal degrees)
longitude	Longitude (decimal degrees)
time	Sampling time, AKST (UTC-8)
vessel	AFSC/RACE vessel code
cruise	AFSC/RACE cruise code
haul	AFSC/RACE haul code
stationid	AFSC/RACE station code
updown	Cast direction (upcast or downcast)
depth	Depth bin (m), at 0.25 m resolution
kdz	Vertical attenuation coefficient of downwelling irradiance (m^{-1})

[1] Alaska Fisheries Science Center. 2020. AFSC/RACE/GAP/Rohan: Eastern Bering Sea Apparent Optical Properties Derived from Bottom-Trawl Survey Light Data, https://inport.nmfs.noaa.gov/inport/item/58980

U.S. Secretary of Commerce
Wilbur L. Ross, Jr.

Acting Under Secretary of Commerce for Oceans and Atmosphere
Dr. Neil Jacobs

Assistant Administrator for Fisheries
Chris Oliver

June 2020

www.nmfs.noaa.gov

OFFICIAL BUSINESS

National Marine Fisheries Service
Alaska Fisheries Science Center
7600 Sand Point Way N.E.
Seattle, WA 98115-6349